Verfahrenstechnik

Gimmy Alex Fernández Ramírez

Molecular Simulation of Transport Properties of Polar Fluids

SHAKER VERLAG

Molecular Simulation of Transport Properties of Polar Fluids

von der Fakultät Maschinenbau der Universiät Stuttgart zur Erlangung der Würde eines Doktor-Ingenieurs (Dr.-Ing.) genehmigte Abhandlung

vorgelegt von

Gimmy Alex Fernández Ramírez

aus Los Angeles, Chile

Hauptberichter: Prof. Dr.-Ing. H. Hasse
Mitberichter: Prof. Dr. S. Lago

Tag der mündlichen Prüfung: 11.05.2007

Institut für Technische Thermodynamik
und Thermische Verfahrenstechnik der
Universität Stuttgart, 2007

Berichte aus der Verfahrenstechnik

Gimmy Alex Fernández Ramírez

Molecular Simulation of Transport Properties of Polar Fluids

D 93 (Diss. Universität Stuttgart)

Shaker Verlag
Aachen 2007

***Bibliographic information* published by the Deutsche Nationalbibliothek**
The Deutsche Nationalbibliothek lists this publication in the Deutsche Nationalbibliografie; detailed bibliographic data are available in the Internet at http://dnb.d-nb.de.

Zugl.: Stuttgart, Univ., Diss., 2007

Gedruckt mit Unterstützung des Deutschen Akademischen Austauschdienstes

Printed in Germany.

ISBN 978-3-8322-6462-8
ISSN 0945-1021

Shaker Verlag GmbH • P.O. BOX 101818 • D-52018 Aachen
Phone: 0049/2407/9596-0 • Telefax: 0049/2407/9596-9
Internet: www.shaker.de • e-mail: info@shaker.de

Acknowledgments

This work was completed during an important period of my life where many things came together, it would not have been possible without the support of many people.

First, I would like to thank the Deutscher Akademischer Austauschdienst DAAD for the financial support and the opportunity to live in Germany and meet its people.

My grateful acknowledgment goes to my advisor Prof. Dr. Ing. Hans Hasse for the trust since the very beginning and during this work, his continuous support, supervision and good working atmosphere during my years at ITT. My grateful acknowledgment also goes to Prof. Dr. Santiago Lago, who kindly accepted to take part in the revision of this thesis.

I am grateful to Dr. Ing. Jadran Vrabec for the friendly support and many interesting and occasionally passionate discussions which enriched this work. I would also like to thank former colleagues at ITT: Dr. Ing. Thomas Grützner, Dipl. Ing. Thorsten Schnabel, and Dipl. Ing. Bernhard Eckl who help me with the correction of the German summary.

At last but not the least, I want to thank my wife, Viviam, who was with me in this enterprise all these years, my children Javiera, Karin, und Ignacio for reminding me of the things that are really important in life.

Ludwigshafen July 5, 2007.

Summary

In the present thesis, a comprehensive study on transport properties of polar fluids by molecular dynamics simulation using the Green-Kubo method is carried out. This study includes self-diffusion coefficient, binary Maxwell-Stefan diffusion, shear and bulk viscosity, and thermal conductivity of pure fluids and binary mixtures.

The molecular models used in the present work belong to the two-center Lennard-Jones plus point quadrupole (2CLJQ) or two-center Lennard-Jones plus point dipole (2CLJD) classes.

In the first part of the present work, predictions of transport properties of real fluids are compared with experimental data. The predictions are based on molecular models from the literature [250, 278, 279] that were adjusted to experimental vapor-liquid equilibrium data only.

Self-diffusion coefficients for gaseous and liquid state points are determined in the simulations with a statistical uncertainty of about 3 %. Predictions of self-diffusion coefficients show good agreement with experimental data. For Ar, CH_4, Kr, Ne, and Xe, which were modeled with the non-polar one-center Lennard-Jones model, the deviations are typically 5 % for gaseous state points, and 10 % for liquid state points. For all other fluids and also for all others transport properties, only liquid state points were investigated here, as for the transport properties of gases good theories are available. For F_2, N_2, CO_2, CS_2, C_2H_6, C_2H_4, C_2H_2, and SF_6, which were modeled with 2CLJQ models, the mean deviations between experimental self-diffusion coefficients and simulation data vary between 2 % and 28 %.

In mixtures, both self-diffusion and binary Maxwell-Stefan diffusion coefficients were obtained by molecular simulation. However, for binary mixtures containing the regarded components no experimental data for comparison with the simulations were available in the literature, with the exception of the gas mixtures Ar+Kr, Ar+Xe, Kr+Xe. These three mixtures, modeled with the non-polar one-center Lennard-Jones model show deviations between experiment and simulation of about 10 %. In these simulations, also self-diffusion coefficients in mixtures were generated. These were used to test the equation of Darken [42] for predicting binary Maxwell-Stefan diffusion coefficients from self-diffusion coefficients in mixtures. The comparison shows a good agreement with experimental data.

The good agreement between predictions for self-diffusion coefficients of liquid N_2, CO_2, and C_2H_6 and experimental data stimulated work on predictions for the liquid mixtures N_2+CO_2, N_2+C_2H_6, and CO_2+C_2H_6. The simulation results for binary Maxwell-Stefan diffusion coefficients as well as the results for self-diffusion

coefficients of these mixtures were used to test the equations of Caldwell and Babb [18], Darken [42], and Vignes [273]. It is important to note here that the equation of Darken [42] uses the self-diffusion coefficients in the mixture to predict Maxwell-Stefan diffusion coefficients. On the other hand, the equations of Caldwell and Babb [18] and Vignes [273] only use infinite dilution diffusion coefficients as input data to predict Maxwell-Stefan diffusion coefficients in the mixture at finite mole fractions. In agreement with the findings for gas mixtures, Darken's equation [42] yields the best performance with an average deviation of 10 %. The equations of Caldwell and Babb [18] and Vignes [273] fail to predict the shape of the composition dependence of the Maxwell-Stefan diffusion coefficients.

Shear and bulk viscosity and thermal conductivity of pure and binary liquid mixtures were determined in the simulations with statistical uncertainties of about 10 %. Predictions for shear viscosity and thermal conductivity were investigated for the following pure liquids: Ar, CH_4, Kr, and Xe and for the two liquid mixtures Ar+Kr and Ar+CH_4. They show excellent agreement with experimental data as discussed in more detail below. In contrast, predictions for bulk viscosity of pure Ar, CH_4, Kr, and Xe show significant deviations from the experimental data. Likewise, predictions for bulk viscosity of the mixtures Ar+Kr and Ar+CH_4 show the same kind of deviations. Given the good agreement between experiment and simulation for the other transport properties, this discrepancy for the bulk viscosity could indicate inaccurate experimental data. Predictions for shear viscosity and thermal conductivity of pure F_2, N_2, O_2, CO_2, C_2H_6, C_2H_4, C_2F_6, C_3H_4, C_3H_6, and SF_6, modeled with 2CLJQ models, and the refrigerants R11 ($CFCl_3$), R12 (CF_2Cl_2), R22 (CHF_2Cl), R23 (CHF_3), R41 (CH_3F), R123 ($CHCl_2$-CF_3), R134a (CH_2F-CF_3), R142b (CH_3F-CF_2Cl), R143a (CH_3-CF_3), R152a (CH_2F-CF_3), modeled with 2CLJD models, show good agreement with correlations of experimental data. Average deviations between predictions and correlations for shear viscosity of quadrupolar fluids range from 4 % for C_3H_6 up to 27 % for C_2F_6. For thermal conductivity the deviations range from 7 % for N_2 and C_2H_6 up to 19 % for C_2F_6. The global average deviations of the predictions from the correlations of experimental data are 11 % and 12 % for thermal conductivity and shear viscosity, respectively. For shear viscosity of dipolar fluids, the deviations between predictions and correlations range from 7 % for R23 up to 25 % for R41. The predictions for thermal conductivity are slightly lower than experimental data with deviations that range from 3 % for R22 up to 22 % for R123. The global average deviations are 11 % and 14 % for thermal conductivity and shear viscosity, respectively. It must be pointed out, that in the calculation of shear viscosity at high density state points, the respective Green-Kubo integral shows slow convergence. A simple method to overcome this problem was suggested

in the present work. It is based on an extrapolation of the autocorrelation function with an analytical function to infinity. This correction contributes up to 20 % to the shear viscosity and improves the final results without additional computational effort.

In the second part of the present work, a systematic study of the influence of anisotropy and polarity on self-diffusion, shear viscosity, and thermal conductivity was carried out. This systematic study is accomplished through the variation of the model parameters in a dimensionless form, e.g. for the 2CLJQ model class, the Lennard-Jones parameters ε and σ, the elongation L, and the quadrupolar momentum Q can conveniently be grouped into two dimensionless parameters $L^* = L/\sigma$ and $Q^{*2} = Q^2/(4\pi\epsilon_0\varepsilon\sigma^5)$. In this way only these have to be varied. This was done in the limits were parameters of real fluids lie, i.e. quadrupole momenta in the range $0 \leq Q^{*2} \leq 4$, and elongations in the range $0 \leq L^* \leq 0.8$. Altogether 30 2CLJQ model fluids were studied here. The procedure for the 2CLJD model class was completely analogous, i.e. dipolar momenta in the range $0 \leq \mu^{*2} \leq 20$ for spherical fluids ($L^* = 0$), dipolar momenta in the range $0 \leq \mu^{*2} \leq 16$ for little elongated fluids ($L^* = 0.2$), and dipolar momenta in the range $0 \leq \mu^{*2} \leq 12$ for elongations in the range $0.4 \leq L^* \leq 1.0$ were studied, which makes altogether 38 2CLJD fluids.

In that study also temperature and density were treated in a dimensionless form, i.e. $T^* = Tk_B/\epsilon$ and $\rho^* = \rho\sigma^3$. The study was carried out along bubble lines and for homogeneous liquid states. In order to achieve a meaningful comparison between the transport properties, also other reduced forms of temperature $T_R = T^*/T_c^*$ and density $\rho_R = \rho^*/\rho_c^*$ were introduced, where T_c^*, ρ_c^* are the critical temperature and density of the individual fluid, respectively.

For 2CLJQ fluids, four points that range from $T_R = 0.6$ to 0.9 with intervals of $\Delta T_R = 0.1$ along the bubble line were considered. In addition to those four points, another twelve points in the homogeneous liquid region were simulated. These points were selected on isochors starting from each bubble point with temperature increments of $\Delta T_R = 0.1$. In this way, also isothermal data were generated. In total, 480 state points were simulated and for each point self-diffusion coefficient, shear viscosity, and thermal conductivity were calculated.

The results of this study for 2CLJQ model fluids show that self-diffusion coefficient, shear viscosity and thermal conductivity coefficients depend predominantly on density. The results for each transport property can be summarized as follows:

Self-diffusion coefficient: It decreases with increasing ρ^* at constant L^* and Q^{*2} along the bubble line. In homogeneous liquid states, it increases linearly with increasing T_R at constant ρ^*, L^*, and Q^{*2}. With respect to the molecular parameters, it decreases with increasing L^* at constant ρ^*, T_R, and Q^{*2}, and with increasing Q^{*2}

at constant ρ^*, T_R, and L^*.

Shear viscosity: It increases with increasing ρ^* at constant L^* and Q^{*2} along the bubble line. In homogeneous liquid states, it decreases with increasing T_R at constant ρ^*, L^*, and Q^{*2}. With respect to the molecular parameters, it increases with increasing L^* at constant ρ^*, T_R, and Q^{*2}, and with increasing Q^{*2} at constant ρ^*, T_R, and L^*.

Thermal conductivity: It behaves similar to shear viscosity. It increases with increasing ρ^* at constant L^* and Q^{*2} along the bubble line. The dependence on T_R in homogeneous liquid states at constant ρ^*, L^*, and Q^{*2} is very weak and *not significant with respect to the statistical uncertainty of the simulation data.* Regarding L^* and Q^{*2}, it increases with increasing L^* at constant ρ^*, T_R, and Q^{*2}. The effect of Q^{*2} at constant ρ^*, T_R, and L^* is more difficult to discern because of the statistical uncertainty of the simulations, but it seems to increase with increasing Q^{*2}.

For 2CLJD fluids an analogous study was carried out, in this case just three points that range from $T_R = 0.6$ to 0.9 with intervals of $\Delta T_R = 0.15$ along the bubble line were considered. In addition to those three points, another nine points in the homogeneous liquid region were simulated. These points were selected starting from isochors starting from each bubble point with temperature increments of $\Delta T_R = 0.15$. In this way, also isothermal data was generated. In total, 456 state points were simulated and for each point self-diffusion coefficient, shear viscosity, and thermal conductivity were calculated.

The results of this analogous study for 2CLJD fluids show that self-diffusion coefficient, shear viscosity, and thermal conductivity depend predominantly on density in the same way as for 2CLJQ fluids. However, in contrast to the quadrupolar interaction, the dipolar interaction shows a much more significant effect on the transport properties. The results for each transport property can be summarized as follows:

Self-diffusion coefficient: It decreases with increasing ρ^* at constant L^* and μ^* along the bubble line. In homogeneous liquid states, it increases linearly with increasing T_R at constant ρ^*, L^*, and μ^{*2}. As expected, self-diffusion decreases with increasing L^* at constant ρ^*, T_R, and μ^{*2}. Remarkably, self-diffusion seems to increase with increasing μ^{*2} at constant ρ^*, T_R, and L^* at least for dipolar momenta $\mu^{*2} > 6$. The elongation affects the influence of the dipolar momentum on self-diffusion, the more elongated the fluid, the smaller is the effect of μ^{*2} on self-diffusion. In particular, for very elongated fluids ($L^* = 0.8$), no influence of the dipolar momentum was observed.

Shear viscosity: It increases with increasing ρ^* at constant L^* and μ^{*2} along the bubble line. In homogeneous liquid states, it decreases with increasing T_R at

constant ρ^*, L^*, and μ^{*2}. In the same way as for quadrupolar fluids, shear viscosity increases with increasing L^* at constant ρ^*, T_R, and μ^{*2}, and with increasing μ^{*2} at constant ρ^*, T_R, and L^*. Elongation affects the influence of the dipolar momentum in the same way as for self-diffusion. However, in contrast to self-diffusion, even for very elongated fluids the effect of dipolar momentum is significant.

Thermal conductivity: It increases with increasing ρ^* at constant L^* and μ^{*2} along the bubble line. Like for quadrupolar fluids, the dependence on T_R in homogeneous liquid states at constant ρ^*, L^*, and μ^{*2} is not significant considering the statistical uncertainty of the simulation data. Furthermore, it increases with increasing L^* at constant ρ^*, T_R, and Q^{*2} as well as with increasing μ^{*2} at constant ρ^*, T_R, and L^*.

The present data bring new detailed insight into the behavior of transport properties of polar fluids and can also be used to improve analytical theories to predict transport properties as well as for the development of physically based equations of state.

Zusammenfassung

Die vorliegende Arbeit beschäftigt sich mit der Vorhersage von Transporteigenschaften realer Fluide mit molekularen Methoden und mit der Untersuchung des Einflusses von thermodynamischen Variablen (Temperatur und Dichte) sowie molekularen Parametern auf die Transporteigenschaften. Diese Untersuchung wurde mit Hilfe von molekulardynamischen Gleichgewichtssimulationen und dem Green-Kubo Formalismus durchgeführt. Bei den untersuchten Transporteigenschaften handelt es sich um den Selbstdiffusionskoeffizient, den binären Maxwell-Stefan Diffusionskoeffizient, die Scher- und Volumenviskosität, sowie die Wärmeleitfähigkeit reiner Fluide und binärer Mischungen.

Im ersten Teil der vorliegenden Arbeit werden Vorhersagen für reale Fluide mit experimentellen Daten verglichen. Die Vorhersagen werden auf der Basis von molekularen Modellen aus der Literatur durchgeführt, die ausschließlich an experimentelle Phasengleichgewichte angepasst wurden. Bei der Entwicklung dieser molekularen Modelle sind keinerlei Informationen über Transporteigenschaften eingeflossen. Die verwendeten Modelle gehören zu den Ein- oder Zwei-Zentren-Lennard-Jones plus Quadrupol (2CLJQ) oder den Zwei-Zentren-Lennard-Jones plus Dipol (2CLJD) Potentialen.

Selbstdiffusionskoeffizienten konnten durch die Simulation mit einer statistischen Unsicherheit von etwa 3 % ermittelt werden. Vorhersagen auf der Basis von molekularen Modellen die nur aus nicht polaren Ein-Zentren-Lennard-Jones Potentialen bestehen, wurden für Ar, CH_4, Kr, Ne und Xe jeweils in Dampf- und Flüssigphase gemacht. Diese Ergebnisse zeigen eine gute Übereinstimmung mit experimentellen Daten, wobei die durchschnittliche Abweichung etwa 5 % für gasförmigen Zustände und 10 % für flüssige Zustände beträgt. Für Selbstdiffusionskoeffizienten von F_2, N_2, CO_2, CS_2, C_2H_6, C_2H_4, C_2H_2 und SF_6, die mit 2CLJQ Potentialen modelliert wurden, liegt die Abweichung zwischen experimentellen Daten bzw. Korrelationen des Selbstdiffusionskoeffizienten und der molekularen Simulation im Bereich von 2 bis 28 %.

Binäre Transport- und Selbstdiffusionskoeffizienten lassen sich mit einer statistischen Unsicherheit von 10 % bzw. 3 % bestimmen. Vorhersagen für gasförmigen Mischungen auf der Basis des nicht polaren Ein-Zentren-Lennard-Jones Modells wurden für die binären Mischungen Ar+Kr, Ar+Xe und Kr+Xe durchgeführt. Der Vergleich dieser Ergebnisse mit experimentellen Daten erfordert die Umrechnung von Maxwell-Stefan Diffusionskoeffizienten in binäre Diffusionskoeffizienten nach Fick. Binäre Maxwell-Stefan Diffusionskoeffizienten und Ficksche Diffusionskoeffizienten

stehen durch den thermodynamischen Faktor Λ in Zusammenhang. Für die hier untersuchteten Zustände kann dieser Faktor, ohne die Genauigkeit in der Rechnung wesentlich zu beeinträchtigen, zu Eins gesetzt werden. Die Abweichung zwischen den Simulationsergebnissen und den experimentellen Daten beträgt ca. 10 %. Die Simulationsdaten für binäre Maxwell-Stefan und Selbstdiffusionskoeffizienten wurden weiterhin verwendet, um das Modell von Darken [42] zu testen, das die Vorhersage von binären Maxwell-Stefan Diffusionskoeffizienten aus Selbstdiffusionskoeffizienten in Mischungen ermöglicht. Dieser Test zeigt eine gute Übereinstimmung zwischen den experimentellen Daten und dem Modell von Darken [42].

Die gute Übereinstimmung zwischen experimentellen Daten und Vorhersagen für flüssige Selbstdiffusionskoeffizienten der reinen Fluide N_2, CO_2 und C_2H_6 auf der Basis des 2CLJQ Modells, motivierte die Untersuchung der Vorhersage binären flüssigen Mischungen N_2+CO_2, N_2+C_2H_6 und CO_2+C_2H_6. Die Vorhersagen für diese drei Mischungen konnten auf Grund fehlender Diffusionsdaten nicht mit Experimenten verglichen werden. Diese Simulationen erhaltenen Daten wurden daher verwendet, um die drei Gleichungen von Darken [42], Caldwell und Babb [18] und Vignes [273] zur Vorhersage von binären Maxwell-Stefan Diffusionskoeffizienten zu bewerten. Hier ist anzumerken, dass die Gleichungen von Caldwell und Babb [18] sowie von Vignes [273] nur Diffusionskoeffizienten in unendlicher Verdünnung benötigen, während die Gleichung von Darken [42] Selbstdiffusionskoeffizienten für die Zusammensetzungen der Mischung erfordert. Die beste Übereinstimmung mit einer durchschnittlichen Abweichung von ca. 10 % wurde mit der Gleichung von Darken [42] erreicht. Außerdem konnten die Gleichungen von Caldwell und Babb [18] sowie Vignes [273] die Konzentrationsabhängigkeit des Diffusionskoeffizienten nicht richtig vorhersagen.

Scher- und Volumenviskosität sowie Wärmeleitfähigkeit für reine Fluide und Mischungen auf der Basis von nicht polaren Einzentren Lennard-Jones Modellen wurden in den Simulationen mit einer statistischen Unsicherheit von etwa 10 % ermittelt. Vorhersagen für Scherviskosität und Wärmeleitfähigkeit der reinen flüssigen Komponenten Ar, CH_4, Kr und Xe und den binären Mischungen Ar+Kr und Ar+CH_4 zeigen eine gute Übereinstimmung mit experimentellen Daten wie unter näher diskutiert. Andererseits zeigen die Vorhersagen für die Volumenviskosität sowohl für die reinen Fluide Ar, CH_4, Kr und Xe als auch für die binären Mischungen Ar+Kr und Ar+CH_4 große Abweichungen zu den experimentellen Daten. In allen Fällen sind die Vorhersagen systematisch zu niedrig. Die Abweichungen zwischen Simulation und Experiment weisen auf Schwierigkeiten bei der Messung der Volumenviskosität hin. Vorhersagen für Scherviskosität und Wärmeleitfähigkeit für die reinen Komponenten F_2, N_2, O_2, CO_2, C_2H_6, C_2H_4, C_2F_6, C_3H_4, C_3H_6 und

SF_6 auf der Basis des 2CLJQ Potentials und für die Kältemittel R11 ($CFCl_3$), R12 (CF_2Cl_2), R22 (CHF_2Cl), R23 (CHF_3), R41 (CH_3F), R123 ($CHCl_2$-CF_3), R134a (CH_2F-CF_3), R142b (CH_3F-CF_2Cl), R143a (CH_3-CF_3) und R152a (CH_2F-CF_3) auf der Basis des 2CLJD Potentials, zeigen eine gute Übereinstimmung mit Korrelationen experimenteller Daten. Die durchschnittlichen Abweichungen zwischen den Vorhersagen und den Korrelationen betragen zwischen 4 % für C_3H_6 und 27 % für C_2F_6. Für die Wärmeleitfähigkeit liegen diese zwischen 7 % für N_2 und C_2H_6 und 19 % für C_2F_6. Globale durchschnittliche Abweichungen über alle hier untersuchten Fluide betragen 11 % und 12 % für Wärmeleitfähigkeit bzw. Scherviskosität. Für die Scherviskosität dipolarer Fluide liegen die Abweichungen zwischen den Korrelationen experimenteller Daten und der Simulation zwischen 7 % für R23 und bis zu 25 % für R41. Andererseits zeigen hier die Vorhersagen für die Wärmeleitfähigkeit eine bessere Übereinstimmung mit den Korrelationen experimenteller Daten. Die Abweichungen für die Wärmeleitfähigkeit variieren zwischen 3 % für R12 bzw. bis zu 22 % für R123. Die globale Abweichung beträgt 11 % für die Wärmeleitfähigkeit und 14 % für die Scherviskosität.

Bei flüssigen Zuständen mit sehr hoher Dichte nahe dem Tripelpunkt kommt es bei der Verwendung der Green-Kubo Gleichung für die Scherviskosität zu Konvergenzproblemen. In dieser Arbeit wurde eine einfache Methode entwickelt, um dieses Problem zu lösen. Diese Methode beruht auf einer Extrapolation der Korrelationsfunktion ins Unendliche durch eine einfache analytische Funktion. Die Korrektur trägt bis zu 20 % zur ermittelten Scherviskosität bei und verbessert die Ergebnisse ohne zusätzliche molekulardynamische Berechnungen.

Im zweiten Teil dieser Arbeit wurde eine systematische Untersuchung des Einflusses der Polarität und der Anisotropie auf den Selbstdiffusionskoeffizient, die Scherviskosität und die Wärmeleitfähigkeit durchgeführt. In dieser Untersuchung wurden die dimensionslosen Modellparameter variiert. So werden zum Beispiel für das 2CLJQ Modell die Lennard-Jones Parameter ϵ und σ, die Elongation L und das quadrupolare Moment Q zu zwei dimensionslosen Variablen $L^* = L/\sigma$ und $Q^{*2} = Q^2/4\pi\epsilon_0\epsilon\sigma^5$ zusammengefasst. Die Variation wurde in dem für reale Fluide relevanten Bereich durchgeführt, d.h. für Quadrupole im Bereich $0 < Q^{*2} < 4$ und für Elongationen im Bereich $0 < L^* < 0.8$. Insgesamt wurden so 30 2CLJQ Fluide untersucht. Eine analoge Studie wurde auch für 2CLJD Fluide durchgeführt, wobei das dipolare Moment im Bereich $0 < \mu^{*2} < 20$ für kugelförmige Fluide ($L^* = 0$), $0 < \mu^{*2} < 16$ bei wenig elongierten Fluiden ($L^* = 0.2$) und $0 < \mu^{*2} < 12$ für größere Elongationen bis $L^* = 1$. Insgesamt wurden 38 2CLJD Fluide untersucht.

Die Untersuchung wurde auf Zustände auf der Siedelinie sowie auf homogene flüssige Zustände fokussiert. Um die Transporteigenschaften miteinander sinnvoll

vergleichen zu können, wurde die reduzierte Temperatur $T_R = T^*/T_c^*$ eingesetzt, wobei T_c^* die kritische Temperatur des jeweiliges Fluids ist.

Für 2CLJQ Fluide wurden vier Punkte bei verschiedenen Temperaturen ($T_R = 0.6, 0.7, 0.8$ und 0.9) auf der Siedelinie untersucht. Ausgehend von diesen vier Punkten wurden weitere zwölf Punkte im homogenen flussigen Zustandsgebiet simuliert, indem zu jedem Punkt auf der Siedelinie drei zusätzliche Punkte entlang Isochoren mit einem Abstand von $\Delta T_R = 0.1$ simuliert wurden. Auf diese Weise wurden auch isotherme Daten generiert, wobei insgesamt 480 Punkte simuliert wurden. Für jeden Punkt wurde der Selbstdiffusionskoeffizient, die Scherviskosität und die Wärmeleitfähigkeit ermittelt.

Alle Transporteigenschaften von 2CLJQ Fluiden hängen vor allem von der Dichte ab. Die Ergebnisse können in folgender Weise zusammengefasst werden:

Selbstdiffusionskoeffizient: Dieser nimmt mit ρ^* bei konstanten L^* und Q^{*2} entlang der Siedelinie ab. Im homogenen flüssigen Zustandsgebiet nimmt er linear mit zunehmendem T_R bei konstanten ρ^*, L^* und Q^{*2} zu. In Bezug auf die molekularen Parameter nimmt er mit zunehmendem L^* bei konstanten ρ^* und T_R ab. Ebenso nimmt er mit zunehmendem Q^{*2} bei konstanten ρ^*, T_R und L^* ab.

Scherviskosität: Diese nimmt mit ρ^* bei konstanten L^* und Q^{*2} entlang der Siedelinie zu. Im homogenen flüssigen Zustandsgebiet nimmt sie mit zunehmendem T_R bei konstanten ρ^*, L^* und Q^{*2} ab. In Bezug auf die molekularen Parameter nimmt sie mit zunehmendem L^* bei konstanten ρ^*, T_R und Q^{*2} zu, genauso mit zunehmendem Q^{*2} bei konstanten ρ^*, T_R und L^*.

Wärmeleitfähigkeit: Diese verhält sich ähnlich wie die Scherviskosität. Sie nimmt mit ρ^* bei konstanten L^* und Q^{*2} entlang der Siedelinie zu. Die Abhängigkeit von T_R im homogenen Zustandsgebiet ist sehr schwach und auf Grund der statistischen Unsicherheit der Simulationen nicht quantifizierbar. In Bezug auf die molekularen Parameter nimmt sie mit zunehmendem L^* bei konstanten ρ^*, T_R und Q^{*2} zu. Die Abhängigkeit von Q^{*2} ist wegen der Simulationsunsicherheit schwer zu erkennen. Sie scheint mit zunehmendem Q^{*2} bei konstanten ρ^*, T_R und L^* zunehmen.

Für 2CLJD Fluide wurden Simulationen in gleicher Weise wie für das 2CLJQ Fluide durchgeführt. In diesem Fall wurden drei Punkte bei reduzierten Temperaturen $T_R = 0.6, 0.75$ und 0.9 auf der Siedelinie simuliert. Zusätzlich wurden weitere neun Punkte im homogenen Zustandsgebiet simuliert, die aus den drei Punkten entlang von Isochoren mit einem Abstand von jeweils $\Delta T_R = 0.15$ generiert wurden, so dass auch isotherme Daten vorliegen. Insgesamt wurden 456 Punkte simuliert und für jeden Punkt den Selbstdiffusionskoeffizienten, die Scherviskosität und die Wärmeleitfähigkeit ermittelt.

In Übereinstimmung mit den Ergebnissen für 2CLJQ Fluide zeigen die Ergeb-

nisse für die 2CLJD Fluide einen dominierenden Einfluß der Dichte. Die Ergebnisse können in folgender Weise zusammengefasst werden:

Selbstdiffusionskoeffizient: Dieser nimmt mit ρ^* bei konstanten L^* und μ^{*2} entlang der Siedelinie ab. Im homogenen flüssigen Zustandsgebiet nimmt er linear mit zunehmendem T_R bei konstanten ρ^*, L^* und μ^{*2} zu. Wie erwartet, nimmt er mit zunehmendem L^* bei konstanten ρ^*, T_R und μ^{*2} ab. Bemerkenswerterweise nimmt er mit zunehmendem μ^* bei konstanten ρ^*, T_R und L^* zu, zumindest für dipolare Moment $\mu^{*2} > 6$. Die Elongation beeinflusst die Wirkung des dipolaren Moments auf den Selbstdiffusionkoeffizienten: je elongierter das Fluid ist, desto schwächer wird der Einfluss des dipolaren Moments.

Scherviskosität: Diese nimmt mit ρ^* bei konstanten L^* und μ^{*2} entlang der Siedelinie zu. Im homogenen flüssigen Zustandsgebiet nimmt sie mit zunehmendem T_R bei konstanten ρ^*, L^* und μ^{*2} ab. Genau wie für quadrupolare Fluide nimmt η^* mit zunehmendem L^* bei konstanten ρ^*, T_R und μ^{*2} zu. Bei konstanten ρ^*, T_R und L^* nimmt die Scherviskosität mit zunehmendem μ^{*2} zu, wobei auch hier genau wie bei D^* die Elongation die Wirkung des dipolaren Moments auf η^* beeinflusst.

Wärmeleitfähigkeit: Diese nimmt mit ρ^* bei konstanten L^* und μ^{*2} entlang der Siedelinie zu. In Übereinstimmung mit den Ergebnissen für 2CLJQ Fluide ist die Abhängigkeit von der T_R im homogenen Zustänsgebiet sehr schwach und wegen der statistischen Unsicherheit der Simulationsergebnisse nicht erkennbar. In Bezug auf die molekularen Parameter nimmt sie mit zunehmendem L^* bei konstanten ρ^*, T_R und μ^{*2} zu. Genau wie fü quadrupolare Fluide, ist die Abhängigkeit von μ^{*2} wegen der statistischen Unsicherheit schwer zu erkennen. Sie scheint bei konstanten ρ^*, T_R und L^* mit zunehmendem μ^{*2} zunehmen.

Die vorliegenden Ergebnisse geben einen Einblick in das Verhalten der Transporteigenschaften polarer Fluide und können zur Verbesserung analytischer Theorien zur Vorhersage von Transporteigenschaften angewendet werden sowie für die Entwicklung von physikalischen basierten Zustandsgleichungen.

Nomenclature

Latin

c_k	$\cos \theta_k$
s_k	$\sin \theta_k$
D_i	self-diffusion coefficient of species i
D_{12}	binary Fick diffusion coefficient
$Đ_{12}$	binary Maxwell-Stefan diffusion coefficient
$Đ_{12}^0$	Darken's estimate of the binary Maxwell-Stefan diffusion coefficient
D_{12}^∞	binary diffusion coefficient at infinite dilution
D^*	reduced self-diffusion coefficient
E	energy
h^k	partial molar enthalpy of species k
J_p^{xy}	xy stress tensor element
J_q^x	component x of the heat flow vector element
k_B	Boltzmann's constant
L	elongation
L^*	reduced elongation
M	molar mass
m_i	molecular mass of species i
m_i^k	molecular mass of particle i of species k
N	number of particles
N_i	number of molecules of species i
p	pressure
Q	quadrupolar momentum
Q^{*2}	squared reduced quadrupolar momentum
Q_s	inertial parameter of the Nosé-Hoover thermostat
r	intermolecular distance
r_c	cut-off radius
r_{ab}	distance between LJ site a and LJ site b
r_{ij}^x	component x of the distance vector between LJ site i and LJ site j
r_{ij}^{kl}	distance between LJ site a and LJ site b of species k or l
t	time
T	temperature
T_c^*	reduced critical temperature
T^*	reduced temperature
u	pair potential
u_{ij}^{2CLJ}	pair potential between two two-center Lennard-Jones molecules i and j

u_Q	pair potential between two ideal point quadrupoles
u_μ	pair potential between two ideal point dipoles
v	velocity
v_i^k	velocity of particle i of species k
$\mathbf{v}_i^k$	vector velocity of particle i of species k
V	volume
x	cartesian coordinate
x_i	mole fraction of species i
y	cartesian coordinate
z	cartesian coordinate
X	*fictitious field*

Greek

α	component
β	component
Δt	integration time step
ϵ	Lennard-Jones energy parameter
ϵ_{11}	Lennard-Jones energy parameter between species 1 only
ϵ_{22}	Lennard-Jones energy parameter between species 2 only
ϵ_{12}	Lennard-Jones energy parameter between species 1 and 2
ϵ_0	permittivity of the vacuum
η_s	shear viscosity
η^*	reduced shear viscosity
η_v	bulk viscosity
θ_i	angle between the axis of molecule i and the center-center connection line in the dipole-dipole interaction
Θ_{η_s}	normalized autocorrelation function for shear viscosity
Θ_{η_b}	normalized autocorrelation function for bulk viscosity
Θ_λ	normalized autocorrelation function for thermal conductivity
λ	thermal conductivity
λ^*	reduced thermal conductivity
Λ	thermodynamic factor
μ_i	*chemical potential of species* i
μ	dipolar momentum
μ^{*2}	squared reduced dipolar momentum
ξ	adjustable binary interaction parameter
ρ	density

ρ^*	*reduced number density*
ρ_c	critical density
σ	Lennard-Jones size parameter
σ_{11}	Lennard-Jones size parameter between species 1 only
σ_{22}	Lennard-Jones size parameter between species 2 only
σ_{12}	Lennard-Jones size parameter between species 1 and 2
$\phi(t)$	general notation of autocorrelation function
ϕ_{ij}	azimutal angle between the axis of molecules i and j
γ	general notation of transport property

Vectorial and Tensorial Quantities

$\mathbf{\Gamma}_{ij}$	torque vector on particle i due to interaction with particle j
$\mathbf{I}$	unitary tensor of second order
$\mathbf{J}$	thermodynamic flux vector
$\mathbf{J}_p$	stress tensor
$\mathbf{J}_q$	heat flow vector
$\mathbf{r}_{ij}$	distance vector
$\mathbf{v}_i$	velocity vector of particle i
$\mathbf{v}_i^j$	velocity vector of particle i of species j
$\mathbf{v}^{cm}$	velocity vector of the center of mass
$\mathbf{w}_i$	angular velocity vector of particle i

Contents

Chapter 1

Introduction

1.1 General Remarks

Transport phenomena are a manifestation of the non-equilibrium nature of the world around us. Transport occurs because of the natural tendency of all systems to reach equilibrium. In this process all gradients in a system tend to disappear, i.e. heat flows from high to low temperature regions, mass of a component i diffuses from high to low concentration regions, or momentum flows from high to low velocity regions.

Transport properties play a fundamental role in many fields of science and engineering. In process engineering, they have to be accounted for the mathematical modeling of the unit operations. They often determine the equipment design, its performance and safety, and the economy. Therefore, the knowledge of transport properties is fundamental for the design and optimization of processes. Some examples are, for instance, the design of chemical reactors, in particular those where chemical reactions take place in more than one phase, or separation equipment. Errors in the values of the transport properties used in the design can propagate throughout the design of the entire plant and negatively affect the capital and operation cost.

The main source of information on transport properties are experiments. However, it is clear that the industry's needs can not be met by experiments alone, so that methods to calculate transport properties are necessary. The most suitable substitute for the direct measurement would be a rigorous statistical mechanic theory that would allow predicting transport properties from ab-initio calculations. Unfortunately, up to now, there is no tractable way to come near this and predict transport properties in such a general form. Current theories are typically limited to a narrow range of densities or serve only as initial point for correlating experimental data. Many of the current methods for predicting transport properties are based on

the theory of corresponding states [255, 256], free volume theory [159, 198, 217], or Enskog theory [47, 48]. A compilation of methods is given by Poling et al. [213].

With the availability of fast computers, molecular simulation is offering an alternative way to supply transport properties. The reliability of the predictions from molecular simulation depends directly on the ability of the molecular model to reproduce the interactions among the real molecules. The application of molecular simulation is not restricted to simulation of bulk properties at or near ambient conditions, much more interesting is the estimation of thermodynamic properties under extreme conditions of pressure [15, 137, 189], temperature [15, 24, 34, 64, 82] or where direct measurements are technically difficult or impracticable, as for example under metastable conditions [126, 168], inside of pores [164, 215], due to toxicity [151, 216], or simply when experiments are too expensive.

1.2 Scope and contribution of this work

The topic of this thesis is the study and prediction of transport properties by molecular simulation. The principal goals of this work are firstly, to assess the adequacy of molecular models that were adjusted to experimental vapor-liquid equilibria only to predict transport properties of fluids; and secondly, to systematically investigate the effect of molecular parameters on the transport properties of liquids.

In this work, transport properties are calculated by equilibrium molecular dynamics and the Green-Kubo method [88, 89, 133, 134]. Predictions for real fluids are made on the basis of molecular models from the literature that were adjusted to experimental vapor-liquid equilibria only [250, 278, 279]. These models belong to the two-center Lennard-Jones plus point quadrupole (2CLJQ) or dipole (2CLJD) class. They consist of two Lennard-Jones centers separated by a distance L and one embedded ideal point quadrupole Q or point dipole μ in its geometrical center. In the limit of zero elongation and polarity, the models reduce to one Lennard-Jones center. With these models, predictions for self-diffusion, binary Maxwell-Stefan diffusion coefficients, shear and bulk viscosity and thermal conductivity were made. These were compared with experimental data and correlations thereof, giving important information about their predictive power for future practical applications.

The direct access to self-diffusion coefficients and Maxwell-Stefan diffusion coefficients was also used to investigate a number of empirical equations to predict binary Maxwell-Stefan coefficients. This novel approach has brought insight in the performance and applicability of such correlations.

An important part of this work is focused on a systematic study of the 2CLJQ and 2CLJD model fluids. They are treated in terms of reduced molecular and

thermodynamic properties allowing a general characterization of the influence of the different molecular features. Previously, no comprehensive information on the transport properties of the 2CLJQ or 2CLJD models was available. The present work fills this gap, by supplying a extensive set of data for self-diffusion, shear viscosity, and thermal conductivity coefficients for these models. The influence of the elongation L, quadrupolar Q, and dipolar momentum μ on these transport properties is investigated in detail, bringing new insight into the dependence of these transport properties on polarity and anisotropy. This comprehensive data set paves the way for future improvement of current theories, and for developing new theories as well as for the development of physically based equations of state.

This work is organized as follows: Chapter 2 describes the current methods for predicting transport properties from molecular dynamics simulation. These methods are classified and compared. In Chapters 3 and 4 results from the prediction of transport properties for real fluids that can be described with the one-center Lennard-Jones potential and the 2CLJQ potential are presented. Predictions for self-diffusion and Maxwell-Stefan diffusion coefficients are compared with experimental data. Furthermore, the performance of three empirical equations for modeling the Maxwell-Stefan diffusion coefficients are assessed. In Chapter 4, results for shear and bulk viscosity, and thermal conductivity of pure fluids and mixtures for real fluids modeled with one-center LJ, 2CLJQ and 2CLJD potentials are compared with experimental data and correlations.

Finally, Chapter 5 presents the results of the comprehensive study on self-diffusion, shear viscosity, and thermal conductivity coefficients of 2CLJQ and 2CLJD model fluids. This study is focused on states along the bubble line and on homogeneous liquid states. A detailed investigation of the effect of temperature, density, anisotropy, i.e. elongation, and polarity, i.e. quadrupolar or dipolar momentum was carried out.

Chapters 3 to 5 are organized independently so that they can be read alone.

Chapter 2

Theoretical background

2.1 Molecular models

Throughout the present work two-center Lennard-Jones (2CLJ) plus point quadrupole (2CLJQ) or dipole (2CLJD) molecular models are used. Parameters for these models are available in the literature that allow an accurate description of vapor-liquid equilibria (VLE) [250, 278, 279]. These were used here without any changes, so that all results from the present work for the transport properties of real fluids in Chapters 2 to 4 are predictions from vapor-liquid equilibria only. Furthermore, these models are used in Chapter 5 for a systematic study.

Both 2CLJQ and 2CLJD models are pairwise additive potential models consisting of two Lennard-Jones sites a distance L apart plus a point quadrupole or dipole located in the geometric center of the molecule. The quadrupole and dipole, respectively, are oriented along the molecular axis which connects the two LJ sites. The interaction energy for the 2CLJ potencial of two molecules i and j is given by

$$u_{ij}^{\mathrm{2CLJ}}(r_{ab}) = \sum_{a=1}^{2}\sum_{b=1}^{2} 4\epsilon_{ij}\left[\left(\frac{\sigma_{ij}}{r_{ab}}\right)^{12} - \left(\frac{\sigma_{ij}}{r_{ab}}\right)^{6}\right]. \tag{2.1}$$

Here, r_{ab} is the distance between LJ site a and LJ site b; a counts the two sites of molecule i, b counts those of molecule j. The LJ parameters σ_{ij} and ϵ_{ij} represent the size and energy parameters of the LJ potential, respectively. The quadrupolar contribution is given by [87]

$$\begin{aligned} u_{\mathrm{Q}}(r_{ij},\theta_i,\theta_j,\phi_{ij},Q) &= \frac{1}{4\pi\epsilon_0}\frac{3}{4}\frac{Q^2}{r_{ij}^5} \\ &\quad \left[1 - 5\left(c_i^2 + c_j^2\right) - 15c_i^2c_j^2 + 2\left(s_is_jc - 4c_ic_j\right)^2\right] \end{aligned} \tag{2.2}$$

and the dipolar contribution is given by [87]

$$u_D(r_{ij}, \theta_i, \theta_j, \phi_{ij}, \mu) = \frac{1}{4\pi\epsilon_0} \frac{\mu^2}{r_{ij}^3}(c - c_i c_j), \tag{2.3}$$

where $c_k = \cos\theta_k$, $s_k = \sin\theta_k$, $c = \cos\phi_{ij}$, and r_{ij} is the center-center distance of the two molecules i and j. θ_i is the angle between the axis of the molecule i and the center-center connection line, and ϕ_{ij} is the azimutal angle between the axis of molecules i and j. Finally, ϵ_0 is the permittivity of the vacuum.

Pure substance parameters σ, ϵ, L, and Q for quadrupolar fluids were taken from [278] and are summarized in Table 2.1.

Table 2.1: Potential model parameters for the quadrupolar pure fluids used in this work [278].

Fluid	CAS RN	σ Å	ϵ/k_B 1/K	L Å	Q 10^{20}C m^2	M g/mol
Ne	7440-01-9	2.8010	33.921	0	0	20.180
Ar	7440-37-1	3.3952	116.79	0	0	39.948
Kr	7439-90-9	3.6274	162.58	0	0	83.8
Xe	7440-63-3	3.9011	227.55	0	0	131.29
CH_4	74-82-8	3.7281	148.55	0	0	16.043
F_2	7782-41-4	2.8258	52.147	1.4129	2.9754	38.00
N_2	7727-37-9	3.3211	34.897	1.0464	4.8024	28.01
CO_2	124-38-9	2.9847	133.22	2.4176	12.6549	44.01
CS_2	75-15-0	3.6140	257.68	2.6809	13.0081	76.14
C_2H_6	74-84-0	3.4896	136.99	2.3762	2.7609	30.07
C_2H_4	74-85-1	3.7607	76.950	1.2695	14.4468	28.05
C_2H_2	74-86-2	3.5742	79.890	1.2998	16.9218	26.04
SF_6	2551-62-4	3.9615	118.98	2.6375	26.7074	146.06

The parameters in Table 2.1 were adjusted to experimental vapor pressure and saturated liquid density data of the pure substances. For symmetric diatomic molecules like fluorine (F_2) and nitrogen (N_2), symmetric triatomic molecules like carbon dioxide (CO_2) and carbon disulfide (CS_2), as well as C_2 derivates as ethane (C_2H_6) and ethylene (C_2H_4) the description of the interaction by the 2CLJQ potential represents a good approximation. Note that the SF_6 molecule is neither elongated nor quadrupolar, so that the parameters of the 2CLJQ model have only little physical meaning. In the limiting case $L = 0$ without polarity, the polar 2CLJQ models reduce to one-center Lennard-Jones models. In this work five pure fluids and three mixtures are modeled with this potential.

Pure substance parameters σ, ϵ, L, and μ for dipolar fluids were taken from [250] and are summarized in Table 2.2. They were adjusted in [250] exclusively to experimental pure substance vapor-liquid equilibrium data.

Table 2.2: Potential model parameters for the dipolar pure fluids used in this work [250].

Fluid	CAS RN	σ Å	ϵ/k_B 1/K	L Å	μ D	M g/mol
R11 ($CFCl_3$)	75-69-4	4.0213	224.15	3.3377	2.7009	137.37
R12 (CF_2Cl_2)	75-71-8	3.8286	185.66	3.2700	2.3219	120.91
R22 (CHF_2Cl)	75-45-6	3.4682	177.43	3.1203	2.2667	86.468
R23 (CHF_3)	75-46-7	3.2643	123.56	2.5670	2.1607	70.014
R41 (CH_3F)	593-53-3	3.0382	137.64	2.4530	1.8850	34.033
R123 ($CHCl_2$-CF_3)	306-83-2	4.0530	221.75	4.0530	3.7002	152.93
R134a (CH_2F-CF_3)	811-97-2	3.6138	175.12	3.6138	3.0214	102.03
R142b (CH_3F-CF_2Cl)	75-68-3	3.8404	193.68	3.4675	2.9610	100.5
R143a (CH_3-CF_3)	420-46-2	3.5960	165.04	3.5395	2.7470	84.041
R152a (CH_2F-CF_3)	75-37-6	3.5168	182.01	3.3125	2.7354	66.051

In the modeling of mixtures assuming pairwise additivity, the like interactions are fully described by the pure substance parameters. The same holds for the unlike quadrupolar or dipolar interaction, which are exactly determined by electrostatics, cf. Eq. (2.2). On the other hand, the parameters of the unlike Lennard-Jones interactions have to be estimated. They were obtained in the present work from the pure fluid parameters by the modified Lorentz-Berthelot combination rule

$$\sigma_{12} = \frac{(\sigma_{11} + \sigma_{22})}{2}, \tag{2.4}$$

and

$$\epsilon_{12} = \xi \cdot \sqrt{\epsilon_{11}\epsilon_{22}}, \tag{2.5}$$

where ξ is a binary interaction parameter that was adjusted to one experimental bubble point of the binary mixture. It has been shown in previous work of other authors for numerous systems [277, 279] that binary and ternary vapor-liquid equilibria can be described accurately in this way. The parameters used in this work were taken from [279], their values are given in Table 2.3.

Table 2.3: Binary interaction parameters [279] for three mixtures.

Mixture	ξ
N_2+CO_2	1.041
N_2+C_2H_6	0.974
CO_2+C_2H_6	0.954

2.2 Methods for calculating transport coefficients

In this section, an overview of the standard methods for calculating transport properties by molecular simulation is given. The available methods can be classified in nonequilibrium molecular dynamics (NEMD) and equilibrium molecular dynamics methods (EMD). The overview begins with the NEMD methods; these methods represent a vast field of current research and there are many good reviews which give account of its progress in the last twenty years [38, 58, 62, 225]. A detailed description of these methods is out of the scope of this work, nevertheless a brief description is given here. It is focused on the main characteristics of the NEMD methods, and differences between NEMD and EMD approaches, their advantages and drawbacks. It is intended as starting point for introducing the EMD methods, in particular the Green-Kubo method [88, 89, 133, 134] and furthermore for a comparison. The Green-Kubo method is used throughout this work to calculate transport properties from molecular simulation. In the present section the Green-Kubo equations for the self-diffusion and the binary Maxwell-Stefan diffusion coefficients as well as shear and bulk viscosity and thermal conductivity coefficients are given in full detail.

2.2.1 Nonequilibrium molecular dynamics methods

Nonequilibrium molecular dynamics methods can be subclassified in synthetic and boundary driven nonequilibrium methods. The synthetic nonequilibrium methods (S-NEMD) are characterized by the introduction of a fictitious field X into the equations of motion that drives a thermodynamic flux $\mathbf{J}$. For instance, a momentum flux in planar Couette flow or a heat current for thermal conductivity [62]. In addition, this method requires the use of special boundary conditions, like the Lees-Edwards sliding brick boundary conditions [138] for the calculation of shear viscosity, in order to ensure that the simulation sample remains homogeneous [5]. A second requirement is that the transport property of interest γ, can be obtained from the following constitutive equation

$$\gamma = \lim_{X \to 0} \lim_{t \to 0} \frac{\mathbf{J}}{X}. \tag{2.6}$$

There are many S-NEMD methods to simulate shear viscosity [25, 26, 58, 62, 85, 136, 241], thermal conductivity [57, 59, 60, 84], and binary transport diffusion coefficients [163], more details about these methods can be found in the original works, or in the reviews by Evans and Morriss [58], Cummings and Evans [38], and Sarman et al. [225].

The second subclass are the boundary driven molecular dynamics methods (BD-NEMD). These methods are characterized by a very intuitive conception that mimics a real system. Here, a gradient is imposed through the boundaries of the simulation sample, by construction of suitable reservoirs on opposite sides of the simulation zone. Once the steady state flux is achieved and through knowledge of the gradient between the reservoirs, the transport coefficients can be evaluated directly using the proper equations given by irreversible thermodynamics. This method has been successfully applied to study: diffusion in fluid systems [257, 258], membranes [79, 80, 160, 161, 162, 197, 214], nanotubes [72, 73, 290], polymers [75, 119], zeolites [8, 110, 200]; rheological properties of polymers [286], silicon surfaces [287, 288]; thermal conductivity in carbon nanotubes [14, 167, 193, 205] and fluids [201, 210, 236, 237]. A recent variant of this method is the so called reverse nonequilibrium molecular dynamics [194, 289]. In that method a heat flux, and not a gradient in temperature, is imposed on the system by suitable exchange of velocities of particles from different regions. It generates a gradient of temperature which is used to calculate the thermal conductivity. A detailed discussion on advantages and disadvantages of this method is given in [194].

2.2.2 Equilibrium molecular dynamics and Green-Kubo formalism

Transport coefficients are associated to irreversible processes, however, it is possible to describe irreversible processes in terms of reversible microscopic fluctuations, through the fluctuation dissipation theory [135]. In that theory, it is shown that transport coefficients can be calculated as integrals of time-correlation functions of appropriate fluxes, i.e. mass flux for diffusion, momentum flux for shear viscosity, and heat flux for thermal conductivity [89, 133]. An alternative way is to measure the accumulated displacement of the fluxes over time, called the Einstein relations, which basically are the integrated form of the Green-Kubo equations. There are different methods for relating transport coefficients to time-correlation functions; a good review can be found in [292].

Diffusion coefficients

Diffusion coefficients can be calculated by equilibrium molecular dynamics through the Green-Kubo formalism [89, 133]. In this formalism, diffusion coefficients are related to integrals of velocity-autocorrelation functions. The self-diffusion coefficient D_i of a component i either as a pure fluid or in a mixture is characterized by the velocity of a single target molecule [91, 115, 170, 266]. Its expression is given by

$$D_i = \frac{1}{3N_i} \int_0^\infty \mathrm{d}t \left\langle \sum_{k=1}^{N_i} \mathbf{v}_i^k(0) \cdot \mathbf{v}_i^k(t) \right\rangle, \tag{2.7}$$

where $\mathbf{v}_i^k(t)$ expresses the velocity vector of molecule k of species i and the notation $< ... >$ denotes the ensemble average. Eq. (2.7) yields the self-diffusion coefficient for component i averaging over N_i molecules. Likewise, the expression for the binary Maxwell-Stefan diffusion coefficient $Đ_{12}$ is given in terms of velocities of the molecular centers of mass [95, 266]

$$Đ_{12} = \frac{x_2}{3N_1} \left(\frac{x_1 M_1 + x_2 M_2}{x_2 M_2} \right)^2 \int_0^\infty \mathrm{d}t \left\langle \sum_{k=1}^{N_1} \mathbf{v}_i^k(0) \cdot \sum_{k=1}^{N_1} \mathbf{v}_i^k(t) \right\rangle, \tag{2.8}$$

where M_i denotes the molar mass of molecules of species i, N_1 the number of molecules of species 1 and x_1 and x_2 are the mole fractions.

To compare Maxwell-Stefan diffusion coefficients to available experimental data, it is often necessary to transform the Maxwell-Stefan diffusion coefficients to Fick diffusion coefficients. There is a direct relation between binary Maxwell-Stefan diffusion coefficients $Đ_{12}$ and binary Fick diffusion coefficients D_{12} [131], which is given by

$$D_{12} = Đ_{12} \Lambda, \tag{2.9}$$

with

$$\Lambda = \frac{x_1}{k_B T} \left(\frac{\partial \mu_1}{\partial x_1} \right)_{T,p}, \tag{2.10}$$

where μ_1 is the chemical potential of species 1, k_B Boltzmann's constant and T the temperature.

Unfortunately, a direct comparison between simulated and experimental binary Maxwell-Stefan diffusion coefficients is not always possible for the investigated mixtures due to the absence of experimental data. Nevertheless, it is possible to estimate

the binary Maxwell-Stefan diffusion coefficients from empirical equations that relate the self-diffusion coefficients or infinite dilution binary diffusion coefficients to the binary Maxwell-Stefan diffusion coefficients through simple functions of the composition. Here, three such equations are considered: Darken's equation [42], Caldwell and Babb's equation [18], and Vignes' equation [273].

Darken's equation relates the self-diffusion coefficients of both components D_1 and D_2 to the binary Maxwell-Stefan diffusion coefficient $Đ_{12}$. It can be derived, inserting the equation for the velocity of the center of mass of the total system

$$\mathbf{v}^{cm} = \frac{M_1 \sum_{k=1}^{N_1} \mathbf{v}_1^k + M_2 \sum_{k=1}^{N_2} \mathbf{v}_2^k}{N_1 M_1 + N_2 M_2}, \tag{2.11}$$

into Eq. (2.8) and after some algebraic manipulation the following equation is obtained

$$\begin{aligned} Đ_{12} = \frac{1}{3N x_1 x_2} \int_0^\infty \mathrm{d}t \Big\langle \Big(x_2 \sum_{k=1}^{N_1} \mathbf{v}_1^k(0) - x_1 \sum_{k=1}^{N_2} \mathbf{v}_2^k(0) \Big) \cdot \\ \Big(x_2 \sum_{k=1}^{N_1} \mathbf{v}_1^k(t) - x_1 \sum_{k=1}^{N_1} \mathbf{v}_2^k(t) \Big) \Big\rangle. \end{aligned} \tag{2.12}$$

This equation contains the center of mass velocities of both components and can be separated into the following terms

$$\begin{aligned} Đ_{12} = \frac{1}{3N x_1 x_2} \\ \int_0^\infty \mathrm{d}t \Big[\Big\langle x_2^2 \sum_{k=1}^{N_1} \mathbf{v}_1^k(0) \mathbf{v}_1^k(t) \Big\rangle + \Big\langle x_1^2 \sum_{k=1}^{N_2} \mathbf{v}_2^k(0) \mathbf{v}_2^k(t) \Big\rangle \\ + \Big\langle x_2^2 \sum_{i=1}^{N_1} \mathbf{v}_1^i(0) \sum_{j=1}^{N_1} \mathbf{v}_1^j(t) \Big\rangle + \Big\langle x_1^2 \sum_{i=1}^{N_2} \mathbf{v}_2^i(0) \sum_{j=1}^{N_2} \mathbf{v}_2^j(t) \Big\rangle \\ - x_1 x_2 \Big(\Big\langle \sum_{k=1}^{N_1} \mathbf{v}_1^k(0) \sum_{k=1}^{N_2} \mathbf{v}_2^k(t) \Big\rangle - \Big\langle \sum_{k=1}^{N_2} \mathbf{v}_2^k(0) \sum_{k=1}^{N_1} \mathbf{v}_1^k(t) \Big\rangle \Big) \Big]. \end{aligned} \tag{2.13}$$

The first two terms represent the self-diffusion coefficients of component 1 and 2, respectively. The other four terms represent cross correlations between different particles of the same component, and cross correlations between particles of different components. Keeping only the first two terms from Eq. (2.13) the equation of Darken [42] is obtained

$$Đ_{12} = x_2 \cdot D_1 + x_1 \cdot D_2. \tag{2.14}$$

This equation allows calculating the Maxwell-Stefan diffusion coefficient from self-diffusion coefficients in the mixture, which is only rigourously valid if the assumptions given above hold. It is important to note that the self-diffusion coefficients in the mixture are needed for each studied composition so that Eq. (2.14) is only of limited use for practical applications.

Vignes' equation [273] and Caldwell and Babb's equation [18] relate the Maxwell-Stefan diffusion coefficients to the infinite dilution binary diffusion coefficients D_{12}^{∞} and D_{21}^{∞}. The equation of Caldwell and Babb is given by

$$Đ_{12} = x_2 \cdot D_{12}^{\infty} + x_1 \cdot D_{21}^{\infty}, \tag{2.15}$$

and the Vignes equation [273] by

$$Đ_{12} = (D_{12}^{\infty})^{x_2} \cdot (D_{21}^{\infty})^{x_1}. \tag{2.16}$$

Here, D_{ij}^{∞} is the diffusion coefficient of species i infinitely diluted in species j. In contrast to Darken's equation [42], the equations of Caldwell and Babb [18] and of Vignes [273] need only the two values for the two diffusion coefficients at infinite dilution as input for the whole range of composition, which makes them attractive for practical applications. In the limit of infinite dilution, the binary Maxwell-Stefan diffusion coefficient and the self-diffusion coefficient coincide. This result can be obtained from Eq. (2.14), by taking the limit $x_i \to 0$, i.e. when $x_1 \to 0$ then $Đ_{12} = D_{12}^{\infty} = D_1$, or when $x_2 \to 0$ then $Đ_{21} = D_{21}^{\infty} = D_2$. This equivalence is used to obtain the self-diffusion coefficients in the infinite dilution limit.

Shear and bulk viscosity

The shear viscosity η_s, as defined in Newton's "law" of viscosity, describes the resistance of a fluid to shear forces. It refers to the resistance of an infinitesimal volume element to shear at constant volume [12]. The shear viscosity can also be related to momentum transport under the influence of velocity gradients. From a microscopic point of view, the shear viscosity can be calculated by integration of the time-autocorrelation function of the off diagonal elements of the stress tensor, e.g. J_p^{xy} [91, 245]

$$\eta_s = \frac{1}{Vk_BT}\int_0^\infty \mathrm{d}t\, \left\langle J_p^{xy}(t)\cdot J_p^{xy}(0)\right\rangle, \tag{2.17}$$

where V is the volume, k_B is Boltzmann's constant, T the temperature, and $< ... >$ denotes the ensemble average. The statistics of the ensemble average in Eq. (2.17) can be improved using all three independent off diagonal elements of the stress tensor J_p^{xy}, J_p^{xz} and J_p^{yz}. For a pure fluid, the component J_p^{xy} of the microscopic stress tensor $\mathbf{J}_p$ is given by

$$J_p^{xy} = \sum_{i=1}^{N} m_i v_i^x v_i^y - \sum_{i=1}^{N}\sum_{j>i}^{N} r_{ij}^x \frac{\partial u(r_{ij})}{\partial r_{ij}^y}. \tag{2.18}$$

Here, i and j are the indices of the particles and the upper indices x and y denote the vector components of the particle velocities v_i. Eqs. (2.17) and (2.18) can be applied directly to mixtures.

On the other hand, the bulk viscosity η_b refers to the resistance to dilatation of an infinitesimal volume element at constant shape [12]. The bulk viscosity in polyatomic molecules is related to a characteristic time required for the transfer of energy from the translational to the internal degrees of freedom [111]. Moreover, the bulk viscosity plays an important role to describe ultrasonic wave absorption and dispersion [121]. From a microscopic point of view, the bulk viscosity can be calculated by integration of the time-autocorrelation function of the diagonal elements of the stress tensor and an additional term that involves the product of pressure p and volume V that does not occur in the shear viscosity, cf. Eq. (2.17). The bulk viscosity in the NVE ensemble is given by [91, 245]

$$\eta_b = \frac{1}{Vk_BT}\int_0^\infty \mathrm{d}t\, \left\langle (J_p^{xx}(t) - pV(t))\cdot (J_p^{xx}(0) - pV(0))\right\rangle. \tag{2.19}$$

The component J_p^{xx} of the microscopic stress tensor $\mathbf{J}_p$ is given by

$$J_p^{xx} = \sum_{i=1}^{N} m_i v_i^x v_i^x - \sum_{i=1}^{N}\sum_{j>i}^{N} r_{ij}^x \frac{\partial u(r_{ij})}{\partial r_{ij}^x}. \tag{2.20}$$

The statistics of the ensemble average in Eq. (2.20) can be improved using all three independent diagonal elements of the stress tensor J_p^{xx}, J_p^{yy}, and J_p^{zz}, as well as their permutations. In the case of mixtures Eqs. (2.19) and (2.20) can also be directly applied. These equations are used in many simulation studies on the bulk viscosity, e.g. [16, 105, 106, 117].

Thermal conductivity

The thermal conductivity λ, as defined in Fourier's "law" of heat conduction, characterizes the capability of a substance for molecular transport of energy driven by temperature gradients. It can be calculated by integration of the time-autocorrelation function of the elements of the microscopic heat flow J_q^x, and is given by [91, 245]

$$\lambda = \frac{1}{Vk_BT^2} \int_0^\infty \mathrm{d}t \, \langle J_q^x(t) \cdot J_q^x(0) \rangle. \tag{2.21}$$

Here, the heat flow $\mathbf{J}_q$ for a pure fluid is given by

$$\mathbf{J}_q = \frac{1}{2} \sum_{i=1}^{N} m_i v_i^2 \mathbf{v}_i - \sum_{i=1}^{N} \sum_{j>i}^{N} \left[\mathbf{r}_{ij} : \frac{\partial u(r_{ij})}{\partial \mathbf{r}_{ij}} - \mathbf{I} \cdot u(r_{ij}) \right] \cdot \mathbf{v}_i, \tag{2.22}$$

where $\mathbf{v}_i$ is the velocity vector of particle i and $\mathbf{r}_{ij}$ is the distance vector between particles i and j. The term in squared parentheses denotes the difference between a dyadic product and the unitary tensor $\mathbf{I}$ multiplied by the intramolecular potential energy $u(r_{ij})$. This description of the heat flow is not sufficient for mixtures. In these, both diffusion and energy transport occur coupled [44], so that energy can be transported on a molecular level by diffusion or by heat transport. In a binary mixture with the components α and β the heat flow is given by [91, 274]

$$\mathbf{J}_q = \frac{1}{2} \sum_{k=\alpha}^{\beta} \sum_{i=1}^{N_k} m_i^k (v_i^k)^2 \mathbf{v}_i^k - \sum_{k=\alpha}^{\beta} \sum_{l=\alpha}^{\beta} \sum_{i=1}^{N_k} \sum_{j>i}^{N_l} \left[\mathbf{r}_{ij}^{kl} : \frac{\partial u(r_{ij}^{kl})}{\partial \mathbf{r}_{ij}^{kl}} - \mathbf{I} \cdot u(r_{ij}^{kl}) \right] \cdot \mathbf{v}_i^k - \sum_{k=\alpha}^{\beta} h^k \sum_{i=1}^{N_k} \mathbf{v}_i^k, \tag{2.23}$$

where h^k denotes the partial molar enthalpy of component k. The computation of the heat flow in a binary mixture can, in principle, be accomplished in one simulation, however, here two separate simulations were preferred. One NpT simulation was performed for the computation of the partial molar enthalpies, corresponding to the enthalpic part of the energy flow, and another NVE simulation for the calculation of the autocorrelation function of the heat flow.

The previous expressions for the heat flux, Eqs. (2.22) and (2.23), are valid for atomic fluids. For molecular fluids, the rotational contributions to the heat flux must be also considered. The expression for the heat flow $\mathbf{J}_q$ in molecular pure fluids has been derived by Evans [60] and is given by

$$\mathbf{J}_q = \frac{1}{2}\sum_{i=1}^{N}\left((m_i v_i^2 + \mathbf{w}_i\mathbf{I}_i\mathbf{w}_i + \sum_{j\neq i}^{N} u_{ij})\cdot\mathbf{v}_i\right) - \sum_{i=1}^{N}\sum_{j>i}^{N}\sum_{k=1}^{3}\sum_{l=1}^{3}\mathbf{r}_{ij}\cdot\left(\mathbf{v}_i\frac{\partial u_{ij}}{\partial \mathbf{r}_{kl}} + \mathbf{w}_i\boldsymbol{\Gamma}_{ij}\right), \quad (2.24)$$

where $\mathbf{w}_i$ is the angular velocity vector of molecule i, $\mathbf{I}_i$ the matrix of angular momentum of inertia, u_{ij} the intermolecular potential energy, and $\boldsymbol{\Gamma}_{ij}$ is the torque vector. The torque refers to a reference frame with origin in the molecular center of mass.

2.3 Discussion

In the previous sections an overview of the NEMD methods and a description of the Green-Kubo equations were given. Both methods are compared in the following.

There are numerous direct comparisons between the S-NEMD and BD-NEMD methods and EMD, i.e. the Green-Kubo method, in the literature. For self-diffusion Erpenbeck [52] applied the S-NEMD method (color algorithm) and Green-Kubo method for calculating the self-diffusion coefficient. He found that Green-Kubo yields more precise results for the same number of time steps. Even for simulations with a smaller number of particles a larger simulation time was necessary for S-NEMD compared to Green-Kubo, moreover for large numbers of particles the steady state in S-NEMD became unstable. Both methods showed an influence of the number of particles on the results. Cummings et al. [37] carried out calculations at two strain rates and compared Green-Kubo and Einstein methods with the color field S-NEMD method. They claimed agreement among the three methods, although the values of the S-NEMD method was about 10 % lower than those of the Green-Kubo and Einstein methods. Lee et al. [144] and Moon et al. [192] carried out simulations for liquid water and argon, respectively. Lee et al. [144] found that S-NEMD yields a self-diffusion coefficient about 30 % larger than the one obtained by the Green-Kubo method, while in the work of Moon et al. [192] they agree within the uncertainty of the simulations. In a more recent work of Daivis and Evans [41], it was found that the previous disagreement between the S-NEMD and Green-Kubo was largely due to a poor statistics resulting from short simulations, and they show good agreement between S-NEMD and Green-Kubo methods for self-diffusion coefficients of alkane models. In addition, they remark that self-diffusion coefficients found by both methods increase with increasing number of particles. To overcome

this issue, a correlation for the self-diffusion coefficient as function of the system size was recently given [285]. This method is also used in the present work.

For shear and bulk viscosity, Hover et al. [117] carried out a comparison of the S-NEMD and the Green-Kubo method. Good agreement between the methods was found for the bulk viscosity of argon. On the other hand, for shear viscosity the results of S-NEMD did not agree with those of the Green-Kubo method. Holian et al. [116] and Ryckaert et al. [222] found good agreement between the S-NEMD and the Green-Kubo method. Holian et al. [116] found that shear viscosity calculated by the Green-Kubo method varies with the number of particles by as much as 25 %, while Ryckaert et al. [222] did not find such a dependence but claimed that the statistical uncertainty of S-NEMD decreases with the number of particles proportional to $N^{-1/2}$. More recent work of Lee et al. [144] and Moon et al. [192] for liquid water and argon, Daivis and Evans for liquid butane [41], and Cui et al. [35, 36] for liquid n-decane and n-hexadecane show good agreement between both methods.

Direct comparisons between the NEMD and the EMD method for thermal conductivity are typically more recent than those for self-diffusion coefficients or shear and bulk viscosity. Daivis and Evans [40, 41] carried out a comparison of the S-NEMD and EMD for thermal conductivity of liquid butane. No dependence on the number of particles in any of the methods was found. Using a different type of NEMD method, Palmer [206] calculated the thermal diffusivity of carbon dioxide and water, here also good agreement with the Green-Kubo method was found. Schelling et al. [227] compared S-NEMD and Green-Kubo for the thermal conductivity of silicon. Good agreement between the methods was found. However, they pointed out that for S-NEMD temperature gradients of about 10^9 K/m are necessary, which could introduce significant nonlinear effects. However, in the range of the reported simulations, nonlinear effects were not found. In the work of Schelling et al. [227] using a simulation time of 1 ns, the Green-Kubo method showed uncertainties of 50 %. For the same simulation time S-NEMD showed an uncertainties of only 10 %. Furthermore, they also claim that S-NEMD appears to be advantageous in the computation of thermal conductivity of inhomogeneous systems.

Another related transport coefficient is the Soret coefficient, which is the ratio between the concentration diffusion coefficient (induced by a gradient of concentration or in general chemical potential) and the thermal diffusion coefficient (induced by a temperature gradient) [94, 95]. Perronace et al. [209, 210] calculate the Soret transport coefficient and compared the performance of S-NEMD, BD-NEMD, and Green-Kubo methods. For the mixture Ar+Kr, they report good agreement of S-NEMD and Green-Kubo with each other and experiments. The uncertainty associated with both methods is 30 %. In a second work of the same authors

[210] the mixture n-pentane+n-decane was investigated. S-NEMD, BD-NEMD, and Green-Kubo method were applied to compute the relevant transport coefficients to the Soret effect. It was found that statistical errors of the cross-coefficients using the Green-Kubo method are too high to enable any comparison with experiments, whereas both S-NEMD and BD-NEMD methods have statistical errors of less than 35 %.

S-NEMD methods are generally claimed in the literature to yield better accuracy than EMD methods, i.e. the Green-Kubo method for the calculation of shear viscosity and thermal conductivity for the same computational effort, see e.g. [38, 58, 62, 225]. However, Cui. et al. [36] showed that an adequate selection of the methodology finally depends on the application. If the zero strain rate viscosity is the only property of interest, significantly less computing time is required by S-NEMD than for the Green-Kubo equations. Furthermore, S-NEMD provides other information such as the strain rate dependence of the shear viscosity, molecular conformation, alignment, transient relaxation of the fluid under stress etc. [36]. On the other hand, the Green-Kubo method allows the calculation of all transport coefficient in one simulation run, and the transport coefficients are always those at zero driving force. Moreover, there are many conceptual issues which are not completely clear for the S-NEMD methods; for example the extrapolation of the simulation results to thermodynamic equilibrium [17, 81, 166, 261, 264], the artificial removal of heat from the system [150], and the introduction of periodic effects by the Lees-Edwards periodic boundary conditions [211, 212, 262]. Likewise, BD-NEMD methods suffer also from several limitations. Firstly, they require a larger number of molecules than S-NEMD or Green-Kubo. Secondly, there is a considerable overhead associated with keeping the reservoirs properly populated [8]. In addition, simulations along the bubble line or, more generally, close to phase transition, as the ones carried out throughout this work, can present many technical problems because the nonuniformity of temperature and density within the simulation sample.

Summarizing, the choice between EMD and NEMD is largely a matter of taste and inclination and finally it depends on the application. There are numerous contributions in the literature in which both methods were applied for the calculation of shear viscosity [105, 106, 116, 207, 220, 229], bulk viscosity [16, 100, 117], and thermal conductivity [105, 106, 207, 274, 275] with comparable performance. In the present work, the Green-Kubo method is preferred over NEMD methods, due to the fact that it allows the calculation of several transport coefficients in one simulation run.

Chapter 3

Self-diffusion and binary Maxwell-Stefan diffusion coefficients of real fluids

3.1 Introduction

Diffusion plays an important role in many chemical processes, such as catalysis or adsorption. Traditionally, self-diffusion coefficients and Maxwell-Stefan diffusion coefficients in pure fluids and mixtures are obtained from empirical correlations or with more or less theoretically based equations. Although very successful in practical applications, this approach is limited to the range where correlations were adjusted to experimental data and, thus, by the availability of experimental data to fit such correlations. On the other hand, the measurement of diffusion coefficients is a time consuming and difficult task [124].

With increasing computer power, molecular simulation has become an interesting alternative tool to investigate a wide range of phenomena in many fields of science and engineering, among which diffusion has also been considered. The first simulation works on self-diffusion coefficients date back to the sixties, when Alder and Wainwright [1, 2] carried out simulations with hard spheres and discovered the long-time tail of the velocity correlation function. Furthermore, Jacucci and McDonald [118], Jolly and Bearman, and Schoen and Hoheisel [120, 228], carried out computations of the binary transport coefficients, and investigated the contribution of the cross correlation to the binary Maxell-Stefan diffusion coefficient. These works established the calculation methodology and paved the way for posterior works aimed to predict diffusion coefficients. There are several contributions in which self-diffusion coefficients [172, 177, 220], binary [105, 120, 143, 207, 219, 228, 247, 291] and ternary diffusion coefficients [266, 267] for noble gases, methane and mixtures of these are calculated. Less frequently, investigations with multi-center Lennard-Jones models,

e.g. mixtures of CH_4+SF_6 [113] and CH_4+CF_4 [230], or polar fluids [155, 268] have been performed. With the exception of [177] and [172], all investigations from the literature cover only diffusion coefficients in the liquid phase and only for a limited range of state points. An overview of the available data in the literature for fluids modeled with the spherical LJ and 2CLJQ potentials is given in Table 3.1.

In the first part of this chapter only simple fluids modeled with the spherical Lennard-Jones potential are considered. Self-diffusion coefficients for five pure fluids: Ar, CH_4, Kr, Ne, and Xe (both liquid and gas) and three binary mixtures: Ar+Kr, Ar+Xe, and Kr+Xe (gas) are predicted. The pure component parameters of these models are given in Table 2.1, they were determined from vapor-liquid equilibria data alone [278]. Binary mixtures were modeled using one adjustable parameter for the unlike interaction which was fitted to vapor-pressure data of the mixtures [249, 279]. Throughout the present simulations, the molar mass from the literature is used [213]. Therefore, the diffusion coefficients from the present simulations are predicted from vapor-liquid equilibria alone, and obtained without any adjustment to diffusion or other transport data. In this first part, the studied systems are those for which both molecular models and experimental data were available.

Furthermore, results for more complex molecules are presented. The intermolecular interactions are described by the two-center Lennard-Jones plus point-quadrupole (2CLJQ) potential. Several authors have employed this model successfully, for modeling thermodynamic properties and the self-diffusion coefficients of simple real fluids [23, 112, 191, 276, 278]. Albeit the 2CLJQ potential is not new, the prediction of transport properties with such a model has still not been explored in detail. In order to investigate the suitability and performance of the 2CLJQ potential with respect to self-diffusion coefficients, they were calculated in the present work for several fluids (F_2, N_2, CO_2, CS_2, C_2H_6, C_2H_4, C_2H_2, SF_6) and compared to existing experimental data for these fluids. In addition, self- and Maxwell-Stefan diffusion coefficients for the binary mixtures N_2+CO_2, N_2+C_2H_6, and CO_2+C_2H_6 were studied. These results were used to evaluate the performance of three equations for describing binary Maxwell-Stefan diffusion coefficients, namely the equations of Caldwell and Babb [18], Darken [42], and Vignes [273]. A direct comparison of simulation results to experimental data of binary Maxwell-Stefan diffusion coefficients is not possible for the fluids studied here, because of the lack of such data.

Table 3.1: Literature data for self-, binary, and ternary diffusion coefficients for fluids modeled with spherical LJ and 2CLJQ potentials. EE: Einstein equation. GK: Green-Kubo equation. NEMD:Nonequilibrium molecular dynamics technique.

Author		Year	Method	Ensemble	Model	Fluid
Present work		2006	GK	NVE/NVT	2CLJQ	Binary
Borgelt	[16]	1990	GK	NVE	LJ	Pure
Canales	[19]	1999	EE/GK	NVT	LJ	Pure
Chen	[22]	1977	EE	NVE	2CLJQ	Pure
Cheung	[23]	1975	EE	NVE	LJ	Pure
Erpenbeck	[52]	1987	GK/NEMD	NVT	LJ	Pure
Erpenbeck	[53]	1988	GK	NVT	LJ	Pure
Gardner	[83]	1991	EE	NVE	LJ	Binary
Hammonds	[93]	1988	GK	NVE/NVT	LJ	Pure
Heyes	[99]	1983	EE	NVE	LJ	Pure
Heyes	[102]	1987	EE	NVT	LJ	Pure
Heyes	[103]	1988	EE	NVT	LJ	Pure
Heyes	[104]	1990	GK	NVT	LJ	Pure
Heyes	[105]	1991	EE/GK	NVT	LJ	Binary
Heyes	[106]	1992	GK	NVT	LJ	Binary
Heyes	[107]	1993	GK	NVE	LJ	Pure
Jaccuci	[118]	1975	GK	NVE	LJ	Binary
Jolly	[120]	1980	EE	NVE	LJ	Binary
Kinkaid	[127]	1994	EE/NEMD	NVE	LJ	Pure
Keffer	[122]	2004	EE	NVE/NVT/NPT	LJ	Binary
Keffer	[123]	2004	EE/GK	NPT	LJ	Binary
Lee	[143]	1997	EE	NVE	LJ	Binary
Lee	[145]	2004	GK/NEMD	NVT	LJ	Pure
Meier	[172]	2001	EE	NVE	LJ	Pure
Meier	[173]	2002	EE	NVE	LJ	Pure
Meier	[174]	2004	EE	NVE	LJ	Pure
Michels	[176]	1975	GK	NVE	LJ	Pure
Michels	[177]	1978	GK	NVE	LJ	Pure
Moon	[192]	1991	GK/NEMD	NVT	LJ	Pure
Pas	[207]	1991	GK	NVT	LJ	Binary
Rowley	[219]	1991	GK	NVE	LJ	Binary
Rowley	[220]	1997	EE	NVT	LJ	Pure
Schoen	[228]	1984	EE/GK	NVE	LJ	Binary
Schofield	[231]	1973	GK	NVE	LJ	Pure
Stoker	[247]	1989	GK	NVE	LJ	Binary

Table 3.1: Continued.

Author		Year	Method	Ensemble	Model	Fluid
Straub	[253]	1992	EE	NVE	LJ	Pure
van de ven-Lucassen	[266]	1998	GK/NEMD	NVT	LJ	Ternary
van de ven-Lucassen	[267]	*1999*	GK	NVT	LJ	Ternary
Zhou	[291]	1995	GK	NVE	LJ	Binary

3.2 Results

3.2.1 Self-diffusion coefficients for simple fluids

Fig. 3.1 shows the results for the self-diffusion coefficients of Ar, Kr, Ne compared *with experimental data for gas state points [31].*

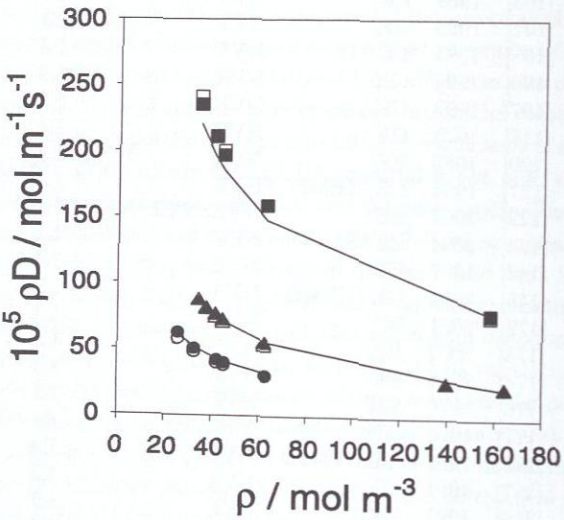

Figure 3.1: *Self-diffusion* coefficients of Ar, Kr, and Ne (gas phase) predicted by molecular simulation compared to experimental data [31] at p=0.1013 MPa. Ar: △ exp., ▲ sim.; Kr: ○ exp., ● sim.; Ne: □ exp., ■ sim. The solid lines represent the results of the correlation of Liu et *al.* [153].

The lines in Fig. 3.1 are the results of the correlation of Liu et al. [153], which is a correlation based on simulation results and experimental data. This correlation is fed with the LJ parameters given in Table 2.1. The data are given at constant pressure and at different temperatures. Fig. 3.2 shows the results for the self-diffusion coefficients for Ar, CH_4, Kr, Ne, and Xe compared with experimental data [13, 27, 96, 185, 208] for liquid state points. The lines in Fig. 3.2 are the results of the correlation of Liu et al. [153] using the LJ parameters from Table 2.1. The data are given at constant temperature and at different pressures. Overall, a very good agreement between the predictions and the experimental data is found. The best results are found for Ar, Kr, Ne in the gas phase with deviations within a few percent. The results for liquid state points show somewhat higher relative deviations from the experimental data (around 10 %). It can be seen that the correlation agrees reasonably well with the simulation data, typical deviations are about 5 %. This accuracy lies in the range claimed by the authors of [153].

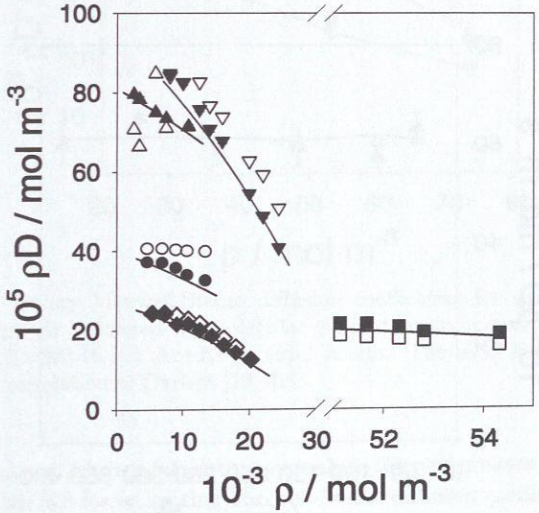

Figure 3.2: Self-diffusion coefficients of Ar, CH_4, Kr, Ne, and Xe (liquid and gas phase) predicted by molecular simulation compared to experimental data [13, 27, 96, 185, 208] at constant temperatures and different pressures. Ar T=323 K: △ exp., ▲ sim.; CH_4 T=298 K:▽ exp., ▼ sim.; Kr T=273 K: ○ exp., ● sim.; Ne T=37 K: □ exp., ■ sim.; Xe T=298 K: ◇ exp., ◆ sim. The solid lines represent the results of the correlation of Liu et al. [153].

3.2.2 Binary Maxwell-Stefan diffusion coefficients for simple fluids

Binary Maxwell-Stefan diffusion coefficients were calculated for the gaseous mixtures Ar+Kr, Ar+Xe, and Kr+Xe. The results are compared to experimental Fick diffusion coefficients. The thermodynamic factor Λ, that relates the Maxwell-Stefan diffusion coefficient to the Fick diffusion coefficient, cf. Eq. (2.9), is assumed to be unity for all cases studied here. This is supported by the calculations of several authors [120, 188, 228, 291]. As a test, Λ was estimated by two simulations to calculate a finite difference [20] for each mixture at the most dense state point. The assumption $\Lambda = 1$ was confirmed within the statistical uncertainty of the calculations.

Fig. 3.3 shows the simulation results for the mixture Ar+Kr in comparison to experimental data taken from [232]. The continuous line in Fig. 3.3 are the results of the correlation of Darken [39, 42]. In this case, the experimental data [269] were reported at constant temperature.

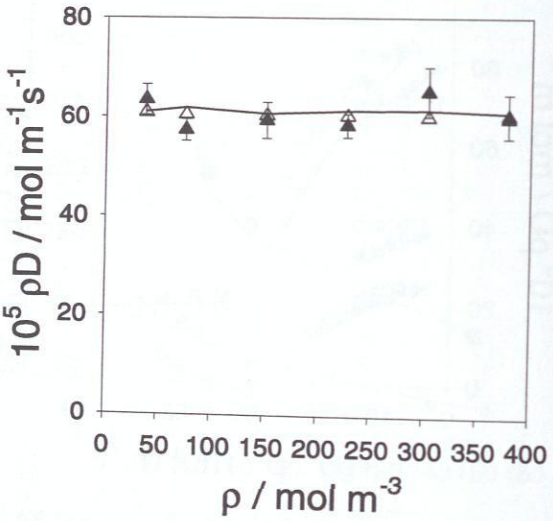

Figure 3.3: Binary Maxwell-Stefan diffusion coefficients for gaseous equimolar mixtures of Ar+Kr predicted by molecular simulation compared to experimental data [232] at T=323.16 K : Ar+Kr △ exp., ▲ sim. The solid lines represent the results of the correlation of Darken [42, 39].

Fig. 3.4 shows the results for the mixtures Ar+Xe and Kr+Xe at constant pressure. Good agreement between the predictions and the experimental values is found. The best results are observed for the mixture Ar+Kr. This mixture shows typical relative deviations of 4 % from the experimental data; the corresponding deviations are 8 % for Ar+Xe, and 16 % for Kr+Xe. It must be pointed out that for the mixture Kr+Xe, no binary interaction parameter ξ was available.

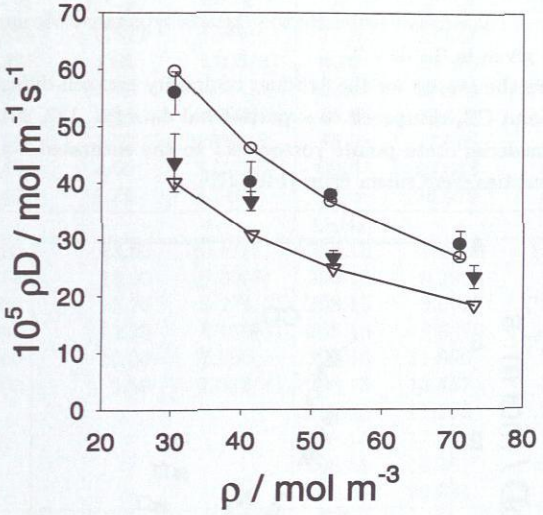

Figure 3.4: Binary Maxwell-Stefan diffusion coefficients for gaseous equimolar mixtures of Ar+Kr predicted by molecular simulation compared to experimental data [232] at T=323.16 K : Ar+Kr △ exp., ▲ sim. The solid lines represent the results of the correlation of Darken [39, 42].

In Figs. 3.3 and 3.4, it is interesting to analyze the performance of the empirical model of Darken [42] for estimating Maxwell-Stefan diffusion coefficients in the gas phase on the basis of known binary self-diffusion coefficients. The figures show that the model of Darken [42] agrees very well with the binary Maxwell-Stefan diffusion coefficients, typical deviations are about 5 %.

3.2.3 Self-diffusion coefficients for quadrupolar fluids

In this section, the predictions for self-diffusion coefficients for quadrupolar fluids are compared to experimental data and to the empirical equation of Liu et al. [153]. The results are presented in terms of the product of self-diffusion coefficient and density rather than the self-diffusion coefficient itself, because the later tends to infinity in the zero density limits. The self-diffusion coefficient is a single-particle property, thus highly accurate data can be obtained with modest computing time. The uncertainty of the present self-diffusion data is typically 3 %, numerical values for all fluids are given in Table 3.2.

Fig. 3.5 shows the results for the product of density and self-diffusion coefficient of F_2, N_2, CO_2, and CS_2 compared to experimental data [54, 132, 204, 284]. For F_2 and N_2, the considered state points correspond to the saturated liquid, for which experimental densities were taken from [146, 270].

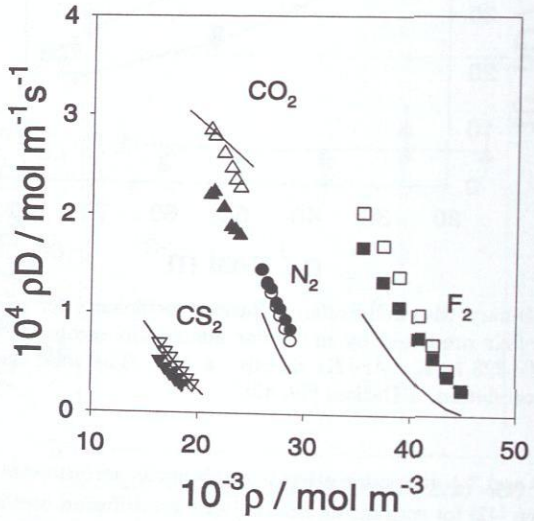

Figure 3.5: Self-diffusion coefficients of F_2, N_2, CO_2, and CS_2 as predicted by molecular simulation in comparison to experimental data [54, 132, 204, 284]. F_2 (saturated liquid, T=54-105 K): □ exp., ■ sim.; N_2 (saturated liquid, T=77-93 K): ○ exp., ● sim.; CO_2 (homogeneous liquid, T= 273 K): △ exp., ▲ sim.; CS_2 (homogeneous liquid, T=298.2 K): ▽ exp., ▼ sim. The lines represent the correlation of Liu et al. [153].

Table 3.2: Self-diffusion coefficients for F_2, N_2, CO_2, CS_2, C_2H_6, C_2H_4, C_2H_2 and SF_6 predicted by molecular simulation compared to experimental data.

F_2				N_2			
T	$10^{-3}\,\rho$	$10^9\,D^{exp.}$	$10^9\,D^{sim.}$	T	$10^{-3}\,\rho$	$10^9\,D^{exp.}$	$10^9\,D^{sim.}$
K	mol · m^{-3}	m^2· s^{-1}	m^2· s^{-1}	K	mol · m^{-3}	m^2· s^{-1}	m^2· s^{-1}
54.0	44.824	0.569	0.569(2)	77.0	28.861	2.526	2.923(8)
62.0	43.497	1.05	0.905(2)	80.0	28.380	2.996	3.309(5)
70.0	42.166	1.69	1.361(3)	83.0	27.870	3.509	3.757(8)
78.0	40.787	2.46	1.903(6)	85.0	27.526	3.875	4.03(1)
88.0	38.968	3.57	2.793(8)	88.0	27.006	4.459	4.63(1)
96.0	37.405	4.55	3.575(6)	90.0	26.643	4.871	4.93(1)
105.0	35.497	5.73	4.74(1)	93.0	26.079	5.522	5.54(1)
CO_2				C_2H_4			
273.0	21.102	13.50	10.41(3)	298.15	4.4955	113.6	110.0(3)
273.0	21.453	13.00	10.39(6)	298.15	6.2923	79.91	76.1(3)
273.0	22.333	11.70	9.274(3)	298.15	8.0927	62.10	56.6(1)
273.0	23.046	10.70	8.156(4)	298.15	9.8895	49.45	42.1(2)
273.0	23.460	10.00	7.890(2)	298.15	11.690	39.58	33.20(8)
273.0	23.900	9.50	7.518(4)	298.15	13.487	31.21	25.5(1)
				298.15	15.283	24.08	19.90(7)
				298.15	17.084	18.20	14.60(3)
				298.15	18.881	13.44	10.70(3)
				298.15	20.681	9.927	7.28(9)
C_2H_6				CS_2			
273.0	15.431	14.6	14.40(4)	298.2	16.489	4.26	3.209(7)
273.0	16.550	11.8	11.71(6)	298.2	17.019	3.64	2.653(8)
273.0	17.968	8.91	9.008(4)	298.2	17.514	3.21	2.264(7)
273.0	18.902	7.24	7.230(2)	298.2	18.031	2.61	1.867(5)
273.0	19.609	6.27	5.870(1)	298.2	18.543	2.23	1.532(5)
C_2H_2				SF_6			
192.0	23.754	3.74	2.91(1)	240.0	12.091	3.35	3.52(3)
197.0	23.463	4.26	3.37(1)	250.0	11.653	3.94	4.28(2)
202.0	23.167	4.82	3.95(1)	260.0	11.221	4.66	4.89(4)
207.0	22.863	5.43	4.35(1)	270.0	10.742	5.59	6.03(2)
212.0	22.554	6.07	4.66(1)	280.0	10.201	6.71	7.49(4)
217.0	22.237	6.76	5.44(1)	290.0	9.606	8.29	8.87(5)
222.0	21.912	7.49	5.95(2)	300.0	8.846	10.5	11.00(2)
310.0	7.826	14.4	14.50(5)				

For CO_2 and CS_2, the state points lie in the homogeneous liquid region at temperatures of 273 K and 298.2 K, respectively. Overall, fair agreement between experimental data and the predictions by molecular simulation is found. The best results are obtained for N_2 with an average deviation of only 6 %. For F_2, the predictions match the experimental data at high densities, at low densities deviations up to 20 % occur. The predictions for CO_2 are too low by about 20 %. For CS_2, the predictions are also too low by about the same amount, in this case the correlation of Liu et al. [153] shows better agreement with the experimental data. It should be noted that the poorer performance of the CO_2 and CS_2 models is reasonable since the three atoms of roughly the same size have not been explicitly considered by the 2CLJQ model.

Fig. 3.6 shows the results for the product of density and self-diffusion coefficient of C_2H_6, C_2H_4, C_2H_2, and SF_6 compared to experimental data [7, 90, 226, 259] and the correlation of Liu at al. [153]. For C_2H_6 and C_2H_4 the considered state points lie in the homogeneous liquid region at temperatures of 273 K and 298.15 K, respectively. For C_2H_2 and SF_6 the states correspond to the saturated liquid, the C_2H_2 densities were taken from [43]. Good agreement with the experimental data is found. The best results are found for C_2H_6 and SF_6 with average deviations of only 2 % and 6 %. For C_2H_2, the predictions of the simulation are too low by about 20 %, for C_2H_4 they are too low by about 15 %. The experimental data of C_2H_4 show a pronounced curvature that is neither reproduced by the simulations nor by Liu's correlation. Liu's correlation is as good as the simulation for SF_6 and C_2H_6, worse than the simulation for C_2H_2, but slightly better for C_2H_4.

To study the dependence of the self-diffusion coefficient on the number of particles, one state point for N_2 at $T = 85$ K, $\rho = 27.526\ 10^3$ mol m^{-3} was chosen. For this state point, a sequence of simulations with increasing number of particles: $N = 108$, 256, 500, 864, and 1372 was carried out. The values for the self-diffusion coefficients were 3.78(6), 3.96(5), 4.03(1), 4.13(2), 4.21(2) in 10^9m$^2\cdot$ s^{-1}, respectively. An estimate of the self-diffusion coefficient for an infinite system size can be obtained by a linear fit of the self-diffusion coefficient data as a function of the inverse box length [285]. This fit yields a value of 4.50(4) 10^{-9} m$^2\cdot$ s^{-1} for an infinitely large system, that is about 10 % greater than the results with $N = 500$ particles. As most predictions of self-diffusion coefficients are below the experimental data, the finite-size correction can improve the agreement with the experimental data for most fluids. Exceptions are F_2, SF_6, and C_2H_6, for which the deviations would increase.

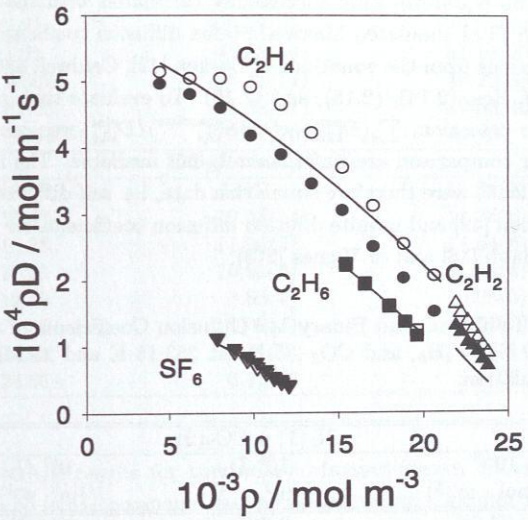

Figure 3.6: Self-diffusion coefficients of C_2H_6, C_2H_4, C_{22}, and SF_6 as predicted by molecular simulation in comparison to experimental data [7, 90, 226, 284]. C_2H_6 (homogeneous liquid, T=273 K): □ exp., ■ sim.; C_2H_4 (homogeneous liquid, T=298.15 K): ○ exp., ● sim.; C_2H_2 (saturated liquid, T= 192-222 K): △ exp., ▲ sim.; SF_6 (saturated liquid, T=240-310 K): ▽ exp., ▼ sim. The lines represent the correlation of Liu et al. [153].

3.2.4 Binary Maxwell-Stefan diffusion coefficients for quadrupolar fluids

In this section, the results obtained for the binary mixtures N_2+CO_2, N_2+C_2H_6, and CO_2+C_2H_6 at 253.15 K and 20 MPa are presented. Numerical data are given in Table 3.3, self-diffusion coefficients of pure fluids in binary mixtures are reported with a statistical uncertainty of about 3 %; binary Maxwell-Stefan diffusion coefficients are reported with statistical uncertainty about 10 %. These mixtures were selected since their vapor-liquid equilibria were successfully calculated with the present molecular models [249]. The simulated Maxwell-Stefan diffusion coefficients are compared with the predictions from the equations of Darken [42], Caldwell and Babb [18], and Vignes [273], cf. Eqs. (2.14), (2.15), and (2.16). To evaluate their performance, the average relative deviation, $\sum_i (Đ_{12,i}^{sim} - DMS_{12,i}^{equation})/Đ_{12,i}^{sim}$, was calculated. Experimental data for comparison are unfortunately not available. The input needed for Eqs. (2.14) to (2.16) were therefore simulation data, i.e. self-diffusion coefficients for Darken's equation [42] and infinite dilution diffusion coefficients for the equations of Caldwell and Babb [18] and of Vignes [273].

Table 3.3: Self-diffusion and Binary MS Diffusion Coefficients of the Binary Mixtures N_2+CO_2, N_2+C_2H_6, and CO_2+C_2H_6 at 253.15 K and 20 MPa Predicted by Molecular Simulation.

$N_2(1) + CO_2(2)$				
x_1	$10^{-3}\ \rho$ (mol · m^{-3})	$10^9\ D_1$ (m^2· s^{-1})	$10^9\ D_2$ (m^2· s^{-1})	$10^9\ Đ_{12}$ (m^2· s^{-1})
0.0	24.08	8.7(9)	6.86(2)	8.7(9)
0.1	22.96	11.57(7)	8.40(3)	11.7(5)
0.2	21.47	14.60(7)	10.55(4)	15.4(3)
0.4	17.73	24.13(10)	16.74(2)	26(1)
0.5	15.59	30.77(8)	21.19(7)	31(1)
0.6	13.60	38.63(6)	26.83(19)	37(2)
0.8	10.90	53.87(20)	38.39(25)	47(3)
0.9	9.968	61.25(20)	44.08(24)	46(3)
1.0	9.356	67.49(13)	43(4)	43(4)

Table 3.3: Continued.

x_1	$10^{-3}\ \rho$ (mol · m^{-3})	$10^9\ D_1$ (m^2· s^{-1})	$10^9\ D_2$ (m^2· s^{-1})	$10^9\ Đ_{12}$ (m^2· s^{-1})
		$N_2(1) + C_2H_6(2)$		
0.0	13.87	20(1)	11.97(4)	20(1)
0.1	13.85	17.39(9)	13.27(2)	18(1)
0.2	13.74	19.58(16)	14.98(4)	18(1)
0.4	12.91	26.48(6)	19.81(11)	26(2)
0.6	11.21	42.88(50)	31.18(20)	39(3)
0.8	9.302	54.42(11)	40.25(38)	48(4)
0.9	8.566	62.88(17)	47.08(40)	48(4)
1.0	8.059	70.21(20)	47(4)	47(4)
		$CO_2(1) + C_2H_6(2)$		
0.0	16.10	13(1)	11.84(1)	13(1)
0.1	16.47	12.38(14)	11.75(6)	13(1)
0.2	16.88	11.98(5)	11.64(6)	13(1)
0.4	17.95	10.93(6)	11.09(8)	13(1)
0.6	19.49	9.63(4)	10.08(6)	12(1)
0.8	21.59	8.09(3)	8.66(9)	10.3(8)
0.9	22.94	7.21(1)	7.78(14)	8.2(7)
1.0	24.66	6.15(6)	5.1(7)	5.1(7)

Fig. 3.7 shows the results for the binary Maxwell-Stefan diffusion coefficients for the mixture N_2+CO_2 compared to the equations of Caldwell and Babb [18], Darken [42], and Vignes [273]. The Maxwell-Stefan diffusion coefficient increases as the mole fraction of N_2 increases due to the smaller size and mass of the N_2 molecule. The simulation results lie above the linear interpolation between the infinite dilution diffusion coefficients, i.e. Caldwell and Babb's equation [18]. Vignes' equation [273] gives a different behavior, with negative deviations from the linear interpolation, whereas Darken's [42] equation predicts positive deviations from the linear interpolation for high N_2 mole fractions and negative deviations for low mole fractions.

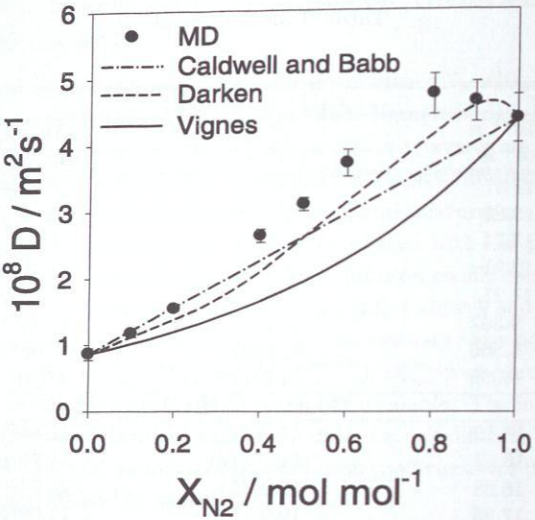

Figure 3.7: Binary Maxwell-Stefan diffusion coefficients for the mixture N_2+CO_2 at 253.15 K and 20 MPa as predicted by molecular simulation in comparison to empirical equations.

Fig. 3.8 shows the results for the binary Maxwell-Stefan diffusion coefficients of the mixture N_2+C_2H_6. In this case, the Maxwell-Stefan diffusion coefficients lie below the linear interpolation of the infinite dilution diffusion coefficients for mole fractions smaller than 0.5 and lie above the linear interpolation for mole fractions larger than 0.5. The results of Darken's equation [42] agree well with the simulation data. The average deviation is only about 6 %. The equation of Vignes [273] fails to reproduce the shape of the curve, which results in an average deviation of about 20 %. The deviations between the simulation results and the correlation of Caldwell and Babb [18] are also about 20 %.

Fig. 3.9 shows the results for the binary Maxwell-Stefan diffusion coefficients of the mixture CO_2+C_2H_6. In this case, the Maxwell-Stefan diffusion coefficients lie above the linear interpolation between the infinite dilution diffusion coefficients (Caldwell and Babb) over the whole composition range. Also, Darken's equation [42] here yields the best results with an average deviation of 12 %, whereas the equations of Caldwell and Babb [18] and of Vignes [273] yield deviations of 23 % and 28 %, respectively. Again Vignes' equation [273] does not reproduce the sign of the deviations from the linear interpolation correctly.

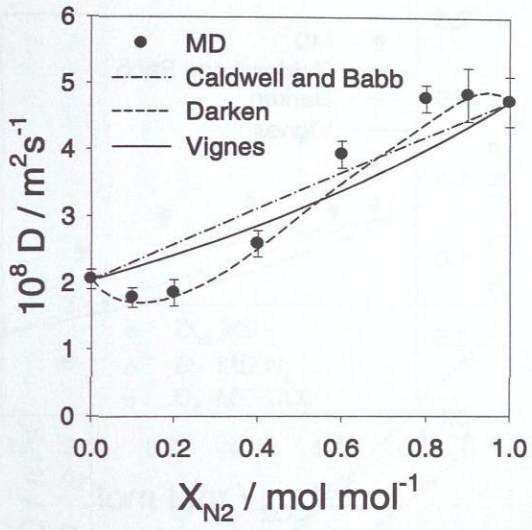

Figure 3.8: Binary Maxwell-Stefan diffusion coefficients for the mixture N_2+C_2H_6 at 253.15 K and 20 MPa as predicted by molecular simulation in comparison to empirical equations.

Figs. 3.7, 3.8, and 3.9 show that the curvature of the Maxwell-Stefan diffusion coefficient is a function of the mole fraction, depending qualitatively on the mixture. It can be concave, with a positive deviation from the linear course, or convex with a negative deviation, or both. The investigated mixtures are not strongly polar, and also in the 2CLJQ models only quadrupolar interactions are present. However, the Maxwell-Stefan diffusion coefficients of these mixtures can not be well represented by the equations of Caldwell and Babb [18] or of Vignes [273], that are often claimed to be adequate for such simple mixtures [273].

Dullien [46] compared the predictions of Vignes' equation [273] with experimental data, and also found that in many cases, where the mixtures were nonassociating, the equation of Vignes [273] was not able to predict the binary Maxwell-Stefan diffusion coefficients correctly. The equation of Darken [42] shows the best performance in all cases. That is because it uses more information than the other two. Moreover, as was shown in Chapter 2, it is exact if the cross correlations between different particles of the same species and particles of different species are neglected. Unfortunately, Darken's equation [42] is of little use for most practical applications.

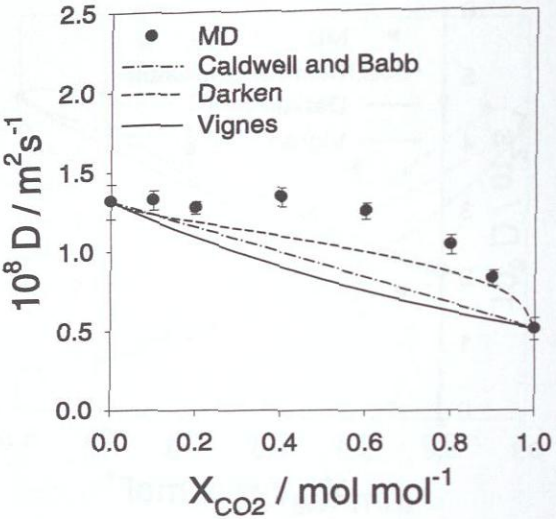

Figure 3.9: Binary Maxwell-Stefan diffusion coefficients for the mixture CO_2+C_2H_6 at 253.15 K and 20 MPa as predicted by molecular simulation in comparison to empirical equations.

3.2.5 Binary self-diffusion coefficients for quadrupolar fluids

Figs. 3.10 to 3.11 show the results for the self-diffusion coefficients of the pure component in the mixture, the called trace diffusion coefficients [39], and the binary Maxwell-Stefan diffusion coefficient for the same mixtures shown in the Figs. 3.7 to 3.9, i.e. N_2+CO_2, N_2+C_2H_6, and CO_2+$C2H_6$ at 253.15 K and 20 MPa.

As Figs. 3.10 to 3.12 show the binary Maxwell-Stefan diffusion coefficients for the mixtures N_2+CO_2 and N_2+C_2H_6 can qualitatively be described by a simple interpolation as indicated by Darken's equation [42], i.e. without the contribution of the cross correlation terms cf. Eq. (2.13). For these mixtures the Maxwell-Stefan lies between the self-diffusion coefficients of both components or very close to one of them. On the other hand, for the mixture CO_2+C_2H_6 , the self-diffusion coefficients are almost equal and below the binary Maxwell-Stefan diffusion coefficient cf. Fig. 3.11. Here the cross correlation terms are significant in the description of the binary Maxwell-Stefan diffusion coefficient, so that Eq. (2.14) results inappropriate.

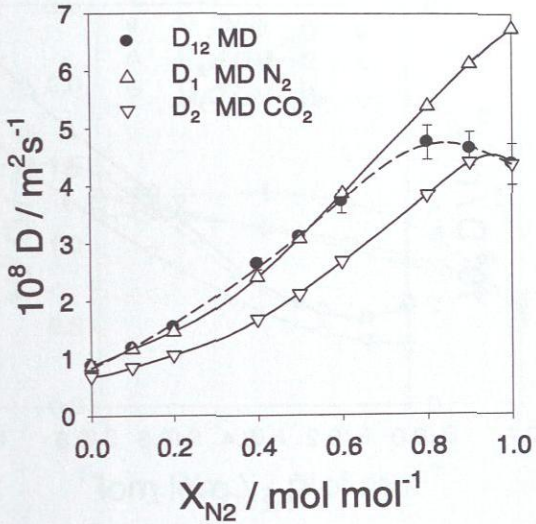

Figure 3.10: Self- and binary Maxwell-Stefan diffusion coefficients for the mixture $N_2(1)$+$CO_2(2)$ at 253.15 K and 20 MPa as predicted by molecular simulation: △ D_1; ▽ D_2; • $Đ_{12}$. The lines serve as guide for the eye.

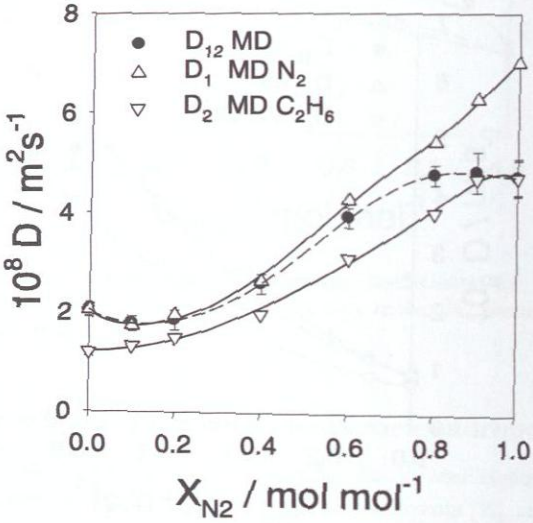

Figure 3.11: Self- and binary Maxwell-Stefan diffusion coefficients for the mixture $N_2(1)$+$C_2H_6(2)$ at 253.15 K and 20 MPa as predicted by molecular simulation: $\triangle$ D_1; $\triangledown$ D_2; $\bullet$ $Đ_{12}$. The lines serve as guide for the eye.

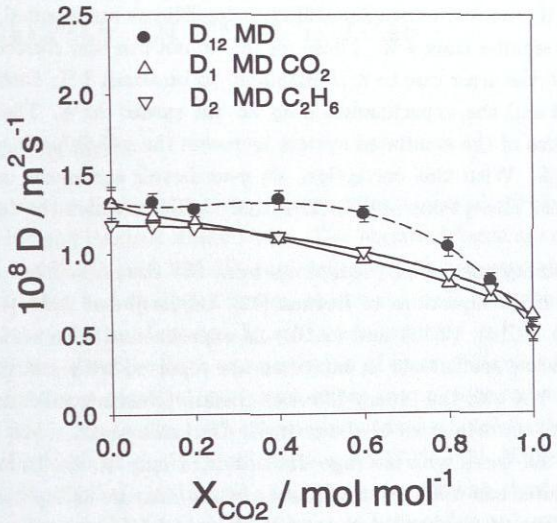

Figure 3.12: Self- and binary Maxwell-Stefan diffusion coefficients for the mixture $CO_2(1)$+$C_2H_6(2)$ at 253.15 K and 20 MPa as predicted by molecular simulation: △ D_1; ▽ D_2; • $Đ_{12}$. The lines serve as guide for the eye.

3.3 Conclusion

In this chapter, molecular dynamics simulation and the Green-Kubo formalism were used to calculate self- and binary Maxwell-Stefan diffusion coefficients for simple fluids modeled the spherical Lennard-Jones potential, and for a class of fluids modeled with the 2CLJQ potential. The potential parameters were taken from the literature [279] where they were adjusted to experimental vapor-liquid equilibria only. Thirteen pure fluids, i.e. Ar, Kr, Ne, CH_4, Xe, F_2, N_2, CO_2, CS_2, C_2H_6, C_2H_4, C_2H_2, and SF_6 and six binary mixtures, i.e. Ar+Kr, Ar+Xe, Kr+Xe, N_2+CO_2, N_2+C_2H_6 and CO_2+C_2H_6, were studied. Self-diffusion coefficients are reported with statistical uncertainties smaller than 1 %. These results do not consider corrections due to the long-time tail; the error due to it is estimated to be about 3 %. Deviations between the predicted and the experimental data do not exceed 20 %. The correction due to the finite size of the simulated system increases the self-diffusion coefficients typically by 10 %. With this correction, an even better agreement can be expected for most fluids. Exceptions are F_2, SF_6, and C_2H_6 for which the deviations would increase.

For the binary mixtures, predictions from the simulations are only compared to results from the equations of Darken [42], Caldwell and Babb [18], and Vignes [273], cf. Eqs. (2.14), (2.15) and (2.16), as experimental data were not available. The self-diffusion coefficients in mixtures are reported with statistical uncertainties less than 1 % and the binary Maxwell-Stefan diffusion coefficients are reported with statistical uncertainties of about 10 %. Darken's equation [42] yields the best agreement in all cases with average deviations of only 10 %. Unfortunately, this equation requires *self-diffusion coefficients* in the mixture as input data. The two simple equations of Caldwell and Babb [18] and of Vignes [273] that use infinite dilution diffusion coefficients as input data, fail to predict the shape and curvature of the composition dependence of the Maxwell-Stefan diffusion coefficients, despite the fairly simple molecules studied here. This indicates that for the prediction of Maxwell-Stefan diffusion coefficients correlations that are more accurate are needed. For their development, molecular simulation is a useful tool, as it can relate molecular properties, i.e. polarity, anisotropy etc., to diffusion coefficients.

Chapter 4

Shear and bulk viscosity and thermal conductivity of real fluids

4.1 Introduction

In this chapter, the prediction of transport properties is extended to consider shear and bulk viscosity, and thermal conductivity. The regarded fluids are modeled with the spherical LJ, 2CLJQ, and 2CLJD potentials. At the present the most comprehensive study that include self-diffusion, shear and bulk viscosity and thermal conductivity of the spherical Lennard-Jones fluid is reported in [172, 173]. Despite of the large number of publications on simulation of transport properties with the spherical Lennard-Jones potential, not much effort seems to have been spent on a comparison of simulation results with experimental data of real fluids. Exceptions are the works of Michels et al. [177] and Heyes et al. [105, 106]. Michels et al. [177] compared the self-diffusion coefficient to the Chapman-Enskog theory and experimental data for Kr and CH_4 at high densities, but thermodynamic properties were not considered. Heyes et al. [105, 106] simulated both transport and thermodynamic properties of Ar+Kr, Ar+CH_4, and CH_4+N_2, but properties of pure fluids were not considered. In other cases [28, 247] more complex molecules like ethylene, carbon dioxide, phenol, alkanes, or carbon tetrachloride were modeled by the spherical Lennard-Jones potential.

For 2CLJQ and 2CLJD potential models, the situation is very different. Here, neither enough simulation results for transport properties not comprehensive comparison with experimental data exist. The 2CLJQ model has successfully been employed by several authors, for the description of static and dynamic (self-diffusion coefficient) thermodynamic properties [23], free energy [234], phase equilibria of pure [154, 223, 224, 276], binary [112, 235, 282], and ternary mixtures [249, 280] at moderated and high pressure, excess properties [76], virial coefficients [158] and

Joule-Thomson inversion curves [21, 29, 30, 279]. Albeit the 2CLJQ potential is not new, the prediction of shear viscosity and thermal conductivity with the 2CLJQ model has up to now not been explored in detail. Only two works report shear viscosity and thermal conductivities for 2CLJ and dipolar spherical LJ, which are particular cases of the 2CLJQ ($Q = 0$, $L = 0$), for a very limited number of states points [114, 155]. For the 2CLJD model the situation is equivalent, this model has been extensively used in the modeling of static thermodynamic properties such as: vapor-liquid equilibria [45, 152, 195, 223, 224, 249], excess properties [129], or surface tension [171, 49]. Also it has been successfully applied to modeling real fluids, yielding good results for vapor-liquid equilibria [128, 130, 152, 250], Joule-Thomson inversion curves [277] virial coefficients [272], and recently also for shear viscosity and thermal conductivity of refrigerants [69]. On the other hand, transport properties for this model class have not been explored systematically. An exception is the work of Lee and Cummings [140] on shear viscosity using the Stockmayer potential [246], which is a subgroup ($L^* = 0$) of the 2CLJD model fluids investigated here. An overview of the available data for shear viscosity, bulk viscosity and thermal conductivity in the literature, for fluids modeled with the spherical LJ, 2CLJQ, and 2CLJD potentials is given in Table 4.1.

Table 4.1: Literature data for shear viscosity of spherical LJ, 2CLJQ, and 2CLJD fluids. EE: Einstein equation. GK: Green-Kubo equation. NEMD: Nonequilibrium molecular dynamics technique.

Author		Year	Method	Ensemble	Model	Fluid	Property
Present work		2006	GK	NVE/NVT	2CLJQ-D	Binary	η_s, η_b, λ
Ashurst	[9]	1975	NEMD	-	LJ	Pure	η_s
Borgelt	[16]	1990	GK	NVE	LJ	Pure	η_s, η_b, λ
Canales	[19]	1999	GK	NVT	LJ	Pure	η_s, η_b, λ
Erpenbeck	[53]	1988	GK	NVT	LJ	Pure	η_s
Evans	[56]	1981	NEMD	NVT	LJ	Pure	η_s
Evans	[59]	1986	NEMD	NVT	LJ	Pure	λ
Evans	[61]	1989	NEMD	NVT	LJ	Pure	η_s
Ferrario	[71]	1991	GK	NVE	LJ	Pure	η_s
Gardner	[83]	1991	EE	NVE	LJ	Binary	η_s, λ

Table 4.1: Continued.

Author		Year	Method	Ensemble	Model	Fluid	Property
Heyes	[98]	1980	NEMD	NVT	LJ	Pure	η_s
Heyes	[99]	1983	EE	NVE	LJ	Pure	η_s
Heyes	[100]	1984	NEMD	-	LJ	Pure	η_b, λ
Heyes	[101]	1986	NEMD	NVT	LJ	Pure	η_s, η_b, λ
Heyes	[102]	1987	EE	NVT	LJ	Pure	η_s
Heyes	[103]	1988	GK	NVT	LJ	Pure	η_s, λ
Heyes	[104]	1990	GK	NVE	LJ	Pure	η_s, λ
Heyes	[105]	1991	EE/GK	NVT	LJ	Binary	η_s, η_b, λ
Heyes	[106]	1992	GK	NVT	LJ	Binary	η_s, η_b, λ
Heyes	[107]	1993	GK	NVE	LJ	Pure	η_s, η_b, λ
Hoheisel	[114]	1990	GK	NVE	2CLJQ	Pure	η_s, η_b, λ
Holian	[116]	1983	GK/NEMD	NVT	LJ	Pure	η_s
Hoover	[117]	1980	GK/NEMD	NVE	LJ	Pure	η_s, η_b
Lee	[139]	1993	NEMD	NPT/NVT	LJ	Binary	η_s
Lee	[140]	1996	NEMD	NPT	1CLJD	Binary	η_s
Lee	[141]	2001	NEMD	NPT	1CLJQ-D	Binary	η_s
Lee	[142]	2001	NEMD	NVT	2CLJ	Binary	η_s
Lee	[145]	2004	EE/GK/NEMD	NPT/NVT	LJ	Pure	η_s, λ
Levesque	[148]	1973	GK	NVE	LJ	Pure	η_s
Levesque	[149]	1987	GK	NVE	LJ	Pure	η_s, λ
Luo	[155]	1991	GK	NVE	2CLJQ	pure	η_s, η_b, λ
Meier	[172]	2001	EE	NVE	LJ	Pure	η_s
Meier	[173]	2002	EE	NVE	LJ	Pure	η_s, η_b, λ
Meier	[175]	2004	EE	NVE	LJ	Pure	η_s
Michels	[184]	1985	GK	NVE	LJ	Pure	η_s
Moon	[192]	1991	GK/NEMD	NVT	LJ	Pure	η_s, λ
Murad	[196]	1991	NEMD	NVT	2CLJ	Pure	λ
Pas	[207]	1991	GK	NVT	LJ	Binary	η_s, η_b, λ
Rowley	[220]	1997	EE	NVT	LJ	Pure	η_s
Schoen	[229]	1985	GK	NVE	LJ	Pure	η_s
Sharma	[233]	1991	-	NVT	LJ	Pure	η_s
Singer	[241]	1980	NEMD	-	LJ	Pure	η_s
Stassen	[244]	1995	GK	NVE	LJ	Pure	η_s
Trozzi	[265]	1984	NEMD	-	LJ	Pure	η_s

The aim of this chapter is the quantitative evaluation of the performance of molecular models [250, 278], which have been optimized for the accurate prediction of vapor-liquid equilibria, in the description of transport properties. In this chapter, EMD is used to carry out a comprehensive comparison, of shear and bulk viscosity and thermal conductivity of pure fluids and binary mixtures of noble gases and methane, quadrupolar and dipolar fluids with experimental data. The molecular models are taken from [250, 278]. These models were adjusted only to vapor-liquid equilibria and yield accurate descriptions of static thermodynamic properties over a wide range of temperatures and densities.

4.2 Results

4.2.1 Shear and bulk viscosity and thermal conductivity of simple fluids

In this section the prediction of shear and bulk viscosity and thermal conductivity are compared pointwise with experimental data. For the shear viscosity the correlation of Rowley et al. [220, 221], which is based on molecular simulation results, was also used.

Fig. 4.1 shows the results for the shear viscosity of Ar, CH_4, Kr, and Xe in comparison with experimental data. Data are reported at different temperatures in homogeneous states and were taken from Vargaftik [270] for the noble gases and from Evers et al. [63] for CH_4. Overall, very good agreement between simulation and experimental data is found. The lowest relative deviations are found for Ar and Kr with a few percent at lower densities. Also the results of shear viscosity of Xe and CH_4 show very good agreement at low density, however, as the density increases, the deviations from the experimental data reach up to about 15 % for Xe and about 20 % for CH_4. It can be observed that the simulations for CH_4, Kr, and Xe tend to underestimate the experimental viscosities as the density increases. This underestimation is larger in the results given by Rowley's correlation for the shear viscosity.

Fig. 4.2 shows the results for the shear viscosity of the binary mixtures Ar+Kr and Ar+CH_4 for two temperatures, the experimental data were taken from Mikhailenko et *al.* [186, 187]. Good agreement between simulation and experimental data is found. For the mixture Ar+Kr the typical deviations are about 10 % and the highest deviations occur for Kr-rich state points. The predictions for the mixture Ar+CH_4 show a better agreement with the experimental data than those for Ar+Kr. Typical deviations of the mixture Ar+CH_4 are about 10 % at 100 K and 6 % at 120 K, simulations performed at one intermediate temperature ($T = 110$ K) confirm that

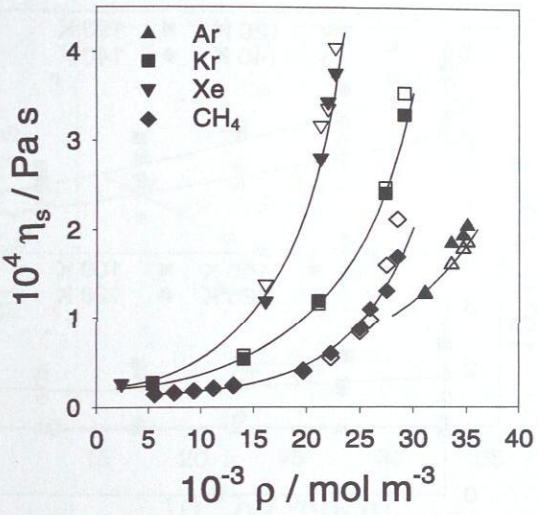

Figure 4.1: Shear viscosity of Ar, CH_4, Kr, and Xe predicted by molecular simulation (full symbols) compared to experimental data (empty symbols) [63, 270]. Ar $T = 300$ K ▲; CH_4 $T = 100$ K - 293.15 K ♦; Kr $T = 230$ K ■; Xe $T = 270$ K ▼; correlation of Rowley et al. [220] — .

better agreement between simulation and experiments is found as the temperature increases. The comparison of the present simulations with previous simulations of Heyes [105, 106], shows a comparable agreement for the mixture Ar+Kr, however, in the mixture Ar+CH_4 the present simulations show better agreement than those of Heyes, specially in CH_4-rich state points, cf. Fig. 4.2.

Fig. 4.3 shows the results for the bulk viscosity of Ar, CH_4, Kr, and Xe in comparison with experimental data. The experimental data are reported at different temperatures and were taken from Cowan et al., Malbrunotet et al., Cowan et al. and Singer [32, 33, 165, 239]. The agreement is poor. Neither the density dependence nor the absolute value of η_b predicted by molecular simulation agrees with the experimental data. The best results for η_b are achieved at the low temperatures and high densities for Kr. In this case the typical error is about 13 %, even here the density dependence in not predicted correctly.

For the other fluids, the predictions are lower than the experimental data by about 50 %. Likewise, the experimental data of bulk viscosity show a stronger dependence on the density than the simulations. It must be pointed out here, however,

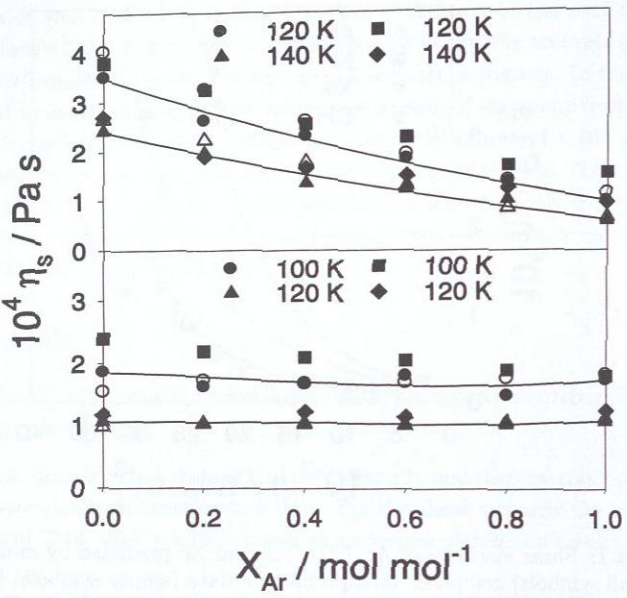

Figure 4.2: Shear viscosity of the mixtures Ar+Kr (top) and Ar+CH_4 (bottom) predicted in the present work by molecular simulation: • T = 100, 120 K, ▲ T = 120, 140 K, compared to simulation data [106]: ♦ T = 120, 140 K, ■ T = 100, 120 K, and experimental (empty symbols) [186, 187]. The lines are a guide for the eye.

that the method to measure the bulk viscosity by means of acoustic absorption of sound waves, involves considerable error [86]. Among the quoted experimental data, the Kr data are claimed to be the most accurate with an error band of about 25 %, for the remainder error bands of up to 40 % can be assumed. In the light of the fact that these simple molecular models describe both the thermal and caloric properties accurately [278] as well as the transport properties self-diffusion [65], shear viscosity and thermal conductivity (see below), it can be argued that the deviations found for the bulk viscosity hints to highly inaccurate measurement.

Fig. 4.4 shows the results for bulk viscosity of the binary mixtures Ar+Kr and Ar+CH_4. The agreement is again poor. Neither the composition dependence nor the absolute value of η_b predicted by molecular simulation agrees with the experimental data. The best results for η_b are achieved at the lowest temperature for the mixture Ar+Kr. In this case, a discrepancy of about 50 % is found. In agreement with the

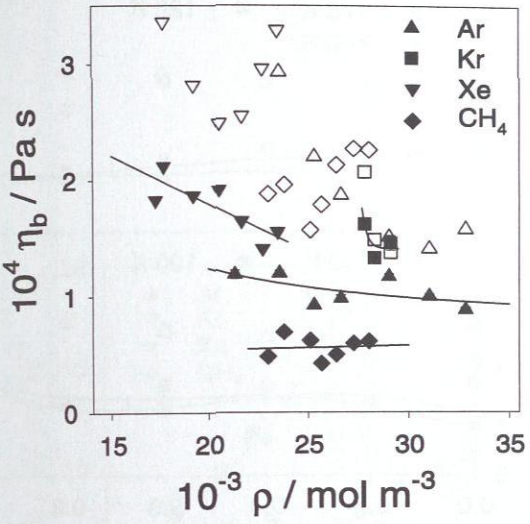

Figure 4.3: Bulk viscosity of Ar, CH_4, Kr, and Xe predicted by molecular simulation (full symbols) compared to experimental data (empty symbols) [32, 33, 165, 239]. The lines are a guide for the eye. Ar T = 100 K - 145 K ▲; CH_4 T = 100 K - 293.15 K ♦; Kr T = 116 K - 130 K ■; Xe T = 165 K - 265 K ▼.

results for pure fluids, it is found that the predictions are much too low in comparison to experimental data. Previous work on these mixtures by Heynes et *al.* [105, 106] confirms lower values from simulation, cf. Fig. 4.4.

Fig. 4.5 shows the results for the thermal conductivity of Ar, CH_4, Kr, and Xe in comparison with experimental data. The data are reported at different temperatures along the bubble line and were taken from Vargaftik et al. [270]. Overall, very good agreement between simulation and experimental data is present. The lowest relative deviations are found for Ar and Xe, typical values are 4 % for Ar and 7 % for Xe. The deviations for Kr and CH_4 reach up to about 20 %, no tendency is observed in these deviations. The good agreement for CH_4 is especially remarkable, considering that the molecular model is very simplified and does not consider the contribution of rotation or internal degrees of freedom [60, 263, 281].

Fig. 4.6 shows the results for the thermal conductivity of the binary mixtures Ar+Kr and Ar+CH_4 for two temperatures, the experimental data were taken from Mikhailenko et al. [186, 187]. In general, good agreement between simulation and experimental data is found. Due to the error introduced by the partial molar en-

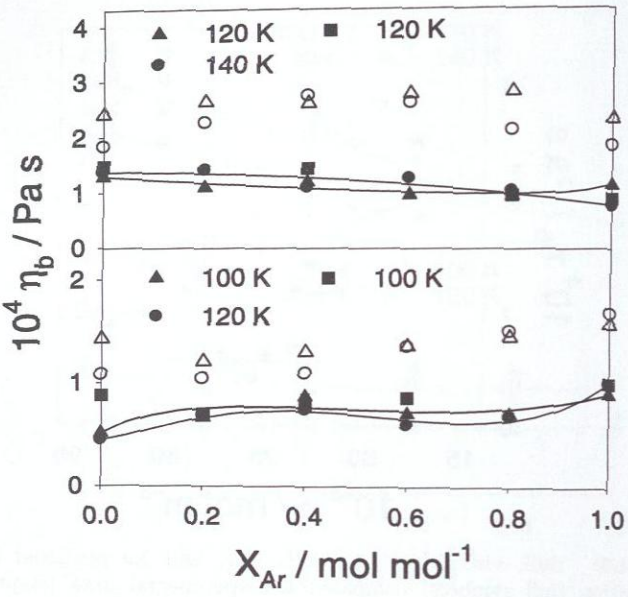

Figure 4.4: Bulk viscosity of the mixtures Ar+Kr (top) and Ar+CH_4 (botton) predicted in this work by molecular simulation: • $T = 120$, 140 K, ▲ $T = 100$, 120 K, compared to simulation data [106]: ■ $T = 100$, 120 K, and experimental data (empty symbols) [186, 187]. The lines are a guide for the eye.

thalpy, the statistical uncertainty of the thermal conductivity was estimated as 5 %. For the mixture Ar+Kr the typical deviations are about 5 % at 120 K, and about 7 % at 140 K. For most of the simulated state points, these deviations lie within the uncertainty bars. For the mixture Ar+CH_4 a better agreement is found than for the mixture Ar+Kr. Over the whole composition range, simulation and experiment for Ar+CH_4 agree within the statistical uncertainties. The comparison of the present simulations with previous simulations of Heynes [105, 106] shows good agreement, cf. Fig. 4.6.

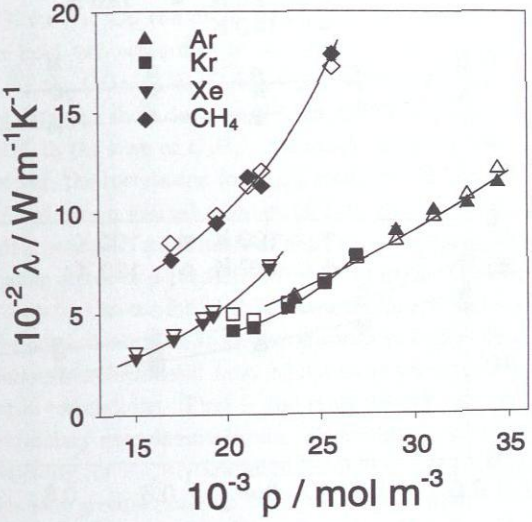

Figure 4.5: Thermal conductivity of Ar, CH_4, Kr, and Xe predicted by molecular simulation (full symbols) compared to experimental data (empty symbols) [270]. The data correspond to bubble points reported at different temperatures. Ar T = 90 K - 140 K ▲; CH_4 T = 100 K - 180 K ♦; Kr T = 140 K - 184 K ■; Xe T = 170 K - 270 K ▼ .

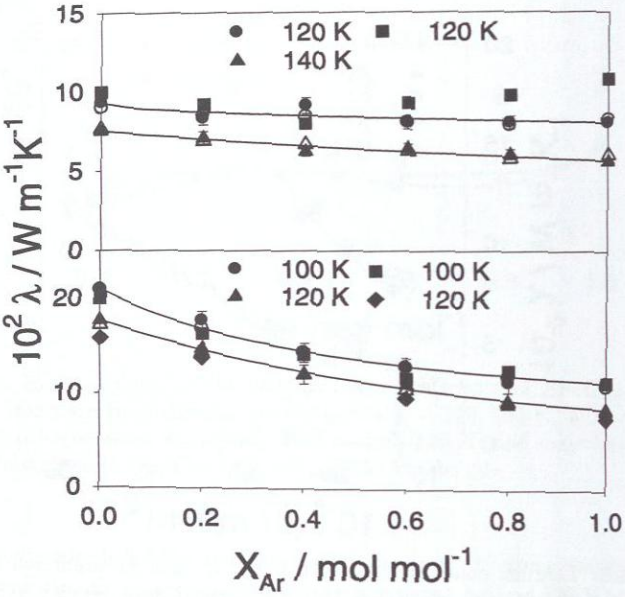

Figure 4.6: Thermal conductivity of the mixtures Ar+Kr (top) and Ar+CH_4 (bottom) predicted by molecular simulation: • T = 100, 120 K, ▲ T = 120, 140 K, compared to simulation data [106]: ■ T = 100, 120 K, ◆ T = 120 K, and experimental data (empty symbols) [186, 187]. The lines are a guide for the eye.

4.2.2 Shear viscosity and thermal conductivity of quadrupolar fluids

In this section, the predictions for shear viscosity and thermal conductivity are compared to correlations of experimental data. In all cases, the studied state points correspond to the saturated liquid. The densities as well as the reference to compare viscosities and thermal conductivities were taken from the REFPROP program of Lemmon et al. [146] provided by NIST. In this program, all correlations for density are based on experimental data and are accurate, deviations vary from 0.05 % for CO_2 to 0.6 % for N_2. *On the other hand, for the viscosities and thermal conductivities* there exist two categories of correlations. In the first category are the correlations for N_2, O_2, CO_2, C_2H_6, C_2H_4, C_2F_6, and C_3H_6; they are entirely based on experimental data and show deviations from the experiment that vary from 2 % for N_2 up to 10 % in the case of C_2H_4. Although, they fit the experimental data within a few percent, the correlation for C_2F_6 could be less reliable than the others because it was fitted over a limited number of data points. In the second category, F_2, C_3H_4, and SF_6, where no experimental data were available, an extended principle of corresponding states in a predictive form was used. These values correspond to information contained in the REFPROP program and it only refers to the liquid state. It must be pointed out that those correlations of experimental data are more accurate than isolated experimental data, because the experimental scatter tends to be compensated in correlations. That is the main reason why they were preferred here in place of primary experimental data. Furthermore, additional experimental data of shear viscosity for F_2 [97] are included in the comparison. For reasons of clarity, the fluids were grouped in Figs. 4.7 to 4.10 according to their density, from low to high.

Fig. 4.7 shows the results for the shear viscosity of C_2F_6, SF_6, C_3H_6, C_3H_4, and C_2H_6. Overall, very good agreement between experiment and simulation is found. With the exception of C_2F_6, almost all results agree within their statistical uncertainties with the correlations. The best results are obtained for C_3H_6 for which the average deviation is only 4 %, for C_3H_4, SF_6, and C_2H_6 the average deviations are lower than 10 %. The poorest results are found for C_2F_6 being systematically too low with an average deviation of 27 %.

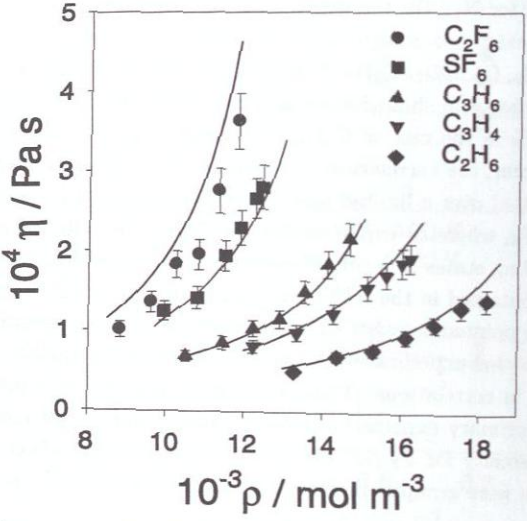

Figure 4.7: Shear viscosity of saturated liquids. The simulations are shown at regular intervals of $0.05T_c$, where T_c is the critical temperature of the fluid. Simulation results: C_2F_6 ($T = 190.5$ - 263.7 K): •, SF_6 ($T = 230.0$ - 286.8 K): ■, C_3H_6 ($T = 219.3$ - 329.0 K): ▲, C_3H_4 ($T = 275.0$ - 362.1 K): ▼, C_2H_6 ($T = 182.5$ - 273.7 K): ♦. Solid lines represent the results of REFPROP. [146].

Fig. 4.8 shows the results for the shear viscosity of C_2H_4, CO_2, N_2, O_2, and F_2. As for the fluids discussed above the agreement between experiment and simulation is within their uncertainties, with the exception of F_2. The best results are obtained for O_2 and CO_2 for which the average deviations are only 4 % and 5 % respectively, whereas for N_2 and C_2H_4 average deviations of up to 10 % occur. On the other hand, for F_2, a fluid for which thermal and caloric properties are well described by the 2CLJQ model [278], systematic deviations from the predictive correlation, with an average of 16 %, are observed. On the other hand, the agreement of the simulations with the experimental data [97], cf. dash line in Fig. 4.8, is practically within the simulation uncertainties, with an average deviation of 5 %. Here the simulations are clearly more accurate than the predictive model, demonstrating the predictive power of the molecular models.

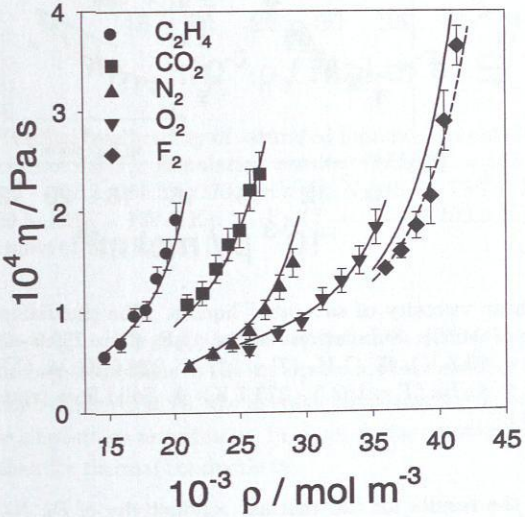

Figure 4.8: Shear viscosity of saturated liquids. The simulations are shown at regular intervals of $0.05T_c$. Simulation results: C_2H_4 (T = 169.4 - 254.1 K): •, CO_2 (T = 218.9 - 273.7 K): ■, N_2 (T = 75.7 - 113.5 K): ▲, O_2 (T = 92.7 - 139.1 K): ▼, F_2 (T = 74.4 - 102.9 K): ◆. The values for F_2 include the correction of the long time tail. Solid lines represent the results of REFPROP [146], and the dashed line represents experimental data for F_2 [97].

Fig. 4.9 shows the results for the thermal conductivity of C_2H_6, C_2F_6, C_3H_4, C_3H_6, and SF_6. Overall, good agreement between experiment and simulation is found. For C_3H_6, C_3H_4, and SF_6 almost all simulation results agree within their statistical uncertainties, for C_3H_6 and C_2F_6 the simulations are too low by about 20 %.

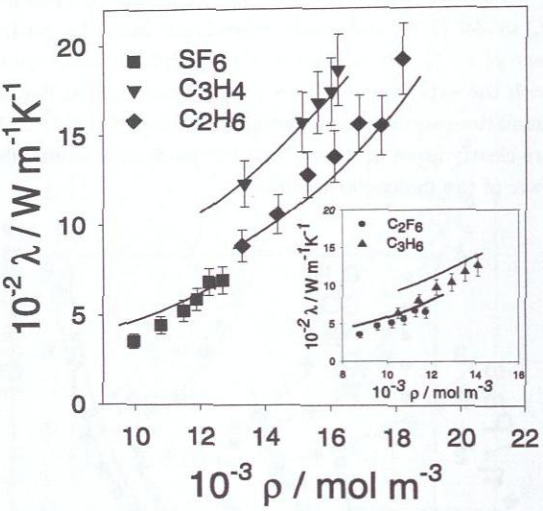

Figure 4.9: Shear viscosity of saturated liquids. The simulations are shown at regular intervals of $0.05T_c$. Simulation results: C_2F_6 (T = 190.5 - 263.7 K): •, SF_6 (T = 223.0, 235 - 286.8 K): ■, C_3H_6 (T = 237.6 - 329.0 K): ▲, C_3H_4 (T = 275.0 - 301.8, 342.0 K): ▼, C_2H_6 (T = 182.5 - 273.7 K): ♦. Solid lines represent the results of REFPROP [146].

In Fig. 4.10 the results for the thermal conductivity of F_2, N_2, O_2, CO_2, and C_2H_4 are presented. Overall, very good agreement between the correlations of experimental data and the simulations is found, the deviations are throughout within the simulation uncertainty. For these five fluids the average deviations between the simulations and the correlations of experimental data are lower than 10 %.

Fig. 4.11 summarizes the results in a bar chart. With the exception of C_2F_6 for shear viscosity, as well as C_2F_6 and C_3H_6 for thermal conductivity, deviations being lower than 10 % from the correlations are observed. These two fluids present deviations that are about two times larger than the average, more over C_2F_6 shows the largest deviations both for shear viscosity and for thermal conductivity. These

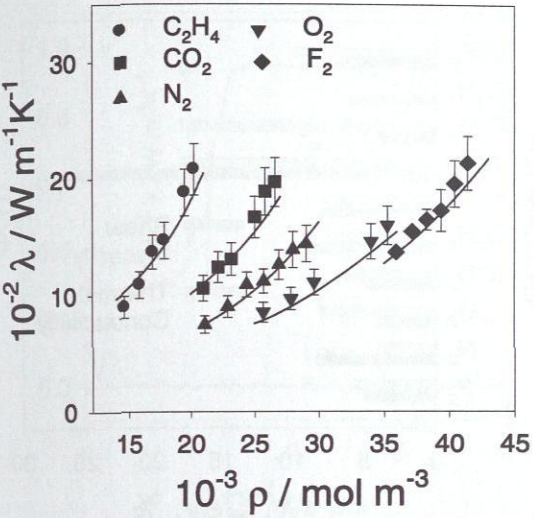

Figure 4.10: Thermal conductivity of saturated liquids. The simulations are shown at regular intervals of $0.05T_c$. Simulation results: C_2H_4 (T = 169.4 - 254.1 K): •, CO_2 (T = 218.9 - 237.2, 255.5 - 273.7 K): ■, N_2 (T = 75.7 - 113.5 K): ▲, O_2 (T = 92.7 - 100.5, 123.7 - 139.1 K): ▼, F_2 (T = 74.4 - 102.9 K): ♦. Solid lines represent the results of REFPROP [146].

larger differences could reside more in the limited data set used in the correlation for C_2F_6 than in the performance of the molecular model used for this fluid. If these two fluids are not considered at all, the average deviations are lower than 7 %, that is lower that the simulations uncertainty. In general, the deviations for viscosity are slightly larger than for thermal conductivity.

4.2.3 Long time behavior of the Green-Kubo integrals

Early simulations of hard spheres of Alder, Gass, and Wainwright [2] suggest the existence of a long time tail in the autocorrelation function of viscosity near the phase boundary to solidification due to the low compressibility of the liquid. This behavior was also found in spherical Lennard-Jones fluid simulations by Levesque, Verlet, and Kürkijarvi [148] and later by Schoen and Hoheisel [229]. This causes problems in the convergence of the Green-Kubo integral, since the correlation function must be calculated over a longer time span. As the F_2 state points correspond to the highest

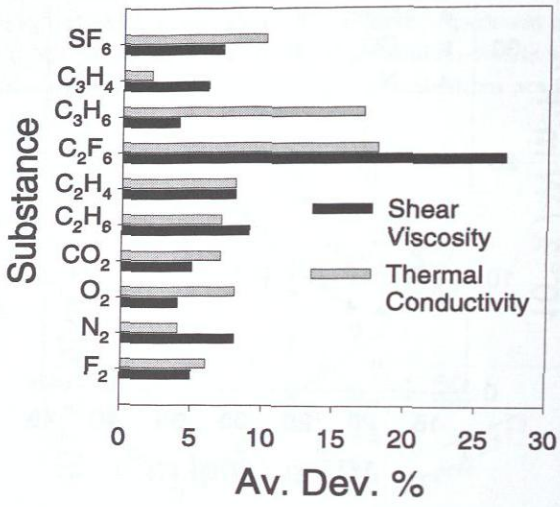

Figure 4.11: Average deviations of shear viscosity and thermal conductivity of saturated liquid F_2, N_2, O_2, CO_2, C_2H_6, C_2H_4, C_2F_6, C_3H_4, C_3H_6, and SF_6 from REFPROP [146].

density among the studied fluids, the convergence of the Green-Kubo integrals is investigated for this substance.

Fig. 4.12 shows the calculated autocorrelation function of thermal conductivity and its integral, cf. Eq. (2.21), at the state point $T = 74.4$ K and $\rho = 41\,424$ mol m^{-3}. These conditions correspond to 92 % of the triple point density (triple point temperature is $T = 53.4$ K). The time correlation function exhibits a fast decay during the first 0.1 10^{-2} ps, afterwards its rises to decay again very fast. The small plot in Fig. 4.12 shows that the Green-Kubo integral converges approximately after 10^{-2} ps within the uncertainty of the simulation. No significant contribution to the integral after 10^{-2} ps was observed.

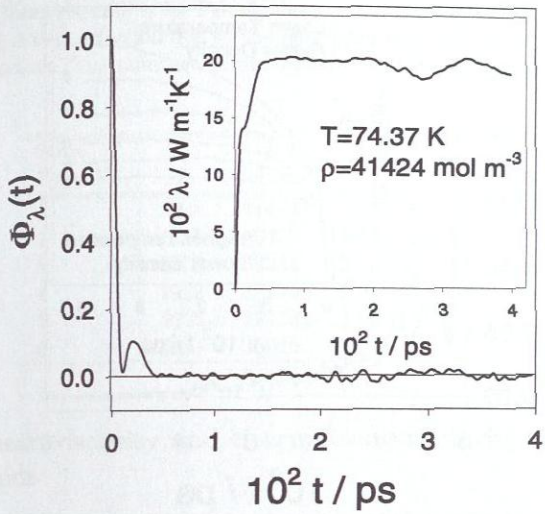

Figure 4.12: Large plot: autocorrelation function of thermal conductivity. Small plot: integral of the autocorrelation function for the thermal conductivity. Both plots are for the most dense simulated state point of saturated liquid fluorine.

The autocorrelation function of shear viscosity is plotted in Fig. 4.13 for the same state point. It does exhibit a long time tail. Its influence on the shear viscosity can better be seen in the small plot in Fig. 4.13, where the integrals for the six saturated liquid densities between $T = 74.4$ and 102.9 K are shown. The corresponding thermodynamic conditions are given in Table 4.2. The simulations for state points 4 to 6 converge approximately after 1.5 10^{-2} ps, that for state point 3 after 2 10^{-2} ps. For state point 2 convergence is reached only after about 3 10^{-2} ps, whereas for state point 1 it is questionable if convergence is reached at all in the simulation run of about 4 10^{-2} ps. In order to overcome this problem with reasonable computational effort, the autocorrelation function of the shear viscosity $\phi(t)=J_p^{xy}(0) \cdot J_p^{xy}(t)/(J_p^{xy}(0) \cdot J_p^{xy}(0))$ was assumed to decay exponentially for times larger than 1.5 10^{-2} ps. Therefore, from 1.5 10^{-2} ps to 4 10^{-2} ps an exponential function of the form $\phi^{fit}(t)= a \cdot \exp(-t/b)$ was fitted to the simulation data and extrapolated to infinity. The choice of an exponential function can be justified by comparison with the Enskog theory [2, 50].

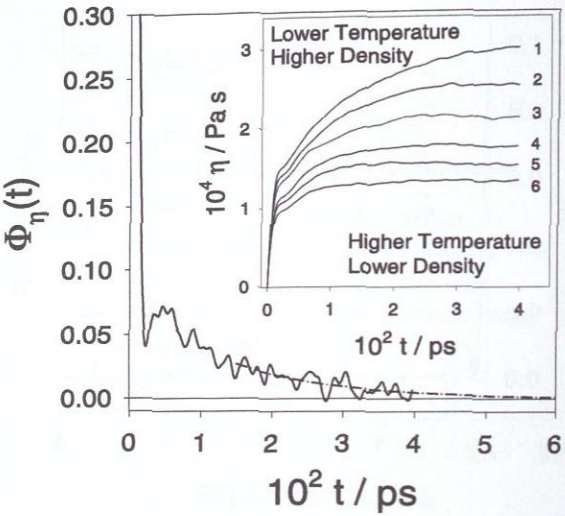

Figure 4.13: *Large plot: autocorrelation function of the shear viscosity* —. *Fitted function* - - - - - . *Small plot: integrals for all six simulated state points of saturated liquid fluorine, numbers 1-6 refer to Table 4.2.*

In this way, the shear viscosity for state points 1 and 2 was estimated as the integral over the autocorrelation function of shear viscosity $\phi(t)$, where it is composed of the explicitly simulated part and the fitted exponential function, i.e. $\phi(t)=\phi^{sim}(t)+\phi^{fit}(t)$. In Table 4.2 the estimated values of the shear viscosity for the state points 1 and 2, together with the contributions of the corrections due to the long time behavior, $\Delta\eta$, are given. The contribution of the long time tail is about 20 % for state point 1, and 10 % for state point 2. These contributions are in the order of magnitude of the statistical uncertainty of the simulations. However, they improve significantly the results indicating clearly that the contribution of the long time tail must be considered for state points close to solidification. Otherwise, a longer calculation of the autocorrelation function is necessary. However, taking into account the inherent simulation uncertainties, which makes difficult to find the point where the correlation function does not contribute any more to the integral, the procedure adopted here is straightforward and economic in terms of computation time.

Table 4.2: Shear viscosity η for F_2 calculated by molecular dynamics without long time tail. $\Delta\eta$ is the correction due to the long time tail, calculated by integration of the fitted function. The numbers in parenthesis denote the uncertainty in the last digits.

State Point No.	T K	ρ mol m^{-3}	η 10^4 Pa s	$\Delta\eta$ 10^4 Pa s
1	74.4	41424	3.01 (20)	0.63
2	80.1	40422	2.54 (30)	0.35
3	85.8	39382	2.13 (30)	
4	91.2	38295	1.84 (13)	
5	97.3	37153	1.59 (7)	
6	103.0	35946	1.42 (3)	

4.2.4 Shear viscosity and thermal conductivity of dipolar fluids

In this section the predictions for shear viscosity and thermal conductivity of dipolar fluids are compared to correlations of experimental data. The investigated state points correspond to the saturated liquid in all cases, taken at regular intervals of 0.1 T_c ranging from 0.6 T_c to 0.9 T_c, where T_c is the critical temperature. Densities as well as viscosities and thermal conductivities for comparison were taken from the REFPROP program of Lemmon et al. [146] provided by NIST. All correlations for density are based on experimental data and are very accurate, deviations vary from 0.05 % for R134a and R143a to 0.1 % for the other regarded fluids. Average deviations from the REFPROP viscosity data vary from 1 % for R11 to 11 % for R41. Similar deviations occur for the correlations of thermal conductivity, varying from 1 % for R11 to 12 % for R41. These values are taken from information contained in REFPROP and only refer to the saturated liquid state. It should be pointed out that the correlations for R41 show the largest average absolute deviations for both viscosity and thermal conductivity. Usually, correlations of experimental data are more accurate than isolated experimental data, because the experimental scatter tends to be compensated by them. Therefore, they were preferred here in place of primary experimental data.

Fig. 4.14 shows the results for the shear viscosity of R11, R12, R123, R134a, and R152a. Overall, good agreement between the correlations of experimental data and simulation is found. However, the molecular models generally tend to underestimate the experimental viscosities: with the exception of R152a, all predictions are below the correlations. The best results are obtained for R152a and R12 for which the

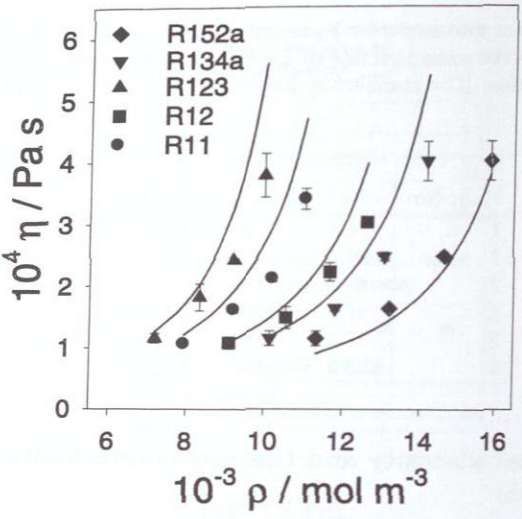

Figure 4.14: Shear viscosity of saturated liquids. Simulation results: R11 (T = 282.7 - 424.0 K): •, R12 (T = 231.1 - 346.6 K): ■, R123 (T = 274.1 - 411.1 K): ▲, R134a (T = 224.5 - 336.8 K): ▼, R152a (T = 231.8 - 347.8 K): ♦. Solid lines represent the results of REFPROP [146].

average deviations are 9 % and 12 %, respectively. The poorest results are found for R11, being systematically too low with an average deviation of 21 %. Fig. 4.15 shows the results for the shear viscosity of R22, R23, R41, R143a, and R142b. The performance of these molecular models is similar to that for the fluids shown in Fig. 4.14. The best results are obtained for R23 and R143a for which the average deviations are only 7 % and 8 %, respectively. For R22 and R41 the average deviations are 10 % and 14 %, whereas for R41 the average deviation raises up to 25 %. Here, the lower accuracy of the correlation for R41 has to be taken into account.

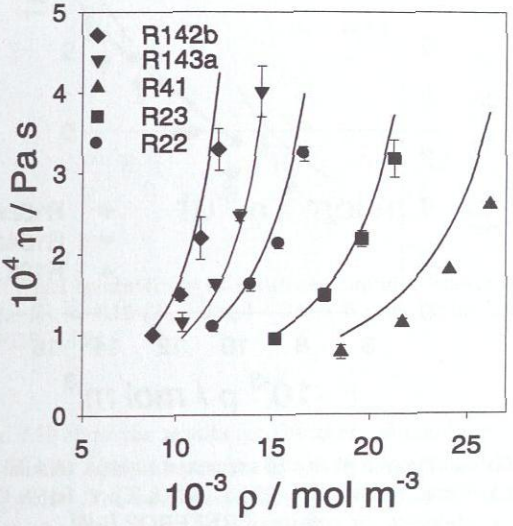

Figure 4.15: Shear viscosity of saturated liquids. Simulation results: R22 (T = 221.58 - 332.37 K): •, R23 (T = 179.6 - 269.3 K): ■, R41 (T = 190.4 - 285.6 K): ▲, R134a (T = 224.5 - 336.8 K): ▼, R142b (T = 246.2 - 369.2 K): ♦. Solid lines represent the results of REFPROP [146].

Figs. 4.16 and 4.17 present the results for thermal conductivity of R123, R134a, R152a, R11, and R12. For the sake of clarity, the results for R11 and R12 are shown in Fig. 4.17. Overall, good agreement between experiment and simulation is found. The best results are observed for R12 and R152a with deviations of only 5 %. For R134a, R11, and R123 the average deviations are 17 %, 18 %, and 22 %, respectively.

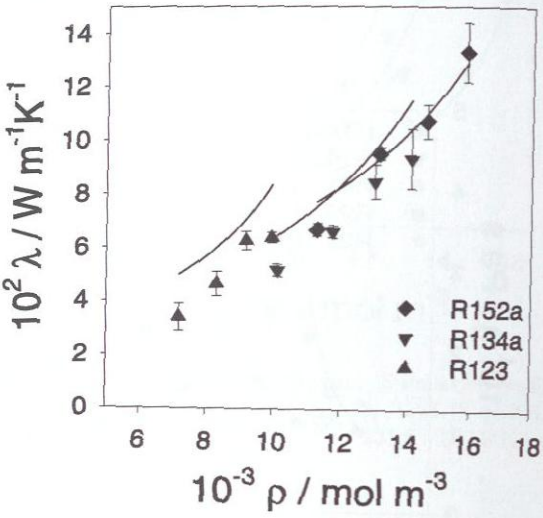

Figure 4.16: Thermal conductivity of saturated liquids. Simulation results: R123 (T = 274.1 - 411.1 K): ▲, R134a (T = 224.5 - 336.8 K): ▼, R152a (T = 231.8 - 347.8 K): ♦. Solid lines represent the results of REFPROP [146].

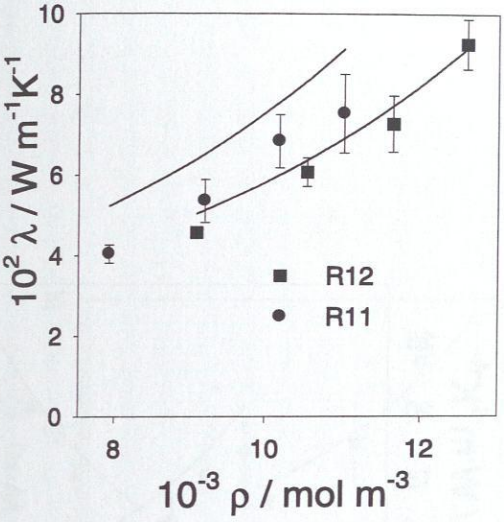

Figure 4.17: Thermal conductivity of saturated liquids. Simulation results: R11 (T = 282.7 - 424.0 K): •, R12 (T = 231.1 - 346.6 K): ■. Solid lines represent the results of REFPROP [146].

Figs. 4.18 and 4.19 show the results for the thermal conductivity of R22, R41, R142b, R23, and R143a. Again for reasons of clarity the results for R23 and R143a are shown in Fig. 4.19. The best results are found for R22, R142b, and R143a. For the two first the deviations are within the simulation uncertainty, while for R23 and R41 deviations are 8 % and 12 %, respectively. As for the shear viscosity, the poorest results are found for R41. A plausible explanation is the lower accuracy of the correlation for R41 as well.

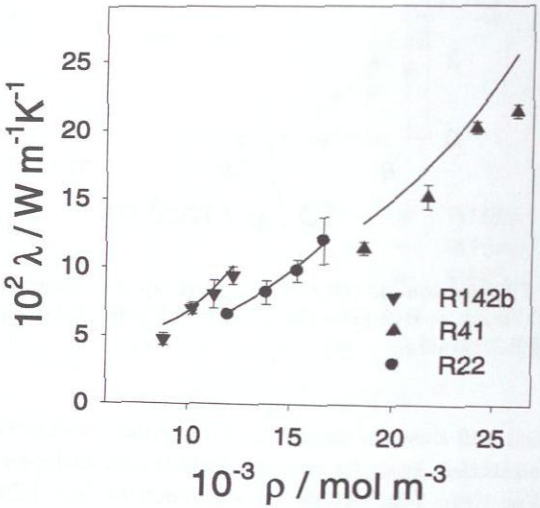

Figure 4.18: Thermal conductivity of saturated liquids. Simulation results: R22 (T = 221.58 - 332.37 K): •, R41 (T = 190.4 - 285.6 K): ▲, R142b (T = 246.2 - 369.2 K): ▼. Solid lines represent the results of REFPROP [146].

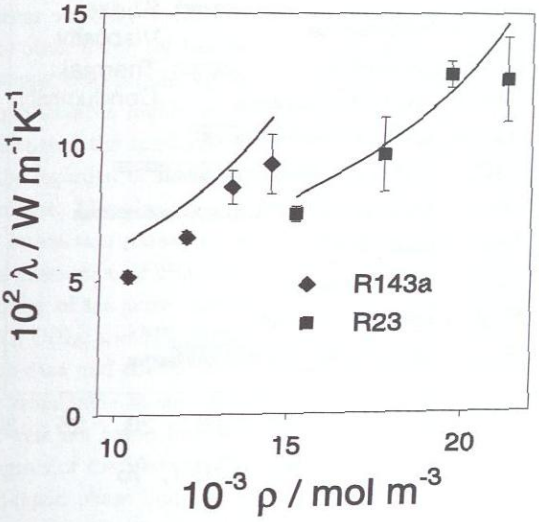

Figure 4.19: Thermal conductivity of saturated liquids. Simulation results: R23 (T = 179.6 - 269.3 K): ■, R143a (T = 224.50 - 336.8 K): ♦. Solid lines represent the results of REFPROP [146].

Fig. 4.20 summarizes all results in a bar chart. The average deviations for shear viscosity and thermal conductivity are 14 % and 11 % with standard deviations of 6 % in both cases. Although the 2CLJD models do not consider any internal degree of freedom, the calculated thermal conductivities show on average a better agreement with the correlations of experimental data than the shear viscosities. The same tendency was also observed in a previous work [68] investigating anisotropic quadrupolar molecules based on the 2CLJQ model.

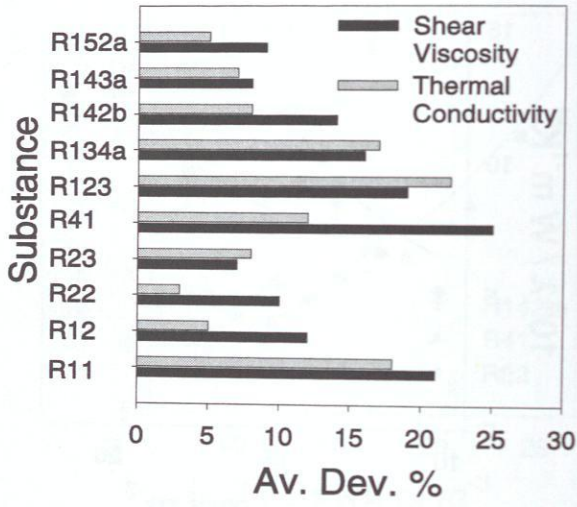

Figure 4.20: Average deviations of simulation results for shear viscosity and thermal conductivity of saturated liquid R11, R12, R22, R23, R41, R123, R134a, R142b, R143a, and R152a from REFPROP [146].

4.3 Conclusion

In this chapter, the Green-Kubo formalism was used to calculate simultaneously shear and bulk viscosity and thermal conductivity of pure nonpolar fluids and their mixtures, and pure quadrupolar and dipolar fluids. All results were compared with available experimental data, correlations of experimental data, and predictive methods.

A comprehensive comparison of predictions for Ar, CH_4, Kr, and Xe, and the binary mixtures Ar+Kr and Ar+CH_4, with available experimental data shows good agreement for shear viscosity and thermal conductivity of pure fluids and binary mixtures. On the other hand, for the bulk viscosity, with the exception of pure Kr, considerable systematic deviations between simulations and experiment occur. This disagreement hints towards highly inaccurate measurements. The present results support the finding that the spherical Lennard-Jones 12-6 potential is an adequate description for the regarded noble gases and also methane, in spite of the simplicity of the used model. Likewise the modified Lorentz-Berthelot combination rules with one binary interaction parameter are an adequate description of the molecular binary unlike interaction. Furthermore, the predictions for shear viscosity and thermal conductivity of ten pure quadrupolar fluids, i.e. F_2, N_2, O_2, CO_2, C_2H_6, C_2H_4, C_2F_6, C_3H_4, C_3H_6, and SF_6 along the bubble line, were compared with available experimental data and correlations. The comparison shows good agreement; this is especially remarkable in the case of thermal conductivity since internal degrees of freedom were not taken into account. In addition, the convergence of the Green-Kubo integrals of thermal conductivity and shear viscosity for state points close to the solid-liquid phase boundary were investigated. The Green-Kubo integral for thermal conductivity converges to its final value quickly (after 10^{-2}) ps. On the other hand, the Green-Kubo integral for shear viscosity shows a slow convergence for state points close to the solid-liquid phase boundary. An approach to overcome this problem is presented. It consists in the extrapolation of the autocorrelation functions for long times with a suitable function; in this case an exponential function was selected. It allows correcting the truncation error of the Green-Kubo integral with low computational cost. This correction contributes up to 20 % in the shear viscosity for the most dense state point studied here. Finally, the predictions for shear viscosity and thermal conductivity of ten dipolar fluids, i.e. R11, R12, R22, R23, R41, R123, R134a, R142b, R143a, and R152a along the bubble line were compared with predictive methods and correlations of experimental data. As the densities were lower than for quadrupolar fluids, no convergence problems were observed, therefore no long time tail corrections were needed. The comparison shows

good agreement. As pointed out before for CH_4, and the quadrupolar fluids, the agreement between simulations and the correlations of experimental data is remarkable, and even more for the regarded dipolar fluids, due to the major complexity of the regarded molecules.

Recent results indicate that even better agreement can be obtained if transport properties are used directly in the parameterization of the molecular potential [74]. On the other hand, the parameterization to vapor-liquid equilibria allows not only the prediction of some static thermodynamic properties but also transport properties with good accuracy.

Chapter 5

Self-diffusion, Shear viscosity and thermal conductivity of 2CLJQ and 2CLJD model fluids

5.1 Introduction

As has been seen in Chapters 3 and 4, molecular simulation is a suitable and genera tool to predict transport properties; likewise it can be used to asses the performanc of empirical equations used to predict transport properties, e.g. the equations of Caldwell and Babb [18], Darken [42], and Vignes [273] in Chapter 3. In the present chapter, molecular simulation is used systematically to investigate the influence of the thermodynamic variables: temperature and density, as well as the molecular parameters elongation and polarity on the self-diffusion, shear viscosity, and thermal conductivity.

Already, since the pioneering work of Alder and Wainwright et al. [1, 2] who used molecular dynamics to investigate transport properties of hard-spheres, the potential of this method has been exploited in the development of more sophisticated theories to predict transport properties. A first step was the discovery of the hydrodynamic long-time tail that implies that the molecular chaos approximation used in the Chapman-Enskog solution of the Boltzmann equation is generally not valid [3], afterward more advanced kinetic theories have been developed by the introduction of the knowledge gained by molecular simulation [78, 125].

Although real fluids usually consist of polar non-spherical molecules, the most extensive studies on transport properties have been done on the basis of very simple molecular models, e.g. hard sphere potential [2, 53], square well potential [178, 179, 180, 181, 182, 183], steeply repulsive potential [108], or spherical Lennard-Jones potential [99, 108].

The 2CLJQ and 2CLJD potentials are very versatile models, capable to cap-

ture the static thermodynamic behavior of real fluids, as it has been demonstrated in the past. 2CLJQ models have extensively been investigated with different approaches, for example: perturbation theory [283], vapor-liquid equilibria of pure substances [250, 278] and mixtures [249, 252, 279]. Furthermore, properties such as Joule-Thomson inversion [277], self-diffusion and binary Maxwell-Stefan diffusion coefficients [67], shear viscosity, and thermal conductivity [68] have reliably been predicted by 2CLJQ models, which were parameterized using only VLE data.

In the same way, static thermodynamic properties of the 2CLJD model fluids have extensively been investigated in the past. There are many results for vapor-liquid equilibria [45, 195, 223, 224, 249], excess properties [129], or surface tension [171, 49]. 2CLJD models have successfully been applied to modeling real fluids as well, yielding good results for vapor-liquid equilibria [128, 130, 152, 250], Joule-Thomson inversion curves [277], virial coefficients [272], and recently also for shear viscosity and thermal conductivity of refrigerants [69].

Despite the number of applications given to these simple potentials, transport properties have not been systematically explored . Exceptions are the series of works of Lee and Cummings [140, 141, 142], which investigated the effect of quadrupolar [141] and dipolar [140] momentum and their mixture, as well as the anisotropy [142] on the shear viscosity. The set of data given in this chapter aim to fill this gap and bring insight in the connection between the molecular parameters of these potentials, and the transport properties.

In this chapter, a systematic study of the influence of anisotropy, i.e. elongation and polarity, i.e. quadrupolar or dipolar momentum on the self-diffusion coefficient, shear viscosity, and thermal conductivity of two-center Lennard-Jones plus point quadrupole (2CLJQ) or dipolar (2CLJD) fluids is carried out. The study is accomplished in the liquid region covering a broad range of temperature and density. Polar and anisotropic effects are studied isolated on each transport property, but also their combined effect. This work is based on the knowledge of accurate vapor-liquid equilibria of 2CLJQ and 2CLJD fluids from [248, 251, 252].

Molecular simulations are carried out along bubble lines for different models over a grid of reduced temperatures. Thus, a consistent comparison of the transport properties of different model fluids is possible and subsequently the effect of the anisotropy and polarity can be identified.

In principle, a specific 2CLJQ model, e.g. for a real fluid like nitrogen, is fully determined by five parameters: σ, ϵ, L, Q [250, 278], and the experimental molar mass M. But in molecular simulation all relevant physical properties can be treated in a reduced form. Here, they are related to σ, ϵ, and M, so that the reduced results are valid for all combinations of these three parameters. In this form, only two

molecular parameters remain, i.e. reduced elongation $L^* = L/\sigma$ and reduced squared quadrupolar momentum $Q^{*2} = Q^2/(4\pi\epsilon_0\epsilon\sigma^5)$; as for M always the experimental molar mass was used. The same procedure was followed for the 2CLJD model. Here, a real substance is also fully determined by five parameters: σ, ϵ, L, μ [248], and the molar mass M. In the reduced form also for this model class only two molecular parameters remain, i.e. reduced elongation $L^* = L/\sigma$ and reduced squared dipolar momentum $\mu^{*2} = \mu^2/(4\pi\epsilon_0\epsilon\sigma^3)$.

Relevant static thermodynamic properties, temperature $T^* = T/(\epsilon/k_B)$ and number density $\rho^* = \rho\sigma^3$, are also reduced in the same way. For sake of brevity, "reduced" will be omitted in the following.

5.2 Investigated models and states

5.2.1 Quadrupolar fluids

For quadrupolar fluids, 30 different model fluids were studied, where each fluid is fully determined by one combination of elongation L^* and quadrupolar momentum Q^{*2}. In Figs. 5.1 and 5.2 four selected systems are shown, they illustrate the covered thermodynamic states and the influence of elongation and quadrupolar momentum on the thermodynamic behavior of the fluids [248]. As Fig. 5.1 shows, critical temperature and density increase with increasing quadrupolar momentum. On the other hand Fig. 5.2 shows that these critical properties decrease with increasing elongation. Such a behavior can also be seen for linear Kihara fluids [271].

The studied model fluids have elongations that vary from $L^* = 0$, i.e. spherical molecules, to 0.8, i.e. strongly elongated dumbbell-shaped molecules, in six steps, i.e. 0, 0.2, 0.4, 0.505, 0.6, 0.8. The odd value $L^* = 0.505$ was chosen to cover the same model fluids as in [248]. Five quadrupolar momenta were studied that range from $Q^{*2} = 0$ to 4 with increments of unity. The upper limit of 4 is sufficient to describe strongly quadrupolar real fluids, e.g. CO_2 with $Q = -3.7938$ DÅ ($Q^{*2} = 3.3037$), C_2H_2 with $Q = 5.0730$ DÅ ($Q^{*2} = 4$), or C_2F_4 with $Q = -7.0332$ DÅ ($Q^{*2} = 3.9272$) [278].

For the sake of consistency, transport properties for spherical fluids, i.e. $L^* = 0$, were treated as two superimposed Lennard-Jones sites. This implies that temperatures have to be divided by 4, as well as the quadrupolar momentum, if a direct comparison with a one-center Lennard-Jones fluid is to be made. The corresponding conversion of self-diffusion coefficient D^*, shear viscosity η^*, and thermal conductivity λ^* for these spherical fluids is obtained dividing the present data by 2.

As temperature and number density in vapor-liquid equilibria vary strongly with the molecular parameters, it is useful to introduce other reduced form for represent-

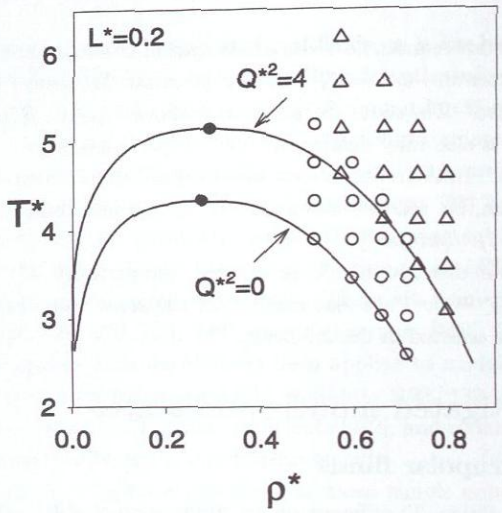

Figure 5.1: Phase diagrams for two selected elongated 2CLJQ fluids ($L^* = 0.2$) where one is non-polar and the other strongly quadrupolar. Saturated densities taken from [252] are represented by the lines joining at the critical point depicted by •. The state points studied in the present work are indicated by ○ for $Q^{*2} = 0$ and by △ for $Q^{*2} = 4$.

ing the temperature $T_R = T^*/T_c^*$ and the density $\rho_R = \rho^*/\rho_c^*$. Here, T_c^* is the critical temperature and $\rho_R = \rho^*/\rho_c^*$ the critical density of the individual 2CLJQ fluid. Values for T_c^* and ρ_c^* where taken from [248]. For each fluid, the considered reduced temperatures along the bubble line range from $T_R = 0.6 - 0.9$ with increments of $\Delta T_R = 0.1$. In addition to those four points, another twelve points in the homogeneous liquid region were simulated (cf. Figs. 5.1 and 5.2). In this way, also isothermal data was generated.

With this grid of points, there are three different views of the data that yield different information. A graphical representation of these three views is given in Fig. 5.2. The first view denoted with the number 1, is along bubble lines. The second denoted with the number 2, is at constant temperature, and the third denoted with the number 3, is at constant density. These three views are presented in the same order for self-diffusion, shear viscosity, and thermal conductivity in the following. The same views are used for the dipolar data, but for them only three points are simulated along the bubble line, therefore only three points at constant temperature are obtained.

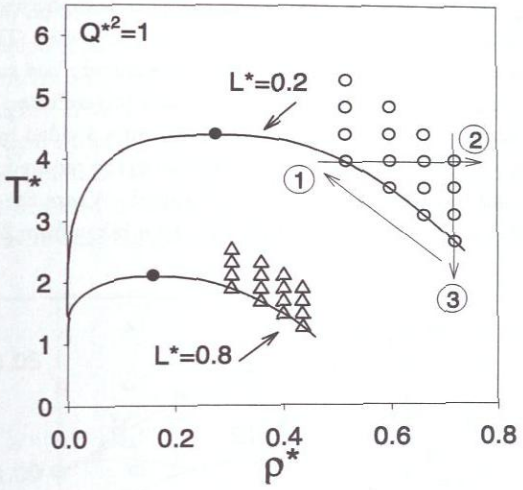

Figure 5.2: Phase diagrams for two selected quadrupolar 2CLJQ fluids ($Q^{*2} = 1$) where one is spherical and the other strongly elongated. Saturated densities taken from [252] are represented by the lines joining at the critical point indicated by •. The state points studied in the present work are depicted by ○ for $L^* = 0$ and by △ for $L^* = 0.8$. The arrows denoted with the numbers from 1 to 3, show the views used to discuss the data in the following.

5.2.2 Dipolar fluids

For dipolar fluids, 38 different were studied, where each fluid is fully determined by one combination of elongation L^* and dipolar momentum μ^{*2}. Simulations at twelve liquid state points were carried out for each model fluid.

The studied model fluids have elongations that vary from $L^* = 0$, i.e. spherical molecules, up to $L^* = 1$, i.e. strongly elongated dumbbell-shaped molecules, in seven steps, i.e. 0, 0.2, 0.4, 0.505, 0.6, 0.8, 1. For Stockmayer fluids, seven dipolar momenta from $\mu^{*2} = 0$ to 20 were considered. For fluids with $L^* = 0.2$, six dipolar momenta from $\mu^{*2} = 0$ to 16 and for larger elongations five dipolar momenta from $\mu^{*2} = 0$ to 12 were taken into account. The upper limit of $\mu^{*2} = 12$ for elongations in the range $L^* = 0 - 1$ is sufficient to describe strongly dipolar real fluids, e.g. $CClF_3$ with $\mu = 1.8261$ D ($\mu^{*2} = 3.4932$), CCl_3F with $\mu = 2.7009$ D ($\mu^{*2} = 3.6250$), or CH_2F-CF_3 with $\mu = 3.0214$ D ($\mu^{*2} = 8.0004$). Very high dipolar momenta from $\mu^{*2} = 16$ to 20 were only consider for fluids with small elongation, because they are realistic only for such molecules [250].

Following the strategy adopted for 2CLJQ fluids, spherical fluids, i.e. $L^* = 0$, were also treated as two superimposed Lennard-Jones sites. Therefore, to compare with one center Lennard-Jones results the temperature has to be divided by 4 as well as the dipolar momentum. Also the values of self-diffusion coefficient D^*, shear viscosity η^*, and thermal conductivity λ^* have to be divided by 2.

In analogy with the previous for 2CLJQ fluids, the reduced form of temperature $T_R^* = T^*/T_c^*$ and the density $\rho_R = \rho^*/\rho_c^*$ was used. Where the critical temperature $T*_c$ and density ρ_c^* of the individual 2CLJD were taken from [248, 252].

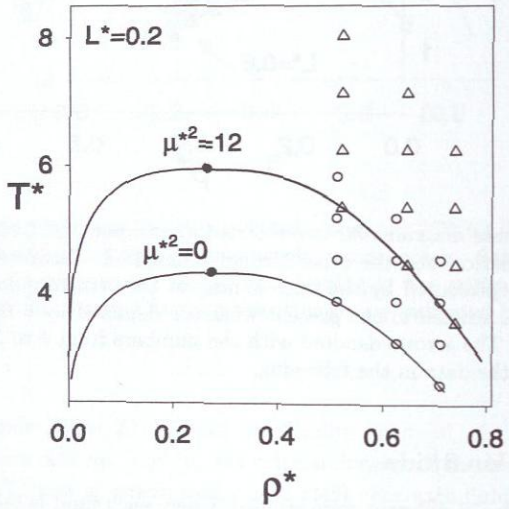

Figure 5.3: Phase diagrams for two selected elongated 2CLJD fluids ($L^* = 0.2$) where one is non-polar and the other strongly dipolar. Saturated densities, taken from [252], are represented by the lines joining at the critical point depicted by •. The investigated state points are depicted by ○ for $\mu^{*2} = 0$ and by △ for $\mu^{*2} = 12$.

For each fluid, three state points along the bubble line were studied from $T_R = 0.6$ to 0.9 with temperature increments of $\Delta T_R = 0.15$. In addition, another nine state points were studied in the homogeneous liquid on three isochors, starting from these three bubble points with temperature increments of $\Delta T_R = 0.15$, cf. Fig.5.3. This grid is less dense than the one used for 2CLJQ fluids, however, as more model fluids are regarded here, both present roughly the same number of data points.

For quadrupolar fluids critical and bubble densities increase monotonously with increasing quadrupolar momentum [248], but dipolar fluids behave different [252].

Fig. 5.4 illustrates the variation of the bubble density, for three reduced temperatures as a function of the dipolar momentum for Stockmayer fluids ($L^* = 0$). As can be seen, the critical density, i.e. bubble density at $T_R = 1.0$, increases up to $\mu^{*2} \approx 3$, but decreases for higher dipolar momenta. At $T_R = 0.9$ and below the critical densities are larger than those of unpolar fluids in all cases. These tendencies are also found for elongated fluids. The influence of elongation on phase behavior does not differ from that observed in quadrupolar fluids, i.e. bubble densities decrease monotonously with increasing elongation [248].

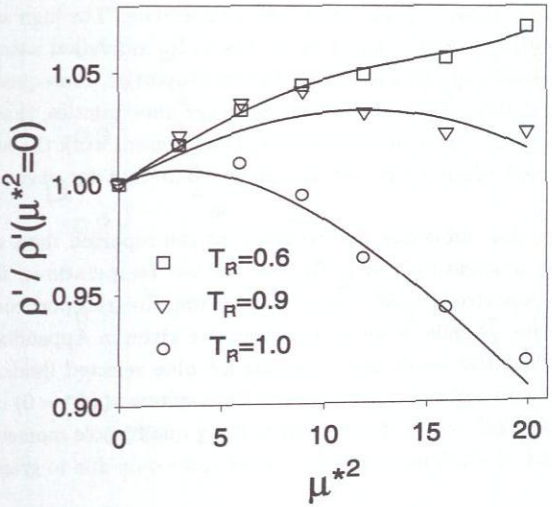

Figure 5.4: Saturated liquid density of Stockmayer fluids ($L^* = 0$) for three reduced temperatures ($T_R = 0.6,\ 0.9,\ 1.0$) as functions of the dipolar momentum. The solid lines indicates the overall correlation in [251], whereas the symbols are from correlations fitted to each model fluids VLE individually.

5.3 Results

5.3.1 Transport properties for 2CLJQ model fluids

In this section, the results for self-diffusion, shear viscosity, and thermal conductivity for the 2CLJQ fluids are presented. Numerical data are given in Appendix B.1 for elongations from $L^* = 0$ to 0.8 and quadrupolar momenta from $Q^{*2} = 0$ to 4. The effects of elongation, quadrupole momentum, temperature, and density are discussed in the following for each transport coefficient separately.

The accuracy of the calculated transport properties decreases in the sequence self-diffusion coefficient, shear viscosity, thermal conductivity. The high accuracy of the self-diffusion coefficient, lower than 3 %, is due to its individual nature [95]. Shear viscosity and thermal conductivity are collective properties, consequently they show for the same simulation time and system size larger uncertainties, that are around 8 and 12 %, respectively. In most simulations of the present work the autocorrelation function of thermal conductivity decays faster than that for shear viscosity, but fluctuate more.

Other factors that influence the accuracy of the reported data are elongation and quadrupolar momentum. In particular, at low temperatures, for fluids with large elongations and strong quadrupolar momentum, the transport coefficients show larger uncertainties. Details of the calculations are given in Appendix A.2.

In the following, the result are discussed for nine selected fluids, covering the hole range of the two molecular parameters, from spherical ($L^* = 0$) over elongated to strong elongated ($L^* = 0.8$) fluids with varying quadrupole momentum $Q^{*2} = 0$, 2, and 4. A subset of six fluids is taken in some cases only due to graphical reasons.

Self-diffusion

Figs. 5.5 and 5.6 illustrate the self-diffusion coefficient along bubble lines for nine selected fluids. The results can either be discussed in terms of reduced density $\rho_R = \rho^*/\rho_c^*$ as in Fig. 5.5 or in terms density ρ^* as in Fig. 5.6. From Fig. 5.5 it can be seen that the regarded range of reduced density is similar for all fluids, but significant deviations from the simple principle of corresponding states are present also for the density. At constant T_R, it can be discerned that the self-diffusion coefficient always decreases with increasing elongation and quadrupolar momentum. A better visibility of the data (which is even more needed for the less accurate properties shear viscosity and thermal conductivity) is obtained when it is plotted over number density in 5.6. Therefore, this graphical representation is preferred as before for 2CLJQ fluids in the following.

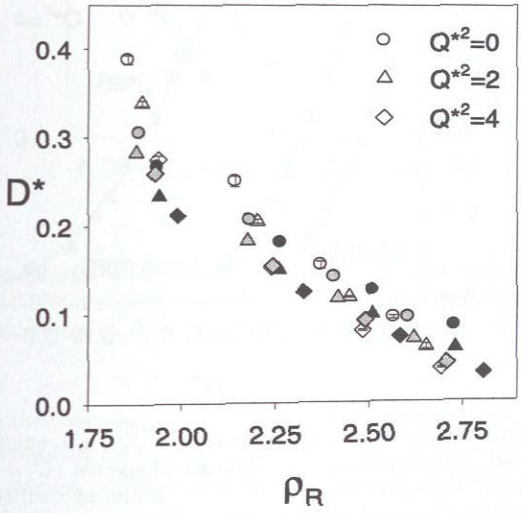

Figure 5.5: Self-diffusion coefficient of spherical ($L^* = 0$, empty symbols) and elongated ($L^* = 0.505$, 0.8, full symbols) 2CLJQ fluids over the reduced density along bubble lines. Reduced temperatures vary from $T_R = 0.6$ to 0.9.

As Fig. 5.6 shows, D^* decreases with increasing density along bubble lines (where with increasing density also the temperature decreases), cf. Fig. 5.2 arrow 1. It is an important result of the present study that the self-diffusion coefficient lies roughly along the same line for a given elongation, independent of the quadrupolar momentum.

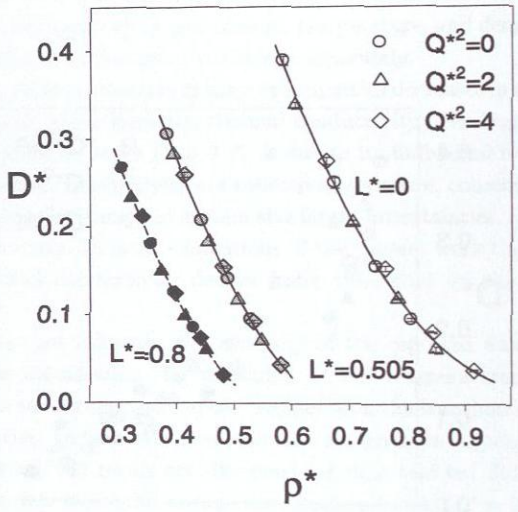

Figure 5.6: Self-diffusion coefficient of spherical ($L^* = 0$, empty symbols), elongated ($L^* = 0.505$, grey symbols), and strongly elongated ($L^* = 0.8$, full symbols) 2CLJQ fluids over density along bubble lines. Reduced temperatures vary from $T_R = 0.6$ to 0.9. Lines are guides for the eye.

Fig. 5.7 shows the dependence of D^* on density for the same nine fluids in the homogeneous liquid region at a constant reduced temperature of $T_R = 0.9$, cf. Fig. 5.2 arrow 2. Note that the density range is the same as in Fig. 5.6. Along this isotherm D^* decreases with increasing density, resembling the behavior of D^* along bubble lines for a given elongation. Comparing D^* along bubble lines with isothermal data for an identical density variation, cf. Fig. 5.6 and 5.7, it is found that the density effect dominates with a contribution of 80 %.

Furthermore, comparing two points with similar density and the same quadrupolar momentum along curves describing different elongations, cf. curves for $L^* = 0.505$ and $L^* = 0.8$ in Fig. 5.7, it can be observed that D^* decreases with increasing elongation.

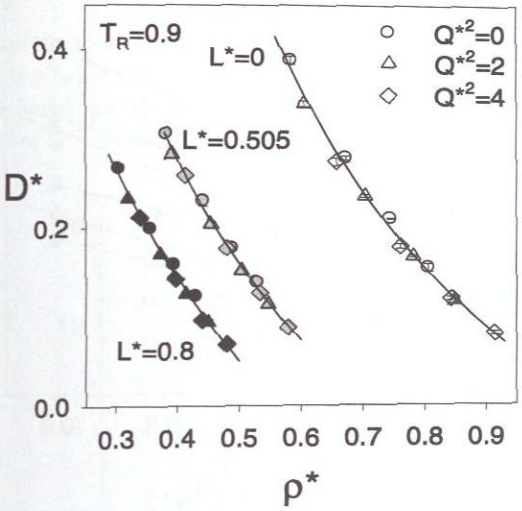

Figure 5.7: Self-diffusion coefficient of spherical ($L^* = 0$, empty symbols) and elongated ($L^* = 0.505$, 0.8, full symbols) 2CLJQ fluids over number density in homogeneous liquid states at $T_R = 0.9$. Lines are guides for the eye.

Fig. 5.8 shows the dependence of the self-diffusion coefficient on temperature at different constant densities for a subset of six fluids. The isochors correspond homogeneous densities starting on the bubble line at the reduced temperature $T_R = 0.6$, cf. Fig. 5.2 arrow 3. Along the isochors the self-diffusion coefficient increases linearly with increasing temperature. The slope of the curves respect to reduced temperature is almost constant for a given elongation, where the less steeply slopes correspond to the more elongated fluids. Such a linear dependence of D^* on temperature has also been reported by other authors for Lennard-Jones fluids [147], Kihara fluids [157], and two-center Lennard-Jones fluids [240].

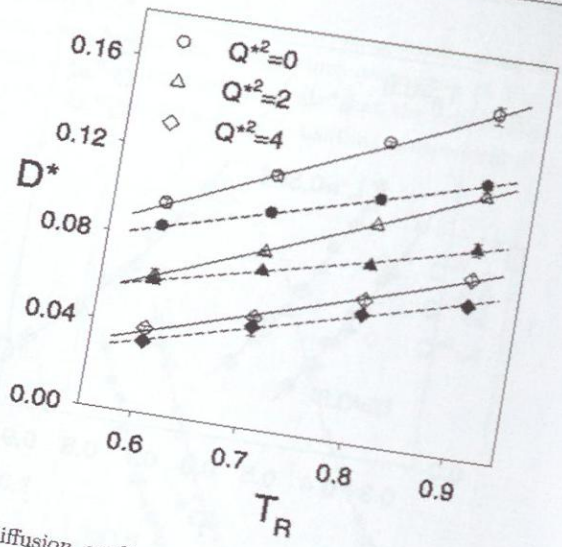

Figure 5.8: Self-diffusion coefficient of spherical ($L^* = 0$, empty symbols) and elongated ($L^* = 0.8$, full symbols) 2CLJQ fluids over reduced temperature in homogeneous liquid states along different isochors. ○: $\rho^* = 0.8062$, △: $\rho^* = 0.8483$, ◇: $\rho^* = 0.9143$, ●: $\rho^* = 0.4302$, ▲: $\rho^* = 0.4513$, ◆: $\rho^* = 0.4800$. Lines are guides for the eye.

Shear viscosity

Fig. 5.9 illustrates the shear viscosity along bubble lines for the nine selected fluids. At constant T_R, it is found that the shear viscosity decreases with increasing elongation. Again it is found that the results for a given elongation lie roughly along one line independent of Q^{*2}, where, as expected, they increase with increasing number density.

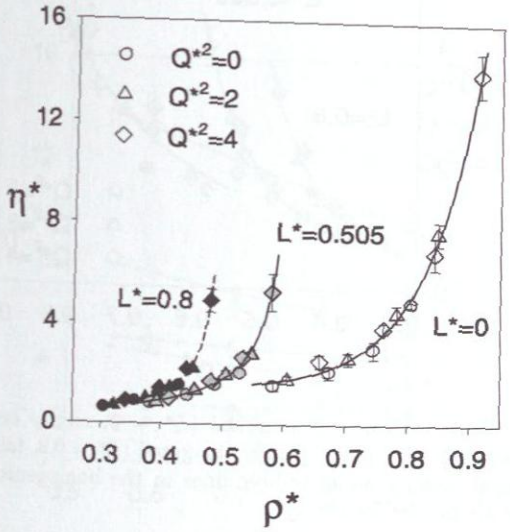

Figure 5.9: Shear viscosity of spherical ($L^* = 0$, empty symbols), elongated ($L^* = 0.505$, grey symbols), and strongly elongated ($L^* = 0.8$, full symbols) 2CLJQ fluids over number density along bubble lines. Reduced temperatures vary from $T_R = 0.6$ to 0.9. Lines are guides for the eye.

The density dependence of shear viscosity in the homogeneous liquid region is illustrated in Fig. 5.10 at $T_R = 0.9$. Comparing the variation of η^* along bubble lines and along isotherms in the same way as for D^*, it is found for non-polar fluids that the density effect is responsible for about 80 % of the increase of η^* along the bubble line. For quadrupolar fluids, however, the temperature influence becomes more important and its contribution is about 40 %. Furthermore, comparing two points with similar density and the same quadrupolar momentum along curves describing different elongations, cf. curves for $L^* = 0.505$ and $L^* = 0.8$ in Fig. 5.10, it can be observed that η^* increases with increasing elongation. Moreover, a closer look

at two points with similar density along the curve $L^* = 0$ shows a trend to higher values of η^* for fluids with stronger quadrupolar momentum.

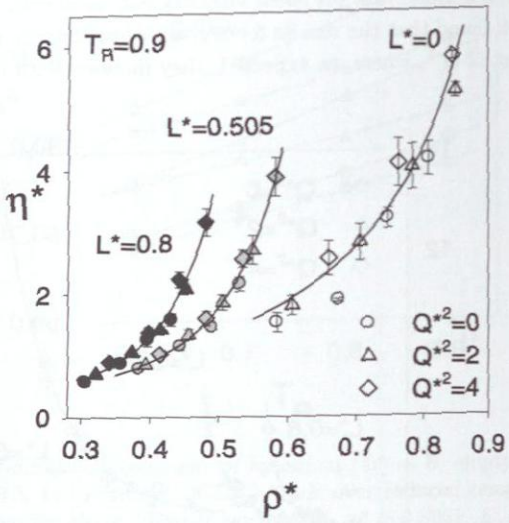

Figure 5.10: Shear viscosity of spherical ($L^* = 0$, empty symbols), elongated ($L^* = 0.505$, grey symbols), and strongly elongated ($L^* = 0.8$, full symbols) 2CLJQ fluids over number density along bubble lines in the homogeneous liquid state at $T_R = 0.9$. Lines are guides for the eye.

Fig. 5.11 shows the dependence of shear viscosity on reduced temperature for a subset of six fluids along isochors with similar values in terms of ρ_R. As expected, shear viscosity decreases with increasing temperature. Strongly quadrupolar fluids, with an about threefold higher shear viscosity in the cold liquid, are more sensitive to temperature, exhibiting larger slopes.

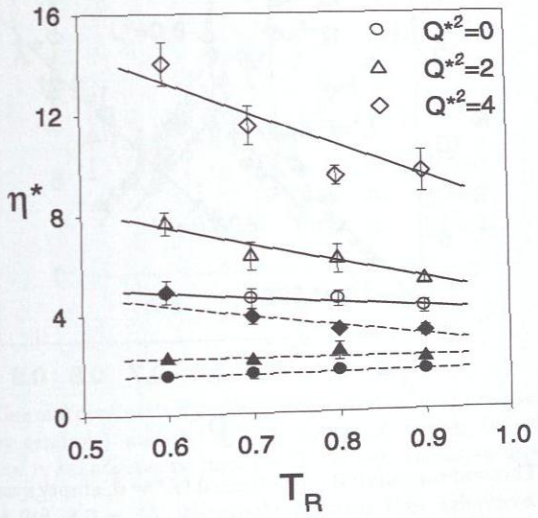

Figure 5.11: Shear viscosity of spherical ($L^* = 0$, empty symbols) and strongly elongated ($L^* = 0.8$, full symbols) 2CLJQ fluids over reduced temperature in homogeneous liquid along different isochors. ○: $\rho^* = 0.8062$, △: $\rho^* = 0.8483$, ◇: $\rho^* = 0.9143$, ●: $\rho^* = 0.4302$, ▲: $\rho^* = 0.4513$, ◆: $\rho^* = 0.4800$. Lines are guides for the eye.

Thermal conductivity

Fig. 5.12 illustrates the thermal conductivity along bubble lines for the nine selected fluids. Again, the data lie roughly along single lines for a given elongation, but considering simulation uncertainties not more than a linear dependence can be discerned. Thermal conductivity has the same basic trends like shear viscosity.

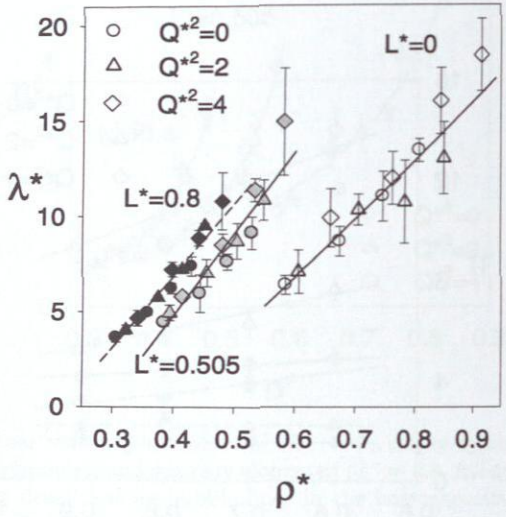

Figure 5.12: Thermal conductivity of spherical ($L^* = 0$, empty symbols), elongated ($L^* = 0$, grey symbols), and strongly elongated ($L^* = 0.8$, full symbols) 2CLJQ fluids over density along bubble lines. Reduced temperatures vary from $T_R = 0.6$ to 0.9. Lines are guides for the eye.

Fig. 5.13 shows the density dependence in the homogeneous liquid at $T_R = 0.9$. It can be seen that the curves resembles those along bubble lines, underlining the dominant effect of density there. Furthermore, comparing two points with similar density and the same quadrupolar momentum along curves describing different elongations cf. Fig. 5.13, it can be observed that λ^* increases with increasing elongation. Similar results have been reported by Tokumasu et al. [263] who studied the nonpolar 2CLJ potential but at different thermodynamic conditions. In their analysis, Tokumasu et al. reduced λ^* by critical temperature and critical density, to isolate the effect of elongation and found that this type of reduced thermal conductivity increases with increasing elongation.

Taking a closer look at two points with similar density along the curve $L^* = 0$ or $L^* = 0.505$ in Fig. 5.13 reveals a trend to higher values of λ^* for fluids with stronger quadrupolar momentum.

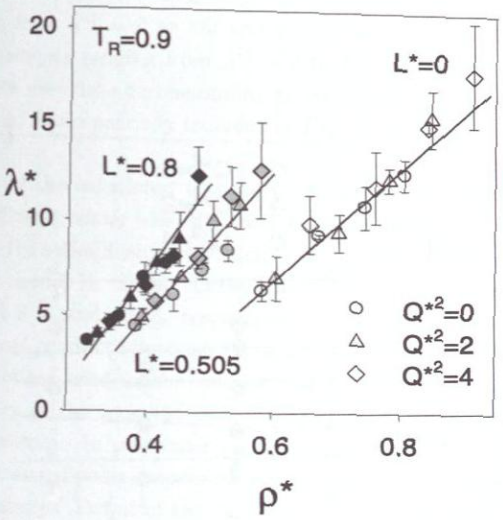

Figure 5.13: Thermal conductivity of spherical ($L^* = 0$, empty symbols), elongated ($L^* = 0.505$, grey symbols), and strongly elongated ($L^* = 0.8$, full symbols) 2CLJQ fluids over density in homogeneous liquid at $T_R = 0.9$. Lines are guides for the eye.

Fig. 5.14 shows isochoric data with similar values in term of ρ_R for a subset of six fluids, where the effect of temperature on λ^* is small. Taking the statistical uncertainty and the scatter of the data into account, hardly any trend can be discerned. Experimental results [242, 243] show that thermal conductivity at constant density increases with increasing temperature, but the variation is very small in the liquid region. However, an increase of λ^* with increasing quadrupole momentum can be seen.

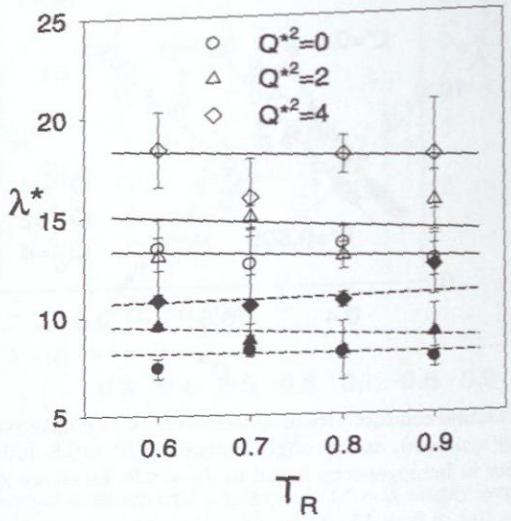

Figure 5.14: Thermal conductivity of spherical ($L^* = 0$, empty symbols) and strongly elongated ($L^* = 0.8$, full symbols) 2CLJQ fluids over reduced temperature in homogeneous liquid along different isochors. ○: $\rho^* = 0.8062$, △: $\rho^* = 0.8483$, ◇: $\rho^* = 0.9143$, ●: $\rho^* = 0.4302$, ▲: $\rho^* = 0.4513$, ◆: $\rho^* = 0.4800$. Lines are guides for the eye.

5.3.2 Transport properties for 2CLJD model fluids

Numerical data for self-diffusion coefficients, shear viscosity, and thermal conductivity for the 2CLJD fluid are given in the Appendix B.2, for spherical fluids with dipolar momenta from $\mu^{*2} = 0$ to 20, for slightly elongated fluids $L^* = 0.2$ with dipolar momenta from $\mu^{*2} = 0$ to 16, and for elongated fluids from $L^* = 0.4$ to 1 with dipolar momenta ranging from $\mu^{*2} = 0$ to 12. As before for 2CLJQ fluids, the discussion here uses data corresponding to state points along bubble lines, and homogeneous liquid states partially included in Figs. 5.17, 5.18, 5.20, 5.21, 5.23, and 5.24.

The accuracy of the calculated transport properties decreases in the sequence self-diffusion coefficient, shear viscosity, and thermal conductivity. Again the results obtained for the self-diffusion coefficient are the most accurate, with statistical uncertainty lower than 3 %. Shear viscosity and thermal conductivity show uncertainties of around 8 % and 12 %, respectively. This set of data is slightly more accurate for thermal conductivity than those for 2CLJQ, due to the larger number of correlation functions used in the calculations. In the same way as for 2CLJQ fluids, the accuracy of the reported data depends on the sate points, elongation, and dipolar momentum. In particular, at low temperatures, for fluids with large anisotropy and strong dipolar momentum, the transport coefficients show larger simulation uncertainties. Detail of the calculation is given in Appendix A.2.

Self-diffusion

Figs. 5.15 and 5.16 illustrate the self-diffusion coefficient along the bubble line for ten selected fluids. The results can either be discussed in terms of reduced density ρ_R as in Fig. 5.15 or in terms of number density ρ^* as in Fig. 5.16. From Fig. 5.15 it can be seen that the regarded range of reduced density is similar for all fluids, but here even more significant deviations from the simple principle of corresponding states of two parameters are also present for the density. At constant T_R, it can be discerned that the self-diffusion coefficient always decreases with increasing elongation. The dipole, however, can either decrease or increase the self-diffusion coefficient. A better visibility of the data (which is even more needed for the less accurate properties shear viscosity and thermal conductivity) is obtained when plotted over number density in Fig. 5.16. Therefore, this graphical representation is preferred in the following.

As Fig. 5.16 shows, D^* decreases with increasing number density along the bubble line. Self-diffusion coefficients of fully elongated fluids lie roughly along the same line as observed for quadrupolar fluids in the previous section. To analyze the effect of the dipole momentum, it is helpful to compare the bubble densities of Stockmayer

fluids in Fig. 5.4, where the influence is most visible, with the corresponding self-diffusion coefficient in Fig. 5.16. The self-diffusion coefficient shows a minimum for for Stockmayer fluids with $\mu^{*2} \approx 6$ at all three temperatures. The bubble densities of Stockmayer fluids also show a peculiar behavior: maxima at $T_R = 0.9$ and 1, and a point of inflexion at $T_R = 0.6$. As the self-diffusion coefficient of of non-polar fluids decreases with increasing density, it can be concluded that the isolated effect of the dipole is to increase the self-diffusion coefficient. Note that only for full elongated fluids the dipolar momentum does not affect significantly.

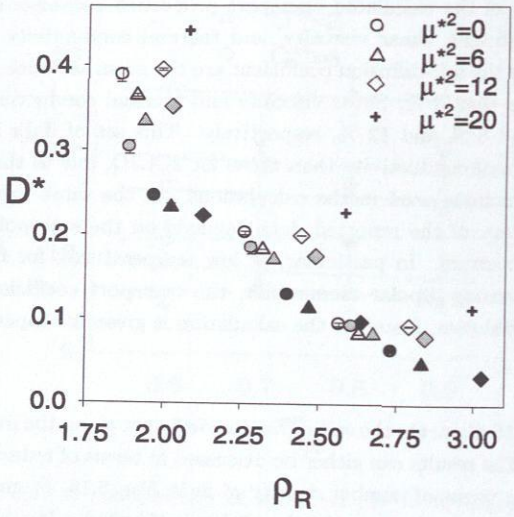

Figure 5.15: Self-diffusion coefficient of spherical ($L^* = 0$, empty symbols), elongated ($L^* = 0.505$, grey symbols), and strongly elongated ($L^* = 1$, full symbols) 2CLJD fluids over reduced density along bubble lines. Reduced temperatures vary from $T_R = 0.6$ to 0.9. Lines are guides for the eye.

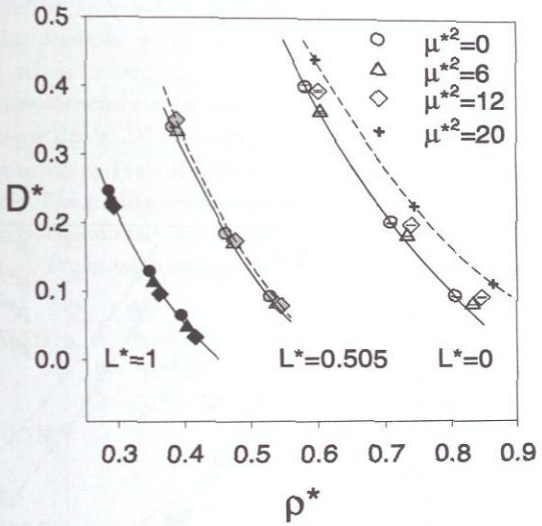

Figure 5.16: Self-diffusion coefficient of spherical ($L^* = 0$, empty symbols), elongated ($L^* = 0.505$, grey symbols), and strongly elongated ($L^* = 1.0$, full symbols) 2CLJD fluids over number density along bubble lines. Reduced temperatures vary from $T_R = 0.6$ to 0.9. Lines are guides for the eye.

Fig. 5.17 shows the dependence of D^* on number density in the homogeneous liquid region at constant reduced temperature of $T_R = 0.9$. Note that the density range is the same as in Fig. 5.16. Along this isotherm D^* decreases slightly hyperbolic with increasing density, resembling the behavior of D^* along bubble lines for a given elongation. Comparing D^* along bubble lines with isothermal data for the same density variation, it is concluded that density is the dominant variable, being responsible for about 80 % of the variation in D^*.

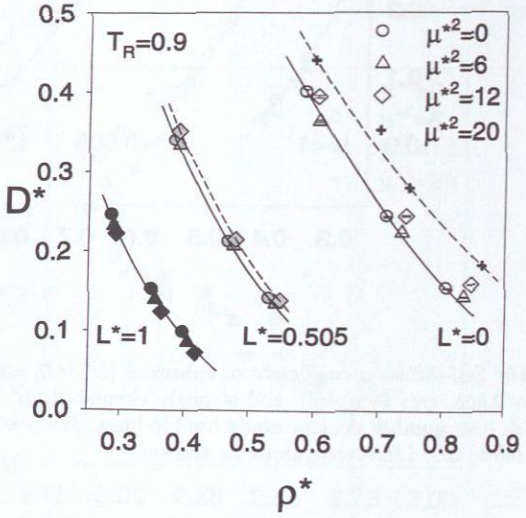

Figure 5.17: Self-diffusion coefficient of spherical ($L^* = 0$, empty symbols), elongated ($L^* = 0.505$, grey symbols), and strongly elongated ($L^* = 1$, full symbols) 2CLJD fluids over number density in homogeneous states at $T_R = 0.9$. Lines are guides for the eye.

Fig. 5.18 shows the dependence of the self-diffusion coefficient on reduced temperature for a subset of six selected fluids at different isochors. These isochors correspond to bubble densities at the reduced temperature $T_R = 0.6$, cf. Fig. 5.3, which have similar values in terms ρ_R. It can be seen that the self-diffusion coefficient decreases monotonously with increasing dipole momentum for elongated, whereas for Stockmayer fluids, D^* again exhibits a minimum at intermediate dipole momenta. Along an isochore, the self-diffusion coefficient increases linearly with increasing temperature. The gradients with respect to reduced temperature are almost constant for a given elongation but less pronounced for more elongated fluids. Such a linear dependence of D^* on temperature was also found for quadrupolar fluids.

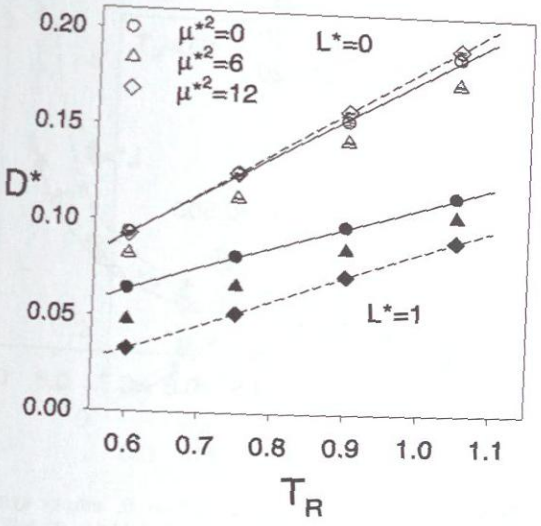

Figure 5.18: Self-diffusion coefficient of spherical ($L^* = 0$, empty symbols) and strongly elongated ($L^* = 1.0$, full symbols) 2CLJD fluids over reduced temperature in homogeneous liquid along different isochors. ○: $\rho^* = 0.8062$, △: $\rho^* = 0.8327$, ◇: $\rho^* = 0.8456$. Lines are guides for the eye.

Shear viscosity

Fig. 5.19 illustrates the shear viscosity along bubble lines for the ten selected fluids. In contrast to quadrupolar fluids, shear viscosity results for fluids with a given elongation, but different dipolar momentum, are not along a single line. At constant T_R, shear viscosity increases considerably with increasing dipole momentum. In accordance to quadrupolar fluids, more elongated molecules have generally a lower shear viscosity along the bubble line. The extremely high values of shear viscosity found for high dipole momenta ($\mu^{*2} = 20$) at low temperatures are remarkable.

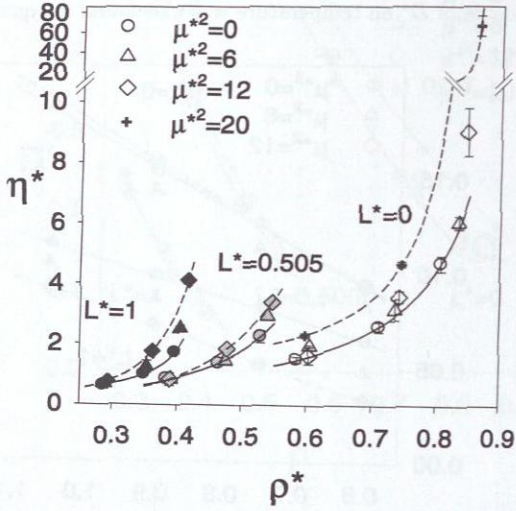

Figure 5.19: Shear viscosity of spherical ($L^* = 0$, empty symbols), elongated ($L^* = 0.505$, grey symbols), and strongly elongated ($L^* = 1$, full symbols) 2CLJD fluids over number density along bubble lines. Reduced temperatures vary from $T_R = 0.6$ to 0.9. Lines are guides for the eye.

Fig. 5.20 illustrates the isolated effect of density on shear viscosity for the same ten selected fluids in the homogeneous liquid region at $T_R = 0.9$. Comparing the variation of η^* along bubble lines and along isotherms in the same way as for D^*, it is found that the density is responsible for about 80 % of the increase of η^* along the bubble line. Exceptions are the shear viscosities of strongly dipolar Stockmayer fluids with $\mu^{*2} = 16$ and 20. These points are very sensitive to temperature changes, where the contribution of density is only about 10 % for $\mu^{*2} = 20$. Furthermore, comparing two points with similar density and the same dipolar momentum along curves describing different elongation, cf. curve $L^* = 0.505$ and $L^* = 1$ in Fig. 5.20, it can be discerned that η^* increases with increasing elongation.

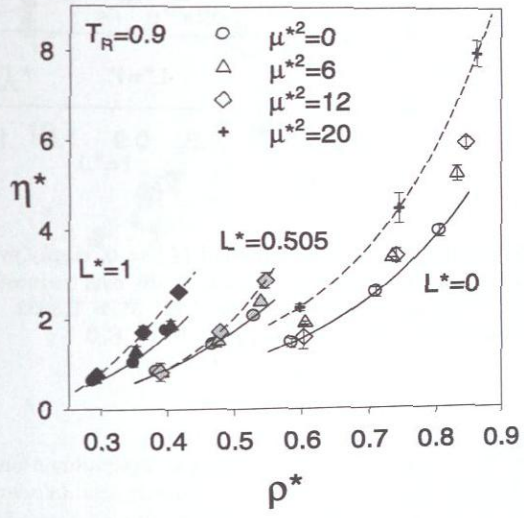

Figure 5.20: Shear viscosity of spherical ($L^* = 0$, empty symbols), elongated ($L^* = 0.505$, grey symbols), and strongly elongated ($L^* = 1$, full symbols) 2CLJD fluids over number density in homogeneous liquid at $T_R = 0.9$. Lines are guides for the eye.

Fig. 5.21 shows the dependence of shear viscosity on reduced temperature for a subset of six fluids along different isochores, with similar values in terms of T_R. As expected, the shear viscosity decreases with increasing temperature. Non-polar fluids show little temperature dependence. On the other hand, strongly dipolar fluids, with an about two-fold higher shear viscosity than non-polar fluids in the

cold liquid, are more sensitive to temperature exhibiting larger slopes.

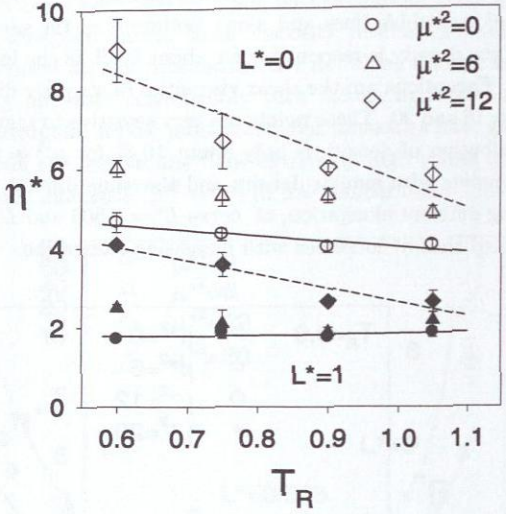

Figure 5.21: Shear viscosity of spherical ($L^* = 0$, empty symbols) and strongly elongated ($L^* = 1.0$, full symbols) 2CLJD fluids over reduced temperature in homogeneous liquid along different isochors. ○: $\rho^* = 0.8062$, △: $\rho^* = 0.8327$, ◇: $\rho^* = 0.8456$. Lines are guides for the eye.

Thermal conductivity

Fig. 5.22 illustrates the thermal conductivity along bubble lines. The thermal conductivity increases with increasing density. In contrast to quadrupolar fluids, the data for a constant elongation do not lie along a single line here. It can best be seen for Stockmayer fluids that λ vary depending on the dipolar momentum, between a lower and upper limit. The region between these limits seems to become narrower as the elongation increases, cf. curves for $L^* = 0.505$ and $L^* = 1$ in Fig. 5.22.

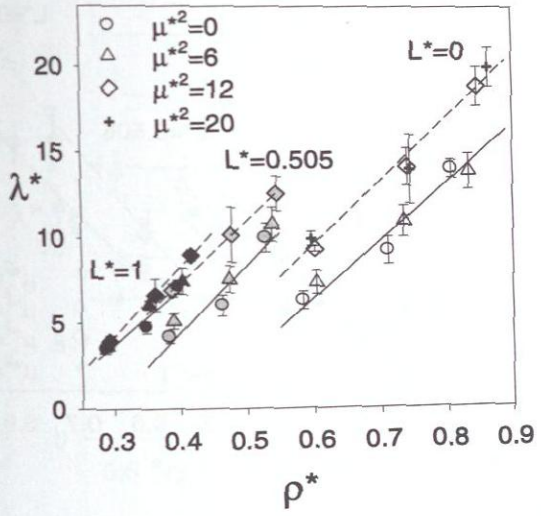

Figure 5.22: Thermal conductivity of spherical ($L^* = 0$, empty symbols), elongated ($L^* = 0.505$, grey symbols), and strongly elongated ($L^* = 1.0$, full symbols) 2CLJD fluids over number of density along bubble lines. Reduced temperatures vary from $T_R = 0.6$ to 0.9. Lines are guides for the eye.

Fig. 5.23 shows the density dependence of the same ten fluids in the homogeneous liquid at $T_R = 0.9$. As can be seen, the curves resemble those along bubble lines, cf. Fig. 5.22, demonstrating the dominant density effect. A closer look to two points with similar density along curves describing the same elongation but different dipolar momentum, reveals that the points with lower and higher dipolar momenta give the lower and higher values for λ^*, respectively. Similar results were found for quadrupolar fluids in the previous section.

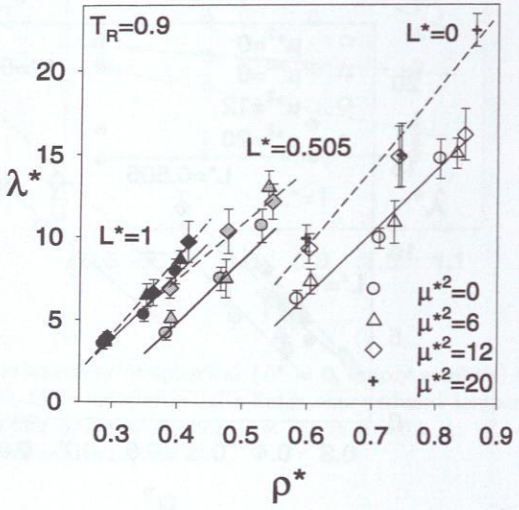

Figure 5.23: Thermal conductivity of spherical ($L^* = 0$, empty symbols), elongated ($L^* = 0.505$, grey symbols), and strongly elongated ($L^* = 1.0$, full symbols) 2CLJD fluids over number density at $T_R = 0.9$. Lines are guides for the eye.

Fig. 5.24 shows weak dependence of λ^* through isochoric data for a subset of six fluids. Taking the statistical uncertainty and the scatter into account, hardly any trend can be discerned. For a constant elongation, however, an increment in the thermal conductivity with increasing dipolar momentum can be observed, which is in agreement with the observation in the previous figures.

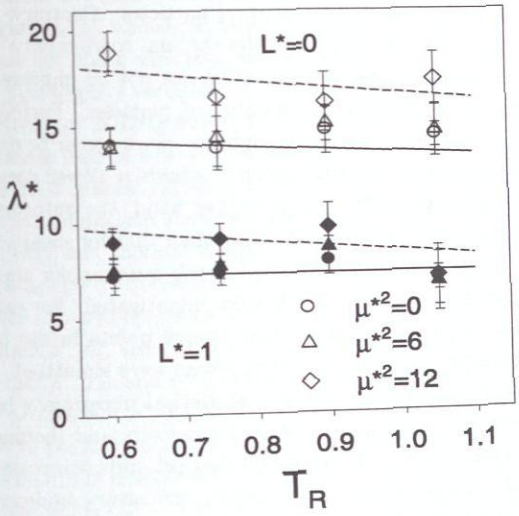

Figure 5.24: Thermal conductivity of spherical ($L^* = 0$, empty symbols) and strongly elongated ($L^* = 1.0$, full symbols) 2CLJD fluids over reduced temperature in the homogeneous liquid along different isochors. ○: $\rho^* = 0.8062$, △: $\rho^* = 0.8327$, ◇: $\rho^* = 0.8456$. Lines are guides for the eye. Lines are guides for the eye.

5.4 Conclusion

In this chapter a systematic study of the influence of polarity and anisotropy on self-diffusion coefficient, shear viscosity, and thermal conductivity was carried out. In addition, a comprehensive data set, which shows the isolated effect of quadrupole, dipole, and anisotropy and also the combined effect of these on self-diffusion, shear viscosity, and thermal conductivity, was generated. The statistical uncertainty of the reported data varies with the transport property. The Self-diffusion coefficient is the most accurate, principally because it is a particle property, for which statistics is improved by increasing the number of particles. Contrary, larger uncertainties are found for the shear viscosity and the thermal conductivity. Principally because the statistics of these transport properties can not be improved in the same from as self-diffusion by increasing the number of particles. Furthermore, at low temperatures, for strongly elongated or strongly quadrupolar or dipolar molecules the autocorrelation function of shear viscosity shows a slower decay, as reported previously [2, 67, 147, 148, 229]. On the other hand, the autocorrelation function of thermal conductivity shows a faster decay than that for shear viscosity but comparable scatter. These characteristics are in both quadrupolar and dipolar fluids.

For 2CLJQ fluids 30 model fluids were investigated. For each model fluid four points along the bubble line plus other twelve points in the homogeneous liquid sate were considered, in total 480 state points were simulated. Self-diffusion coefficients were predicted with an overall statistical uncertainty up to 3 %, whereas the overall statistical uncertainty for shear viscosity and thermal conductivity was 8 % and 12 %, respectively. It was found that self-diffusion coefficient, shear viscosity and thermal conductivity depend almost exclusively on density; elongation and quadrupolar momentum do not affect the behavior significantly.

Self-diffusion coefficient: It decreases with increasing ρ^* at constant L^* and Q^{*2} along the bubble line. In homogeneous liquid states, it increases linearly with increasing T_R at constant ρ^*, L^*, and Q^{*2}. With respect to the molecular parameters, it decreases with increasing L^* at constant ρ^*, T_R, and Q^{*2}, and with increasing Q^{*2} at constant ρ^*, T_R, and L^*.

Shear viscosity: It increases with increasing ρ^* at constant L^* and Q^{*2} along the bubble line. In homogeneous liquid states, it decreases with increasing T_R at constant ρ^*, L^*, and Q^{*2}. With respect to the molecular parameters, it increases with increasing L^* at constant ρ^*, T_R, and Q^{*2}, and with increasing Q^{*2} at constant ρ^*, T_R, and L^*.

Thermal conductivity: It behaves similar to shear viscosity. It increases with increasing ρ^* at constant L^* and Q^{*2} along the bubble line. The dependence on

T_R in homogeneous liquid states at constant ρ^*, L^*, and Q^{*2} is very weak and not significant with respect to the statistical uncertainty of the simulation data. Regarding L^* and Q^{*2}, it increases with increasing L^* at constant ρ^*, T_R, and Q^{*2}. The effect of Q^{*2} at constant ρ^*, T_R, and L^* is more difficult to discern because of the statistical uncertainty of the simulations, but it seems to increase with increasing Q^{*2}.

For 2CLJD fluids 38 model fluids were investigated. For each model fluid three points along the bubble line plus other nine points in the homogeneous liquid region were considered, in total 456 state points were simulated. Self-diffusion coefficients were predicted with an overall statistical uncertainty up to 3 %, whereas the overall statistical uncertainty for shear viscosity and thermal conductivity was 8 % and 10 %, respectively. This slightly variation of the uncertainties respect to the results for thermal conductivity of 2CLJQ fluids, is consequence of the larger number of autocorrelation functions used in the calculation. In the same form as for the 2CLJQ fluids, the density is the dominant variable. However, different from the quadrupolar interaction, the dipolar interaction shows a significant effect in the behavior of self-diffusion, shear viscosity, and thermal conductivity.

Self-diffusion coefficient: It decreases with increasing ρ^* at constant L^* and μ^* along the bubble line. In homogeneous liquid states, it increases linearly with increasing T_R at constant ρ^*, L^*, and μ^{*2}. As expected, self-diffusion decreases with increasing L^* at constant ρ^*, T_R, and μ^{*2}. Remarkably, self-diffusion *seems to increase* with increasing μ^{*2} at constant ρ^*, T_R, and L^* at least for dipolar momenta $\mu^{*2} > 6$. The elongation affects the influence of the dipolar momentum on self-diffusion, the more elongated the fluid, the smaller is the effect of μ^{*2} on self-diffusion. In particular, for very elongated fluids ($L^* = 0.8$), no influence of the dipolar momentum was observed.

Shear viscosity: It increases with increasing ρ^* at constant L^* and μ^{*2} along the bubble line. In homogeneous liquid states, it decreases with increasing T_R at constant ρ^*, L^*, and μ^{*2}. In the same way as for quadrupolar fluids, shear viscosity increases with increasing L^* at constant ρ^*, T_R, and μ^{*2}, and with increasing μ^{*2} at constant ρ^*, T_R, and L^*. Elongation affects the influence of the dipolar momentum in the same way as for self-diffusion. However, in contrast to self-diffusion, even for very elongated fluids the effect of dipolar momentum is significant.

Thermal conductivity: It increases with increasing ρ^* at constant L^* and μ^{*2} along the bubble line. Like for quadrupolar fluids, the dependence on T_R in homogeneous liquid states at constant ρ^*, L^*, and μ^{*2} is not significant considering the statistical uncertainty of the simulation data. Furthermore, it increases with increasing L^* at constant ρ^*, T_R, and Q^{*2} as well as with increasing μ^{*2} at constant

ρ^*, T_R, and L^*.

The following tables resume the observed tendencies for self-diffusion coefficient, shear viscosity, and thermal conductivity of 2CLJQ and 2CLJD fluids.

Table 5.1: Tendencies of the transport coefficients respect to ρ^*, T_R, L^*, and Q^{*2} for quadrupolar fluids.The meaning of the arrows is as follow. ↑: the transport property increases upon increasing the variable at the top of the column, ↓: the transport property decreases with the variable at the top of the column.

2CLJQ	ρ^* along bubble lines	T_R homogeneous liquid	L^* homogeneous liquid	Q^{*2} homogeneous liquid
D^* at constant	↓ L^*, Q^{*2}	↑ ρ^*, L^*, Q^{*2}	↓ ρ^*, T_R, Q^{*2}	↓ ρ^*, T_R, L^*
η^* at constant	↑ L^*, Q^{*2}	↓ ρ^*, L^*, Q^{*2}	↑ ρ^*, T_R, Q^{*2}	↑ ρ^*, T_R, L^*
λ^* at constant	↑ L^*, Q^{*2}	weak ρ^*, L^*, Q^{*2}	↑ ρ^*, T_R, Q^{*2}	↑ ρ^*, T_R, L^*

Table 5.2: Tendencies of the transport coefficients respect to ρ^*, T_R, L^*, and μ^{*2} for dipolar fluids. The meaning of the arrows is the same as in the previous table for 2CLJQ fluids.

2CLJD	ρ^* along bubble lines	T_R homogeneous liquid	L^* homogeneous liquid	μ^{*2} homogeneous liquid
D^* at constant	↓ L^*, μ^{*2}	↑ ρ^*, L^*, μ^{*2}	↓ ρ^*, T_R, μ^{*2}	↑ ρ^*, T_R, L^* and $\mu^{*2}>6$
η^* at constant	↑ L^*, μ^{*2}	↓ ρ^*, L^*, μ^{*2}	↑ ρ^*, T_R, μ^{*2}	↑ ρ^*, T_R, L^*
λ^* at constant	↑ L^*, μ^{*2}	weak ρ^*, L^*, μ^{*2}	↑ ρ^*, T_R, μ^{*2}	↑ ρ^*, T_R, L^*

Appendix

A Simulation details

A.1 Self-diffusion and binary Maxwell-Stefan diffusion coefficients

The molecular simulations were performed in a cubic box of volume V containing standard $N = 500$ molecules modeled by the LJ potential or 2CLJQ potential, respectively. The cut-off radius was set to $r_c = 5\sigma$; standard techniques for periodic boundary conditions and long-range corrections were used [5]. For the calculation of the 2CLJ long range corrections, orientational averaging was applied with equally weighted relative orientations as proposed by Lustig [156]. The assumption of no preferential relative orientations beyond the cut-off sphere implies for the quadrupolar interactions that long range corrections are not needed since they vanish. The simulations were started with the molecules in a face-center-cubic lattice with random velocities, the total momentum of the system was set to zero. Two sort of molecular dynamic ensemble were used: for simulation with the spherical LJ potential NVE ensemble was used. In this case the Newton's equations of motion were solved with a velocity-Verlet algorithm [5]. Simulations for 2CLJQ fluids were carried out in the NVT ensemble, here modified Newton's equations of motion were solved with the Gear predictor-corrector integration scheme of fifth order [92]. In both cases the time step for these algorithms was set to $\Delta t\sqrt{\epsilon_1/m_1}/\sigma_1 = 0.001$ for liquid and 0.01 for Gas state points.

The diffusion coefficients were calculated in a NVE or NVT ensemble, using Eqs. (2.7) and (2.8). The relative fluctuation in the total energy in the NVE ensemble was less than 10^{-3} for the longest run, which yields a temperature drift of less than 0.5 K. In the NVT ensemble temperature fluctuations are zero in average. The thermosetting was accomplished using the Nosé-Hoover thermostat [77, 203] with a thermal inertial parameter $Q_s/(m\sigma^2) = 10$. It must be pointed out that both NVE and NVT simulations were performed, and the obtained diffusion coefficients agreed in all cases within their uncertainties. It was concluded that the Nosé-Hoover thermostat does not influence the values of the diffusion coefficients.

Both kind of simulations are initiated in a NVT ensemble until equilibrium at the desired density and temperature is reached. 100 000 time steps were used for that equilibration. Once the equilibrium is reached, the thermostat is turned off,

and then the NVE ensemble is invoked. Otherwise, the simulations continues in the NVT ensemble were the transport properties are calculated. The experimental data which was used for comparison to our simulations is often reported at given pressure and temperature. In these cases, a prior isobaric-isothermal NpT simulation [6] was performed, from which the corresponding densities for the NVE or NVT ensemble were taken. The statistical uncertainty of the diffusion coefficients was estimated with the standard block average technique [77].

The self diffusion coefficient is a property related to one molecule. It is possible to obtain very good statistics with a few independent velocity autocorrelation functions (VACF). The self diffusion coefficients were calculated by averaging over 200 independent VACF each with 500 molecules, i.e. a total of 10^5 VACF. For gas densities, the VACF decays very slowly and therefore long simulation runs were necessary in order to achieve the VACF decay and hence independent time-origins. Here, a compromise between simulation time and time-origin independence had to be made. In order to keep the simulation time low, and following the work of Schoen and Hoheisel [228], the separation between time origins was chosen at least as long as the VACF needs to decay to $1/e$ of its normalized value. The choice of this separation time and the production phase depended upon the temperature and density conditions. In theory, as Eq. (2.7) shows, the value of the diffusion coefficient is determined by an infinite time integral. In fact, however, the integral is evaluated based on the length of the simulation. The integration must be stopped at some finite time, ensuring that the contribution of the long-time tail [2] is small compared to the desired statistical uncertainty of the diffusion coefficient. Figure A.1.1 shows the behavior of the VACF and its integral given by Eq. (2.7) for two selected gas state points of argon. As can be seen, for the higher density state point, the VACF has decayed after 500 ps to less than 1 % of its normalized value. Later it oscillates around zero. The same can be seen after 1 500 ps at the lower density state point. It was assumed here that the VACF has fully decayed when these oscillations reached a threshold below 0.5 % of their normalized value. Furthermore, a graphical inspection of the VACF integral was made, in order to verify a sufficient integration time.

An important time scale to calculate the VACF is the time that a sound wave takes to cross the simulation box. VACF calculated for times higher than that may show a systematic error [95, 109]. That criterion was verified using the experimental speed of sound taken from [31]. For the simulations of gases, the VACF decay time was found to be higher than that time. To check whether this to leads to a systematic error in the present simulations, the system size was varied. For the lowest density state point of argon, where the above mentioned problem would be expected to

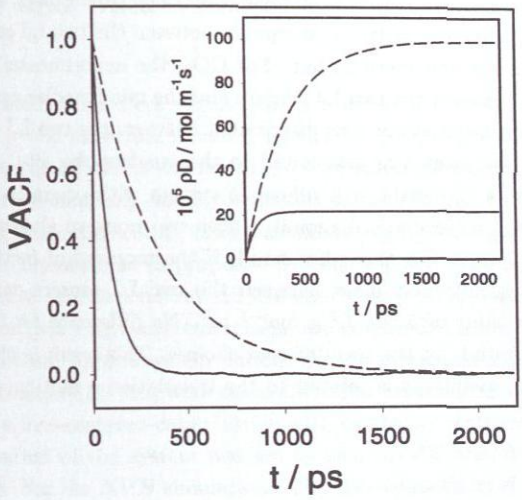

Figure A.1.1: Large plot: Velocity autocorrelation functions. Small plot: Integral following Eq. (2.7). Both plots are shown for selected state points of argon: —— $T = 77.7$ K and $\rho = 163.26$ mol m^{-3}; - - - - $T = 353.2$ K and $\rho = 34.49$ mol m^{-3}.

be most severe, simulations with a constant number of time origins and increasing system sizes were carried out. System sizes of $N = 864$, 2 048, 4 000, and 6 912 molecules were investigated. All results were found to agree within the statistical uncertainty, and no size dependence could be observed. It is therefore concluded that no systematic error due to system size in gas phase simulations is present.

For the calculation of the binary MS diffusion coefficients, 12 000 independent time origins were averaged, here a compromise between accuracy and simulation time was made. The time origins were taken every 100th time steps, and the correlation function was calculated over 1 000 to 1 500 time steps. This requires simulations of about $1 \cdot 10^5$ to $4 \cdot 10^5$ time steps for the self-diffusion coefficients and $12 \cdot 10^5$ for MS diffusion coefficients. The binary MS diffusion coefficients were calculated for mole fractions between 0.1 and 0.9. To obtain the binary MS diffusion coefficients at infinite dilution, a polynomial function was fitted to the simulation results between mole fractions 0.1 and 0.9 and then extrapolated to zero and one, respectively. The relative error was estimated as being the same as for the binary MS diffusion coefficients at 0.1 and 0.9, respectively.

Other important issue for molecular fluids, is the influence of the moments of

inertia of the molecules on the self-diffusion coefficient. In all cases, the experimental molecular mass [202] was distributed equally between the two LJ centers. However, for CO_2 this matter was investigated. For CO_2, the experimental molecular mass was distributed between the two LJ centers and the quadrupolar center, so that the mass of the two oxygen atoms was distributed between the two LJ centers, and the mass of the carbon atom was associated to the quadrupolar site. In this case the tensor of moments of inertia in a reference system with origin in the geometrical center of the CO_2 molecule is diagonal, whose two nonzero elements are given by 4.000 L^2 g mol^{-1} m^2. On the other hand, if the moment of inertia is calculated sharing the total molecular mass between the two LJ centers only, the diagonal elements have a value of 5.501 L^2 g mol^{-1} m^2. No difference for the self-diffusion coefficients was found, for the two different choices. This result is plausible, because the self-diffusion coefficient is related to the translational motion of the molecular center of mass.

A.2 Shear and bulk viscosity, and thermal conductivity

The molecular simulations were performed in a cubic box of volume V containing standard $N = 500$ molecules modeled by the LJ potential or 2CLJQ potential, respectively. The cut-off radius was set to $r_c = 5\sigma$; standard techniques for periodic boundary conditions and long-range corrections were used [5]. For the calculation of the 2CLJ long range corrections, orientational averaging was applied with equally weighted relative orientations as proposed by Lustig [156]. The assumption of no preferential relative orientations beyond the cut-off sphere implies for the quadrupolar interactions that long range corrections are not needed since they vanish. For 2CLJD fluids instead, long-range corrections due to dipolar interactions using the reaction field technique [11, 199] were calculated. The simulations were started with the particles in a face-centered-cubic lattice with randomly assigned velocities, and the total momentum of the system was set to zero. NVE and NVT simulations were carried out. For the NVE simulations, Newton's equations of motion were integrated, for NVT simulations instead, modified Newton's equations of motion were integrated. In both cases, a Gear predictor-corrector of fifth order [92] method was used. The time step for this algorithm was set to $\Delta t\sqrt{\epsilon_1/m_1}/\sigma_1 = 0.001$. Transport coefficients for quadrupolar fluids were calculated in NVE, the temperature drift was less than 3 % in all cases. On the contrary, the reaction field method applied for the long range corrections of dipolar fluids does not conserve the energy of the system, therefore transport properties of dipolar fluids were calculated in the NVT ensemble, with the Nosé-Hoover thermostat [77, 203] with a thermal inertial parameter $Q_s/(m\sigma^2) = 10$. In both cases equations (2.17), (2.19), (2.21) and (2.23) were used. Both kind of simulations were initiated in a NVT ensemble until equilibrium at the desired density and temperature was reached. Between 100 000 and 200 000 time steps were used for the equilibration depending on the state point. Once the equilibrium is reached, the thermostat was turned off and then the NVE ensemble invoked, otherwise the thermostating is held until the simulation is completed. The length of the production period depended on density and temperature of the state point. In particular for the systematic study of transport properties of 2CLJQ and 2CLJD fluids, a total of 12 000 and 15 000 independent autocorrelation functions were respectively used. They were grouped in blocks of 3 000 for 2CLJQ and in blocks of 5 000 for the 2CLD fluids, from which the statistical uncertainty was calculated using a block average technique [77].

In theory as Eqs. (2.17), (2.19) and (2.21) show, the value of the transport coefficient are determined by an infinite time integral. In fact, however, the integral

is evaluated based on the length of the simulation. Therefore, the integration must be stopped at some finite time, ensuring that the contribution of the long-time tail [2] is small. Figure A.2.1 shows the behavior of the different autocorrelation functions and their integrals given by Eqs. (2.17), (2.19) and (2.21) for the most dense state points of argon for each transport property. As can be seen, all autocorrelation functions decay after 2 ps to less than 1 % of their normalized value. Later they oscillate around zero. To consider the effect of the long time tail, the calculation of the autocorrelations functions was extended to 5.4 ps for thermal conductivity and shear viscosity and to 6.5 ps for bulk viscosity. This was done because this autocorrelation function exhibits the largest fluctuation around zero attributable to long time correlation. The statistical uncertainty of the transport coefficients and thermodynamic properties were estimated using the Fincham's method [70]. For the calculation of the thermal conductivity of mixtures it was necessary to include the partial molar enthalpies. For that purpose, Widom's test particle insertion [238] was taken using 2 000 test particles after each time step, 100 000 time steps for reaching equilibrium and 300 000 for production.

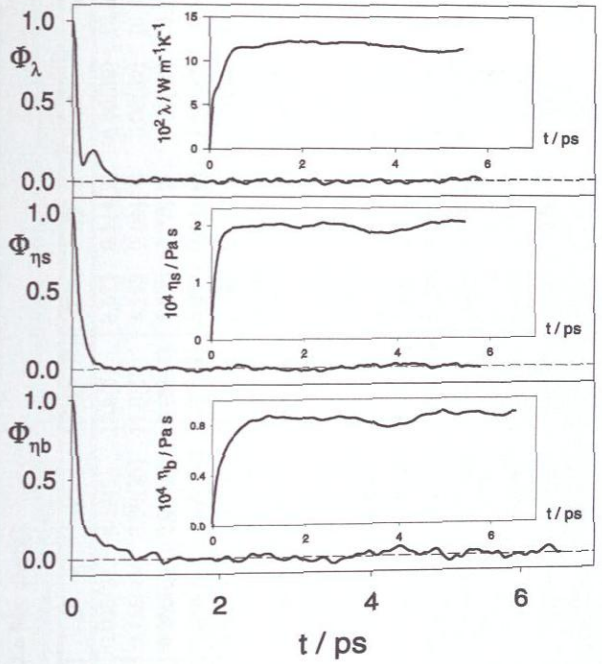

Figure A.2.1: Large plots: Autocorrelation functions. Small plots: Integrals following Eqs. (2.17), (2.19) and (2.21). All plots are shown for the most dense state points of argon for each transport property; top: thermal conductivity $T = 90$ K and $\rho = 34\,433$ mol m^{-3}, middle: shear viscosity $T = 150.7$ K and $\rho = 35\,046$ mol m^{-3}, bottom: bulk viscosity $T = 100$ K and $\rho = 32\,843$ mol m^{-3}.

B Numerical simulation results

B.1 Self-diffusion, shear viscosity, and thermal conductivity for 2CLJQ fluids

Tables B.1.1 to B.1.12 show the simulation results for the 2CLJQ fluids.

Table B.1.1: Transport coefficients of 2CLJQ fluids, for $L^* = 0$ and different quadrupole momentum Q^{*2}. The numbers in parentheses denote the uncertainty in the last digits.

$L^*=0$	T^*	ρ^*	D^*	η^*	λ^*	T^*	D^*	η^*	λ^*
$Q^{*2}=0$	3.156	0.8062	0.095(2)	4.83(9)	13.4(6)	3.671	0.114(2)	4.60(39)	12.5(17)
	3.681	0.7453	0.155(4)	3.00(35)	11.0(13)	4.193	0.184(3)	3.08(32)	10.0(12)
	4.255	0.6735	0.250(6)	2.00(24)	8.65(77)	4.696	0.278(2)	1.87(10)	9.30(11)
	4.674	0.5838	0.388(5)	1.52(16)	6.37(51)	5.243	0.431(6)	1.57(12)	6.59(77)
$Q^{*2}=1$	3.132	0.8201	0.080(1)	5.31(35)	11.7(12)	3.729	0.100(2)	5.31(26)	15.2(26)
	3.712	0.7575	0.143(2)	3.62(23)	11.2(12)	4.246	0.166(1)	3.17(33)	11.9(12)
	4.187	0.6851	0.228(4)	2.26(18)	9.8(12)	4.782	0.261(6)	2.38(13)	9.26(90)
	4.773	0.5934	0.368(2)	1.58(6)	6.44(78)	5.311	0.407(6)	1.51(5)	6.6(10)
$Q^{*2}=2$	3.398	0.8483	0.062(3)	7.67(46)	13.0(19)	3.914	0.080(1)	6.30(56)	14.96(55)
	3.925	0.7819	0.119(1)	4.45(34)	10.7(22)	4.474	0.143(3)	4.11(14)	12.81(91)
	4.538	0.7041	0.205(2)	2.64(25)	10.32(82)	5.048	0.236(2)	2.80(29)	9.48(99)
	4.946	0.6055	0.339(3)	1.79(16)	7.07(11)	5.580	0.381(2)	1.77(18)	7.30(86)
$Q^{*2}=3$	3.505	0.8796	0.047(1)	9.70(64)	15.4(25)	4.203	0.065(2)	8.41(73)	15.2(19)
	4.106	0.8099	0.099(2)	5.83(58)	12.4(13)	4.782	0.122(3)	5.24(36)	15.1(26)
	4.741	0.7292	0.179(1)	3.28(62)	10.4(19)	5.412	0.210(2)	3.40(17)	10.8(10)
	5.341	0.6272	0.310(4)	1.93(26)	7.9(12)	5.921	0.346(3)	2.02(22)	7.30(35)
$Q^{*2}=4$	3.841	0.9143	0.038(1)	14.02(86)	18.3(19)	4.467	0.050(1)	11.53(77)	15.9(19)
	4.476	0.8430	0.081(1)	6.87(64)	15.9(17)	5.161	0.102(1)	6.70(53)	14.8(22)
	5.164	0.7609	0.153(3)	3.85(21)	11.9(14)	5.744	0.179(2)	4.07(39)	11.9(19)
	5.742	0.6579	0.275(4)	2.54(27)	9.8(15)	6.401	0.313(2)	2.29(22)	8.7(13)

Table B.1.2: Transport coefficients of 2CLJQ fluids, for $L^* = 0$ and different quadrupole momentum Q^{*2}. The numbers in parentheses denote the uncertainty in the last digits.

$L^* = 0$	T^*	ρ^*	D^*	η^*	λ^*	T^*	D^*	η^*	λ^*
$Q^{*2} = 0$	4.201	0.8062	0.136(1)	4.52(31)	13.52(84)	4.711	0.155(4)	4.12(27)	12.60(82)
	4.746	0.7453	0.210(1)	3.18(16)	10.8(11)	5.248	0.233(3)	3.04(14)	11.91(98)
	5.191	0.6735	0.306(4)	1.96(12)	8.14(17)	5.755	0.339(6)	2.24(15)	9.01(90)
	5.718	0.5838	0.462(2)	1.55(10)	6.53(41)	6.279	0.502(11)	1.57(13)	6.96(47)
$Q^{*2} = 1$	4.272	0.8201	0.121(2)	4.37(29)	14.26(11)	4.784	0.141(1)	4.82(36)	11.55(16)
	4.786	0.7575	0.190(1)	3.27(9)	10.91(12)	5.314	0.215(3)	3.01(35)	10.9(12)
	5.359	0.6851	0.295(1)	2.20(20)	10.99(22)	5.859	0.321(3)	2.30(33)	9.52(17)
	5.775	0.5934	0.442(2)	1.57(15)	7.06(11)	6.373	0.479(3)	1.63(29)	7.65(41)
$Q^{*2} = 2$	4.455	0.8483	0.099(1)	6.13(57)	12.93(67)	5.011	0.118(2)	5.21(11)	15.5(14)
	5.025	0.7819	0.168(1)	4.00(36)	12.29(64)	5.568	0.189(2)	4.02(49)	12.2(23)
	5.530	0.7041	0.260(3)	2.63(6)	10.05(80)	6.141	0.295(4)	2.66(12)	9.0(15)
	6.102	0.6055	0.416(1)	1.60(8)	7.34(96)	6.683	0.455(1)	1.61(16)	7.9(11)
$Q^{*2} = 3$	4.771	0.8796	0.081(1)	7.70(51)	16.5(16)	5.345	0.098(1)	7.52(27)	13.8(14)
	5.374	0.8099	0.144(2)	4.43(34)	12.1(20)	5.986	0.167(1)	4.84(39)	15.2(14)
	6.000	0.7292	0.238(1)	3.14(22)	10.7(10)	6.563	0.263(5)	3.21(45)	12.3(18)
	6.556	0.6272	0.388(3)	1.88(11)	8.27(73)	7.152	0.423(5)	1.98(14)	8.46(85)
$Q^{*2} = 4$	5.106	0.9143	0.065(2)	9.47(38)	17.96(95)	5.749	0.081(2)	9.59(83)	17.8(27)
	5.753	0.8430	0.121(2)	5.76(10)	15.11(21)	6.410	0.143(2)	5.81(82)	14.1(12)
	6.338	0.7609	0.204(1)	4.12(10)	11.80(10)	7.027	0.234(4)	3.48(41)	12.4(31)
	6.978	0.6579	0.345(1)	2.16(20)	9.04(69)	7.700	0.384(7)	2.15(25)	9.12(20)

Table B.1.3: Transport coefficients of 2CLJQ fluids, for $L^* = 0.2$ and different quadrupole momentum Q^{*2}. The numbers in parentheses denote the uncertainty in the last digits.

$L^* = 0.2$	T^*	ρ^*	D^*	η^*	λ^*	T^*	D^*	η^*	λ^*
$Q^{*2} = 0$	2.589	0.7114	0.089(1)	3.64(16)	11.58(59)	3.029	0.106(1)	3.89(16)	12.23(80)
	3.015	0.6573	0.147(1)	2.63(10)	9.69(74)	3.483	0.169(1)	2.58(10)	10.32(19)
	3.441	0.5946	0.228(6)	1.74(11)	7.67(83)	3.863	0.251(3)	1.83(8)	7.60(57)
	3.874	0.5144	0.353(7)	1.27(10)	5.90(30)	4.299	0.381(5)	1.23(6)	5.95(55)
$Q^{*2} = 1$	2.625	0.7203	0.083(1)	4.19(21)	12.0(10)	3.075	0.101(1)	3.98(19)	14.08(94)
	3.070	0.6644	0.142(2)	2.86(23)	11.7(12)	3.528	0.163(1)	2.68(20)	11.82(91)
	3.496	0.5998	0.226(4)	1.89(10)	8.54(57)	3.937	0.247(2)	1.78(13)	8.70(81)
	3.941	0.5185	0.350(9)	1.19(10)	6.74(28)	4.408	0.381(3)	1.30(10)	6.51(61)
$Q^{*2} = 2$	2.722	0.7420	0.075(1)	4.78(36)	17.1(13)	3.210	0.093(2)	4.75(29)	17.9(10)
	3.195	0.6833	0.133(2)	2.97(12)	15.4(15)	3.642	0.152(2)	2.86(15)	13.9(18)
	3.659	0.6167	0.215(4)	2.12(14)	11.76(93)	4.095	0.237(4)	2.06(12)	10.89(92)
	4.072	0.5322	0.338(8)	1.34(10)	7.74(47)	4.511	0.367(3)	1.29(8)	7.46(60)
$Q^{*2} = 3$	2.877	0.7683	0.067(1)	5.48(21)	21.0(28)	3.333	0.082(1)	5.08(18)	22.4(16)
	3.393	0.7085	0.123(1)	3.67(10)	19.8(16)	3.876	0.143(2)	3.48(17)	17.6(10)
	3.856	0.6397	0.203(5)	2.40(10)	15.6(18)	4.314	0.224(3)	2.34(14)	14.90(90)
	4.318	0.5535	0.326(6)	1.53(16)	9.5(10)	4.751	0.351(3)	1.51(10)	10.45(95)
$Q^{*2} = 4$	3.054	0.7939	0.026(3)	11.21(42)	23.2(30)	3.560	0.075(1)	6.23(10)	24.4(14)
	3.642	0.7311	0.117(2)	4.06(14)	22.5(24)	4.091	0.135(2)	3.91(26)	22.7(20)
	4.103	0.6596	0.196(2)	2.44(10)	18.4(21)	4.604	0.219(3)	2.45(13)	17.5(21)
	4.600	0.5686	0.324(9)	1.71(10)	12.0(21)	5.099	0.352(1)	1.64(10)	12.38(77)

Table B.1.4: Transport coefficients of 2CLJQ fluids, for $L^* = 0.2$ and different quadrupole momentum Q^{*2}. The numbers in parentheses denote the uncertainty in the last digits.

$L^* = 0.2$	T^*	ρ^*	D^*	η^*	λ^*	T^*	D^*	η^*	λ^*
$Q^{*2} = 0$	3.421	0.7114	0.124(3)	3.81(17)	11.87(92)	3.895	0.144(3)	3.38(21)	11.37(89)
	3.882	0.6573	0.192(1)	2.74(13)	10.06(62)	4.311	0.218(2)	2.46(15)	9.9(11)
	4.299	0.5946	0.284(3)	1.76(10)	7.60(49)	4.737	0.316(3)	1.69(10)	7.77(47)
	4.756	0.5144	0.430(3)	1.39(10)	5.80(30)	5.168	0.469(1)	1.29(12)	6.60(16)
$Q^{*2} = 1$	3.515	0.7203	0.120(2)	3.73(17)	12.9(20)	3.962	0.140(1)	3.65(10)	13.25(99)
	3.943	0.6644	0.187(2)	2.56(9)	12.0(16)	4.392	0.208(4)	2.68(13)	10.4(10)
	4.340	0.5998	0.276(4)	1.85(6)	8.91(80)	4.807	0.310(5)	1.87(10)	8.24(73)
	4.854	0.5185	0.426(2)	1.33(10)	6.40(60)	5.249	0.464(6)	1.32(10)	6.69(50)
$Q^{*2} = 2$	3.629	0.7420	0.108(2)	4.11(21)	16.2(16)	4.131	0.128(1)	4.01(17)	18.5(11)
	4.142	0.6833	0.178(1)	3.06(10)	13.26(80)	4.597	0.199(2)	3.07(15)	13.71(70)
	4.554	0.6167	0.268(2)	2.08(13)	11.24(84)	5.034	0.300(2)	2.00(19)	10.16(75)
	4.975	0.5322	0.412(5)	1.26(10)	7.00(60)	5.452	0.454(1)	1.37(11)	8.08(80)
$Q^{*2} = 3$	3.819	0.7683	0.098(1)	5.49(26)	21.7(28)	4.298	0.115(1)	5.64(26)	21.4(55)
	4.296	0.7085	0.162(1)	3.16(11)	14.8(24)	4.820	0.184(2)	3.18(21)	16.4(24)
	4.846	0.6397	0.256(3)	2.43(16)	14.5(22)	5.308	0.284(1)	2.20(10)	13.3(12)
	5.229	0.5535	0.392(8)	1.53(17)	8.68(70)	5.764	0.438(6)	1.58(23)	9.3(12)
$Q^{*2} = 4$	4.092	0.7939	0.092(1)	5.72(15)	25.9(49)	4.611	0.108(2)	5.75(12)	25.6(55)
	4.613	0.7311	0.156(2)	3.75(29)	22.2(30)	5.119	0.176(2)	3.49(10)	20.02(80)
	5.077	0.6596	0.244(1)	2.55(24)	16.0(11)	5.605	0.272(6)	2.18(22)	16.43(89)
	5.620	0.5686	0.393(8)	1.65(10)	11.1(11)	6.129	0.435(8)	1.76(22)	9.8(21)

Table B.1.5: Transport coefficients of 2CLJQ fluids, for $L^* = 0.4$ and different quadrupole momentum Q^{*2}. The numbers in parentheses denote the uncertainty in the last digits.

$L^* = 0.4$	T^*	ρ^*	D^*	η^*	λ^*	T^*	D^*	η^*	λ^*
$Q^{*2} = 0$	1.893	0.5808	0.094(2)	2.51(20)	9.36(45)	2.208	0.110(1)	2.37(14)	10.35(84)
	2.232	0.5365	0.147(1)	1.82(10)	8.90(36)	2.519	0.163(1)	1.81(11)	8.13(50)
	2.536	0.4853	0.219(5)	1.32(10)	6.67(57)	2.841	0.238(3)	1.32(10)	6.76(50)
	2.858	0.4185	0.326(3)	0.89(5)	4.92(47)	3.150	0.354(2)	0.92(8)	4.98(30)
$Q^{*2} = 1$	1.925	0.5879	0.084(1)	2.82(17)	10.12(60)	2.249	0.100(1)	2.64(13)	10.75(71)
	2.239	0.5426	0.134(1)	2.03(10)	8.97(40)	2.559	0.155(3)	2.00(15)	7.99(94)
	2.573	0.4913	0.206(1)	1.35(8)	7.39(55)	2.875	0.231(5)	1.38(10)	7.32(60)
	2.869	0.4252	0.311(2)	0.92(8)	5.24(84)	3.199	0.342(3)	0.93(6)	5.32(71)
$Q^{*2} = 2$	1.999	0.6025	0.072(1)	3.36(11)	11.11(80)	2.317	0.087(1)	3.10(15)	11.41(87)
	2.318	0.5555	0.121(1)	2.23(10)	9.58(40)	2.651	0.140(1)	2.10(13)	10.06(80)
	2.663	0.5008	0.194(2)	1.53(10)	7.60(55)	2.975	0.216(1)	1.45(8)	6.7(10)
	2.987	0.4310	0.304(4)	0.97(8)	6.02(40)	3.316	0.334(3)	0.94(10)	5.23(50)
$Q^{*2} = 3$	2.096	0.6209	0.061(1)	3.98(14)	14.9(11)	2.431	0.074(1)	3.84(14)	13.35(80)
	2.447	0.5717	0.109(1)	2.64(10)	10.52(90)	2.781	0.126(1)	2.47(10)	10.2(13)
	2.794	0.5154	0.180(1)	1.71(10)	8.52(60)	3.100	0.199(2)	1.67(10)	7.95(60)
	3.134	0.4428	0.290(5)	1.07(8)	6.37(60)	3.483	0.321(2)	1.08(8)	6.32(50)
$Q^{*2} = 4$	2.213	0.6396	0.051(6)	5.83(80)	14.04(71)	2.579	0.064(1)	4.72(44)	15.6(20)
	2.599	0.5884	0.098(2)	2.95(20)	13.3(12)	2.941	0.115(2)	3.10(20)	12.7(12)
	2.972	0.5307	0.168(1)	1.90(13)	10.51(17)	3.298	0.188(3)	1.86(11)	10.0(17)
	3.350	0.4554	0.281(3)	1.21(10)	7.61(41)	3.686	0.309(3)	1.15(10)	7.41(50)

Table B.1.6: Transport coefficients of 2CLJQ fluids, for $L^* = 0.4$ and different quadrupole momentum Q^{*2}. The numbers in parentheses denote the uncertainty in the last digits.

$L^* = 0.4$	T^*	ρ^*	D^*	η^*	λ^*	T^*	D^*	η^*	λ^*
$Q^{*2} = 0$	2.533	0.5808	0.126(2)	2.41(14)	10.79(61)	2.863	0.144(2)	2.56(15)	10.3(15)
	2.849	0.5365	0.186(1)	1.86(10)	8.11(74)	3.134	0.204(3)	1.90(11)	8.22(53)
	3.157	0.4853	0.269(3)	1.36(10)	6.15(60)	3.446	0.290(8)	1.33(10)	6.70(50)
	3.513	0.4185	0.404(4)	0.90(6)	5.04(20)	3.809	0.434(16)	0.97(6)	5.15(70)
$Q^{*2} = 1$	2.556	0.5879	0.116(2)	2.60(25)	11.3(11)	2.881	0.133(2)	2.77(23)	11.43(72)
	2.876	0.5426	0.175(1)	1.91(10)	9.05(40)	3.182	0.195(3)	1.98(13)	8.70(97)
	3.206	0.4913	0.257(3)	1.49(10)	6.7(11)	3.529	0.283(8)	1.32(12)	7.68(60)
	3.505	0.4252	0.385(4)	0.91(11)	5.27(50)	3.838	0.415(13)	0.95(9)	5.17(74)
$Q^{*2} = 2$	2.657	0.6025	0.102(1)	3.25(33)	12.8(13)	2.961	0.116(1)	2.92(11)	10.9(23)
	2.990	0.5555	0.161(2)	2.20(12)	9.3(17)	3.330	0.180(3)	2.09(15)	10.3(12)
	3.316	0.5008	0.244(5)	1.50(10)	7.19(60)	3.676	0.273(2)	1.55(10)	7.63(76)
	3.658	0.4310	0.379(2)	1.02(8)	5.7(10)	3.977	0.403(15)	0.96(5)	5.20(60)
$Q^{*2} = 3$	2.765	0.6209	0.088(1)	3.67(11)	12.5(10)	3.149	0.105(1)	3.57(20)	13.1(14)
	3.160	0.5717	0.149(2)	2.66(14)	12.12(13)	3.524	0.167(4)	2.54(17)	11.45(82)
	3.471	0.5154	0.229(1)	1.68(10)	7.90(60)	3.835	0.248(4)	1.72(10)	8.30(60)
	3.847	0.4428	0.366(2)	1.20(7)	6.33(50)	4.145	0.390(11)	1.07(8)	6.02(40)
$Q^{*2} = 4$	2.952	0.6396	0.078(2)	4.52(20)	15.6(34)	3.316	0.092(1)	4.35(46)	15.14(96)
	3.349	0.5884	0.136(1)	2.83(18)	12.9(17)	3.694	0.153(2)	2.79(20)	14.38(80)
	3.673	0.5307	0.215(2)	1.89(10)	11.22(50)	4.071	0.238(5)	1.87(17)	8.8(10)
	4.026	0.4554	0.349(2)	1.10(7)	6.31(55)	4.433	0.380(8)	1.13(18)	7.1(10)

Table B.1.7: Transport coefficients of 2CLJQ fluids, for $L^* = 0.505$ and different quadrupole momentum Q^{*2}. The numbers in parentheses denote the uncertainty in the last digits.

$L^* = 0.505$	T^*	ρ^*	D^*	η^*	λ^*	T^*	D^*	η^*	λ^*
$Q^{*2} = 0$	1.638	0.5291	0.095(1)	2.02(6)	9.13(84)	1.901	0.109(1)	2.06(10)	10.16(75)
	1.913	0.4891	0.141(2)	1.55(8)	7.62(42)	2.159	0.158(2)	1.55(1)	8.17(31)
	2.190	0.4431	0.206(1)	1.10(6)	5.94(99)	2.467	0.230(5)	1.15(10)	6.08(83)
	2.476	0.3835	0.305(1)	0.79(4)	4.43(18)	2.729	0.330(2)	0.77(8)	4.30(39)
$Q^{*2} = 1$	1.652	0.5349	0.083(1)	2.29(14)	9.97(74)	1.943	0.099(2)	2.30(10)	9.87(49)
	1.924	0.4942	0.130(1)	1.67(6)	8.08(68)	2.221	0.149(2)	1.71(10)	7.86(20)
	2.187	0.4474	0.193(1)	1.19(4)	6.48(18)	2.490	0.217(2)	1.28(10)	6.45(40)
	2.509	0.3873	0.295(3)	0.81(5)	4.83(36)	2.757	0.328(13)	0.83(8)	4.88(30)
$Q^{*2} = 2$	1.728	0.5476	0.071(2)	2.80(20)	10.8(10)	1.972	0.083(7)	2.70(10)	10.1(11)
	2.029	0.5049	0.118(1)	1.96(28)	8.70(92)	2.294	0.134(2)	1.81(10)	8.78(40)
	2.288	0.4548	0.183(3)	1.34(23)	7.04(71)	2.580	0.205(2)	1.33(10)	7.02(30)
	2.584	0.3926	0.283(1)	0.85(5)	4.93(40)	2.853	0.310(2)	0.84(8)	4.76(20)
$Q^{*2} = 3$	1.813	0.5643	0.058(1)	3.67(27)	11.5(13)	2.125	0.072(1)	3.28(20)	13.1(14)
	2.102	0.5193	0.102(1)	2.40(13)	10.6(11)	2.420	0.121(1)	2.34(10)	10.2(18)
	2.393	0.4691	0.166(2)	1.52(11)	7.49(65)	2.739	0.189(2)	1.48(10)	7.59(33)
	2.692	0.4041	0.266(4)	0.95(10)	5.52(34)	3.041	0.297(1)	1.01(6)	5.48(31)
$Q^{*2} = 4$	1.922	0.5803	0.043(1)	5.28(74)	14.9(28)	2.236	0.061(1)	4.10(11)	12.8(16)
	2.252	0.5335	0.092(2)	2.66(13)	11.39(60)	2.546	0.108(1)	2.54(12)	11.16(47)
	2.541	0.4809	0.155(1)	1.71(10)	8.52(60)	2.878	0.177(3)	1.60(12)	8.07(53)
	2.885	0.4135	0.259(3)	1.02(8)	5.80(30)	3.203	0.288(1)	0.99(10)	6.32(15)

Table B.1.8: Transport coefficients of 2CLJQ fluids, for $L^* = 0.505$ and different quadrupole momentum Q^{*2}. The numbers in parentheses denote the uncertainty in the last digits.

$L^* = 0.505$	T^*	ρ^*	D^*	η^*	λ^*	T^*	D^*	η^*	λ^*
$Q^{*2} = 1$	2.166	0.5291	0.123(1)	2.10(15)	8.62(86)	2.463	0.139(2)	2.15(12)	8.45(53)
	2.438	0.4891	0.177(1)	1.45(8)	7.41(43)	2.724	0.194(2)	1.60(10)	7.64(56)
	2.740	0.4431	0.255(1)	1.22(5)	6.22(20)	2.981	0.270(10)	1.22(10)	6.40(30)
	3.035	0.3835	0.370(12)	0.78(4)	5.00(23)	3.307	0.402(21)	0.84(6)	5.25(24)
$Q^{*2} = 2$	2.223	0.5349	0.113(1)	2.28(13)	10.57(60)	2.481	0.127(1)	2.26(12)	9.33(71)
	2.473	0.4942	0.166(1)	1.64(8)	7.93(30)	2.759	0.183(5)	1.55(10)	7.70(30)
	2.762	0.4474	0.243(1)	1.23(7)	6.37(61)	3.064	0.262(8)	1.22(8)	6.74(66)
	3.067	0.3873	0.367(3)	0.92(7)	5.09(15)	3.300	0.380(16)	0.84(6)	4.77(23)
$Q^{*2} = 3$	2.310	0.5476	0.099(1)	2.92(29)	11.21(58)	2.598	0.114(1)	2.70(23)	10.9(12)
	2.571	0.5049	0.152(1)	1.86(12)	10.0(10)	2.883	0.170(2)	1.84(10)	9.46(94)
	2.849	0.4548	0.229(3)	1.29(6)	6.15(25)	3.150	0.249(7)	1.30(10)	6.85(31)
	3.171	0.3926	0.348(6)	0.87(5)	5.18(47)	3.475	0.375(12)	0.92(9)	5.02(78)
$Q^{*2} = 4$	2.404	0.5643	0.083(1)	3.35(34)	11.93(79)	2.708	0.098(1)	3.36(25)	10.60(21)
	2.708	0.5193	0.137(1)	2.26(10)	10.3(12)	3.017	0.154(1)	2.06(11)	8.81(36)
	3.013	0.4691	0.212(4)	1.55(8)	7.49(56)	3.302	0.231(6)	1.46(21)	6.48(51)
	3.331	0.4041	0.334(5)	1.00(8)	5.87(77)	3.616	0.354(13)	1.01(10)	5.55(38)
$Q^{*2} = 0$	2.583	0.5803	0.074(1)	3.81(10)	12.6(11)	2.885	0.088(1)	3.87(31)	12.7(25)
	2.903	0.5335	0.127(2)	2.56(14)	11.3(15)	3.212	0.143(3)	2.54(10)	10.3(11)
	3.193	0.4809	0.201(3)	1.58(12)	9.26(94)	3.506	0.220(5)	1.61(10)	8.44(28)
	3.520	0.4135	0.327(3)	1.03(8)	6.17(59)	3.842	0.346(5)	1.00(8)	5.85(59)

Table B.1.9: Transport coefficients of 2CLJQ fluids, for $L^* = 0.6$ and different quadrupole momentum Q^{*2}. The numbers in parentheses denote the uncertainty in the last digits.

$L^* = 0.6$	T^*	ρ^*	D^*	η^*	λ^*	T^*	D^*	η^*	λ^*
$Q^{*2} = 0$	1.475	0.4900	0.094(1)	1.76(8)	9.39(96)	1.719	0.107(2)	1.82(12)	8.91(32)
	1.726	0.4521	0.140(1)	1.37(8)	7.67(37)	1.959	0.156(3)	1.31(10)	7.58(80)
	1.948	0.4088	0.199(2)	1.02(6)	6.00(68)	2.213	0.223(5)	0.99(8)	5.94(64)
	2.211	0.3520	0.294(3)	0.66(6)	4.13(45)	2.452	0.329(16)	0.74(6)	3.92(20)
$Q^{*2} = 1$	1.490	0.4947	0.084(1)	2.01(8)	8.92(39)	1.742	0.098(16)	2.02(12)	9.07(16)
	1.731	0.4563	0.128(1)	1.45(8)	7.46(59)	1.995	0.146(1)	1.49(10)	6.85(47)
	2.011	0.4116	0.193(2)	1.10(4)	6.09(37)	2.252	0.212(2)	1.04(8)	6.05(64)
	2.233	0.3519	0.287(1)	0.70(3)	3.85(27)	2.500	0.317(3)	0.74(7)	4.45(30)
$Q^{*2} = 2$	1.552	0.5083	0.069(1)	2.42(11)	10.06(31)	1.822	0.083(1)	2.51(26)	9.69(61)
	1.810	0.4682	0.112(1)	1.72(9)	8.07(74)	2.067	0.128(2)	1.76(11)	8.20(61)
	2.080	0.4214	0.177(2)	1.19(14)	6.09(35)	2.351	0.198(1)	1.18(10)	6.37(20)
	2.314	0.3622	0.268(1)	0.79(4)	3.6(11)	2.586	0.298(2)	0.79(7)	4.94(40)
$Q^{*2} = 3$	1.610	0.5239	0.055(1)	3.04(26)	11.25(61)	1.894	0.066(3)	3.31(22)	10.4(11)
	1.879	0.4819	0.096(1)	2.05(6)	9.40(67)	2.154	0.113(1)	1.98(13)	9.17(82)
	2.137	0.4349	0.156(1)	1.38(9)	6.95(67)	2.412	0.176(1)	1.33(10)	7.02(46)
	2.435	0.3758	0.250(3)	0.90(4)	4.97(40)	2.672	0.274(2)	0.88(3)	4.92(40)
$Q^{*2} = 4$	1.725	0.5381	0.040(1)	4.84(23)	10.01(24)	2.015	0.059(1)	3.54(10)	11.6(20)
	2.023	0.4944	0.087(1)	2.37(6)	10.23(71)	2.287	0.102(1)	2.30(10)	10.28(87)
	2.284	0.4452	0.147(2)	1.52(5)	7.85(70)	2.587	0.169(2)	1.53(10)	7.83(85)
	2.608	0.3812	0.248(1)	0.99(7)	5.72(25)	2.853	0.271(3)	0.96(6)	5.64(65)

Table B.1.10: Transport coefficients of 2CLJQ fluids, for $L^* = 0.6$ and different quadrupole momentum Q^{*2}. The numbers in parentheses denote the uncertainty in the last digits.

$L^* = 0.6$	T^*	ρ^*	D^*	η^*	λ^*	T^*	D^*	η^*	λ^*
$Q^{*2} = 0$	1.949	0.4900	0.120(1)	1.75(7)	8.42(47)	2.211	0.135(1)	1.79(10)	8.97(93)
	2.225	0.4521	0.176(3)	1.45(13)	6.94(39)	2.444	0.189(3)	1.39(8)	6.69(59)
	2.457	0.4088	0.248(2)	1.17(3)	6.03(69)	2.705	0.265(8)	1.08(6)	5.40(54)
	2.699	0.3520	0.364(2)	0.74(5)	4.22(42)	2.933	0.391(15)	0.79(8)	4.10(23)
$Q^{*2} = 1$	1.993	0.4947	0.111(1)	1.97(10)	9.55(11)	2.245	0.126(1)	2.03(10)	9.12(33)
	2.243	0.4563	0.163(2)	1.42(4)	7.00(13)	2.498	0.180(3)	1.48(7)	7.72(50)
	2.493	0.4116	0.236(4)	1.11(7)	6.16(40)	2.731	0.254(7)	1.11(8)	6.2(10)
	2.749	0.3519	0.357(7)	0.74(2)	4.34(20)	2.978	0.380(14)	0.73(5)	4.51(38)
$Q^{*2} = 2$	2.076	0.5083	0.095(1)	2.48(10)	9.20(93)	2.317	0.108(2)	2.25(19)	10.23(74)
	2.327	0.4682	0.146(1)	1.73(18)	8.09(58)	2.583	0.162(3)	1.76(19)	7.88(98)
	2.579	0.4214	0.221(4)	1.13(10)	6.25(50)	2.864	0.240(4)	1.19(10)	6.66(64)
	2.865	0.3622	0.338(10)	0.79(5)	5.17(39)	3.100	0.363(18)	0.83(5)	4.67(51)
$Q^{*2} = 3$	2.163	0.5239	0.079(1)	2.87(10)	10.6(19)	2.459	0.095(1)	2.95(10)	11.56(63)
	2.405	0.4819	0.127(1)	1.93(9)	8.40(47)	2.709	0.147(2)	1.99(10)	9.4(11)
	2.727	0.4349	0.201(1)	1.34(3)	7.00(55)	2.959	0.214(4)	1.41(15)	7.47(40)
	2.984	0.3758	0.310(7)	0.86(8)	5.36(89)	3.202	0.332(10)	0.95(7)	5.32(30)
$Q^{*2} = 4$	2.291	0.5381	0.068(1)	3.87(28)	10.42(13)	2.574	0.082(2)	3.41(16)	10.9(15)
	2.586	0.4944	0.118(1)	2.38(5)	10.18(84)	2.884	0.136(1)	2.40(12)	10.03(51)
	2.837	0.4452	0.187(3)	1.59(5)	7.12(89)	3.181	0.211(5)	1.48(9)	7.43(92)
	3.121	0.3812	0.301(8)	0.91(6)	5.03(37)	3.438	0.331(11)	0.99(10)	6.10(95)

Table B.1.11: Transport coefficients of 2CLJQ fluids, for $L^* = 0.8$ and different quadrupole momentum Q^{*2}. The numbers in parentheses denote the uncertainty in the last digits.

$L^* = 0.8$	T^*	ρ^*	D^*	η^*	λ^*	T^*	D^*	η^*	λ^*
$Q^{*2} = 0$	1.234	0.4302	0.085(1)	1.51(10)	7.38(51)	1.440	0.097(2)	1.58(20)	8.24(20)
	1.426	0.3956	0.126(1)	1.13(8)	6.21(28)	1.643	0.142(1)	1.14(10)	6.90(51)
	1.632	0.3568	0.181(1)	0.85(7)	4.93(13)	1.839	0.199(1)	0.86(6)	4.94(50)
	1.856	0.3051	0.267(3)	0.58(3)	3.64(23)	2.031	0.288(1)	0.60(4)	3.34(46)
$Q^{*2} = 1$	1.246	0.4364	0.074(1)	1.69(10)	8.09(50)	1.459	0.088(1)	1.79(10)	8.03(92)
	1.458	0.4016	0.115(1)	1.23(4)	6.86(51)	1.686	0.131(1)	1.27(8)	6.56(66)
	1.686	0.3602	0.173(1)	0.89(5)	5.56(41)	1.883	0.190(1)	0.92(8)	5.22(22)
	1.885	0.3059	0.259(1)	0.60(3)	3.64(30)	2.111	0.286(2)	0.61(5)	3.70(30)
$Q^{*2} = 2$	1.308	0.4513	0.060(1)	2.23(10)	9.52(13)	1.513	0.071(1)	2.12(12)	8.76(81)
	1.514	0.4143	0.099(2)	1.46(7)	7.22(22)	1.718	0.112(1)	1.48(18)	7.62(74)
	1.712	0.3734	0.150(2)	1.02(6)	5.74(10)	1.954	0.171(1)	1.05(8)	5.92(58)
	1.933	0.3207	0.233(1)	0.70(4)	4.04(24)	2.155	0.258(4)	0.70(7)	4.01(20)
$Q^{*2} = 3$	1.352	0.4666	0.047(1)	2.91(20)	9.0(12)	1.590	0.059(1)	2.68(17)	9.71(32)
	1.579	0.4290	0.082(3)	1.85(10)	7.42(29)	1.814	0.098(1)	1.84(10)	8.39(90)
	1.801	0.3858	0.136(2)	1.24(7)	6.19(40)	2.050	0.154(2)	1.21(10)	6.40(38)
	2.045	0.3319	0.219(1)	0.78(7)	4.42(35)	2.270	0.242(2)	0.75(7)	4.26(59)
$Q^{*2} = 4$	1.447	0.4800	0.032(1)	4.92(20)	10.8(15)	1.669	0.046(1)	3.89(31)	10.5(15)
	1.674	0.4416	0.073(1)	2.18(13)	8.87(40)	1.945	0.088(1)	2.18(20)	8.96(94)
	1.914	0.3975	0.125(2)	1.42(12)	7.22(40)	2.171	0.143(2)	1.37(10)	6.60(53)
	2.187	0.3402	0.212(1)	0.90(8)	4.65(41)	2.401	0.233(3)	0.89(6)	4.75(43)

Table B.1.12: Transport coefficients of 2CLJQ fluids, for $L^* = 0.8$ and different quadrupole momentum Q^{*2}. The numbers in parentheses denote the uncertainty in the last digits.

$L^* = 0.8$	T^*	ρ^*	D^*	η^*	λ^*	T^*	D^*	η^*	λ^*
$Q^{*2} = 0$	1.647	0.4302	0.110(2)	1.63(10)	8.09(31)	1.852	0.123(1)	1.58(10)	7.74(48)
	1.854	0.3956	0.158(1)	1.25(7)	6.98(78)	2.051	0.174(3)	1.24(10)	6.25(17)
	2.062	0.3568	0.224(5)	0.90(8)	5.33(62)	2.259	0.240(6)	0.95(8)	5.22(39)
	2.240	0.3051	0.326(10)	0.61(7)	3.88(43)	2.462	0.357(15)	0.61(8)	3.53(18)
$Q^{*2} = 1$	1.674	0.4364	0.098(1)	1.84(10)	7.23(60)	1.889	0.112(1)	1.84(15)	9.45(28)
	1.883	0.4016	0.145(1)	1.35(12)	6.57(37)	2.076	0.159(2)	1.30(10)	7.09(70)
	2.092	0.3602	0.213(2)	0.90(5)	5.06(57)	2.314	0.231(2)	0.95(8)	4.98(20)
	2.314	0.3059	0.314(7)	0.62(7)	3.94(47)	2.513	0.347(17)	0.63(5)	3.60(34)
$Q^{*2} = 2$	1.735	0.4513	0.081(1)	2.42(14)	8.2(14)	1.955	0.094(3)	2.07(10)	9.0(13)
	1.946	0.4143	0.126(2)	1.42(12)	7.81(66)	2.170	0.142(1)	1.58(20)	6.23(29)
	2.162	0.3734	0.189(1)	1.02(10)	6.27(50)	2.376	0.208(4)	1.16(10)	5.64(54)
	2.370	0.3207	0.293(4)	0.74(6)	3.94(10)	2.588	0.311(12)	0.70(9)	4.07(46)
$Q^{*2} = 3$	1.809	0.4666	0.066(1)	2.94(21)	9.85(55)	2.019	0.079(2)	2.51(37)	8.5(16)
	2.026	0.4290	0.109(1)	1.77(12)	7.29(10)	2.262	0.124(2)	1.87(10)	8.10(51)
	2.267	0.3858	0.171(2)	1.24(13)	6.22(21)	2.491	0.189(2)	1.20(7)	7.17(63)
	2.483	0.3319	0.272(1)	0.80(7)	3.99(47)	2.734	0.294(3)	0.76(5)	4.23(58)
$Q^{*2} = 4$	1.940	0.4800	0.058(2)	3.31(23)	10.72(38)	2.165	0.069(1)	3.16(22)	12.4(15)
	2.135	0.4416	0.096(1)	2.23(22)	8.14(39)	2.415	0.113(1)	1.95(19)	8.5(12)
	2.388	0.3975	0.157(1)	1.42(12)	6.55(84)	2.666	0.178(3)	1.33(10)	7.01(36)
	2.674	0.3402	0.264(3)	0.90(9)	4.64(41)	2.887	0.282(10)	0.93(8)	4.51(68)

B.2 Self-diffusion, shear viscosity, and thermal conductivity for 2CLJD fluids

Tables B.2.1 to B.2.14 show the simulation results for the 2CLJQ fluids.

Table B.2.1: Transport coefficients of 2CLJD fluids, for $L^* = 0$ and different dipole momentum μ^{*2}. The numbers in parentheses denote the uncertainty in the last digits.

$L^* = 0$	T^*	ρ^*	D^*	η^*	λ^*	T^*	D^*	η^*	λ^*
$\mu^{*2} = 0$	3.139	0.8063	0.094(1)	4.66(26)	14.00(52)	3.923	0.125(1)	4.33(16)	13.81(46)
	3.925	0.7108	0.202(1)	2.56(16)	9.24(81)	4.708	0.243(1)	2.63(11)	9.94(60)
	4.708	0.5840	0.400(4)	1.48(10)	6.29(54)	5.491	0.456(1)	1.55(10)	7.03(36)
$\mu^{*2} = 3$	3.288	0.8202	0.083(1)	5.46(8)	13.04(89)	4.110	0.113(1)	5.11(24)	13.40(78)
	4.110	0.7245	0.184(1)	2.79(39)	10.12(10)	4.932	0.226(1)	3.05(17)	10.99(63)
	4.932	0.5966	0.372(1)	1.74(19)	7.26(32)	5.754	0.430(2)	1.76(10)	6.97(73)
$\mu^{*2} = 6$	3.597	0.8327	0.082(1)	6.02(21)	13.9(10)	4.496	0.113(1)	5.29(25)	14.4(16)
	4.494	0.7345	0.183(1)	3.14(35)	10.93(90)	5.394	0.224(1)	3.41(10)	10.9(12)
	5.395	0.6049	0.364(2)	1.94(10)	7.36(10)	6.294	0.424(1)	1.94(12)	7.5(11)
$\mu^{*2} = 9$	3.954	0.8419	0.084(1)	7.44(72)	16.41(31)	4.944	0.116(1)	5.65(32)	15.8(14)
	4.943	0.7407	0.187(1)	3.41(19)	13.6(10)	5.931	0.231(1)	3.57(21)	10.64(50)
	5.931	0.6082	0.370(1)	1.95(10)	7.01(10)	6.919	0.433(1)	1.84(15)	8.2(14)
$\mu^{*2} = 12$	4.378	0.8456	0.093(1)	8.99(79)	18.8(11)	5.472	0.126(1)	6.67(69)	16.49(45)
	5.470	0.7404	0.199(1)	3.56(20)	14.1(10)	6.565	0.245(1)	3.45(16)	14.9(18)
	6.564	0.6024	0.395(1)	1.62(28)	9.32(17)	7.659	0.464(2)	1.91(10)	7.6(11)
$\mu^{*2} = 16$	4.956	0.8516	0.104(1)	18.8(16)	20.7(20)	6.192	0.137(1)	9.13(60)	17.4(35)
	6.192	0.7400	0.215(1)	3.75(23)	15.8(18)	7.430	0.267(1)	3.54(28)	12.3(14)
	7.429	0.5968	0.426(1)	1.93(10)	8.91(18)	8.667	0.499(2)	1.85(11)	8.65(94)
$\mu^{*2} = 20$	5.505	0.8632	0.113(1)	66.4(70)	19.9(11)	6.879	0.145(1)	12.41(80)	15.5(23)
	6.878	0.7445	0.226(1)	4.64(10)	3.98(20)	8.253	0.280(1)	4.51(33)	14.9(19)
	8.254	0.5972	0.441(1)	2.29(10)	9.93(42)	9.628	0.522(2)	2.17(10)	8.3(11)

Table B.2.2: Transport coefficients of 2CLJD fluids, for $L^* = 0$ and different dipole momentum μ^{*2}. The numbers in parentheses denote the uncertainty in the last digits.

$L^*=0$	T^*	ρ^*	D^*	η^*	λ^*	T^*	D^*	η^*	λ^*
$\mu^{*2}=0$	4.722	0.8063	0.154(1)	4.00(13)	14.7(12)	5.486	0.188(2)	4.04(13)	14.41(62)
	5.499	0.7108	0.283(2)	2.70(21)	9.70(63)	6.280	0.323(3)	2.57(13)	10.24(53)
	6.286	0.5840	0.509(3)	1.65(10)	7.00(14)	7.071	0.561(1)	1.69(10)	7.07(23)
$\mu^{*2}=3$	4.931	0.8202	0.145(1)	3.90(36)	12.9(14)	5.755	0.174(1)	4.67(12)	15.2(10)
	5.753	0.7245	0.266(1)	2.90(23)	10.90(42)	6.574	0.306(1)	3.02(15)	10.37(62)
	6.577	0.5966	0.486(1)	1.70(10)	6.99(64)	7.395	0.541(2)	1.76(11)	7.33(30)
$\mu^{*2}=6$	5.395	0.8327	0.144(1)	5.29(17)	15.07(92)	6.294	0.175(1)	4.87(16)	14.6(13)
	6.293	0.7345	0.266(1)	3.35(24)	11.2(12)	7.193	0.307(1)	3.02(31)	12.0(17)
	7.193	0.6049	0.484(1)	1.77(10)	8.13(44)	8.091	0.540(1)	1.76(14)	8.87(21)
$\mu^{*2}=9$	5.932	0.8419	0.148(1)	5.43(32)	16.9(30)	6.920	0.181(1)	5.50(61)	16.78(25)
	6.919	0.7407	0.272(1)	3.21(25)	12.45(67)	7.907	0.317(1)	3.22(10)	11.8(12)
	7.907	0.6082	0.497(2)	1.97(10)	7.59(85)	8.896	0.555(2)	1.91(10)	8.80(66)
$\mu^{*2}=12$	6.565	0.8456	0.160(1)	5.99(11)	16.2(15)	7.660	0.193(1)	5.78(32)	17.34(13)
	7.659	0.7404	0.292(1)	3.38(17)	12.4(14)	8.753	0.337(1)	3.33(10)	14.77(10)
	8.752	0.6024	0.531(1)	1.98(10)	8.78(99)	9.845	0.594(1)	2.00(16)	8.46(95)
$\mu^{*2}=16$	7.431	0.8516	0.173(1)	6.21(59)	17.1(16)	8.669	0.209(1)	6.03(53)	18.99(99)
	8.668	0.7400	0.319(1)	3.61(15)	13.2(15)	9.905	0.367(1)	3.30(39)	14.14(46)
	9.906	0.5968	0.573(3)	1.94(21)	9.87(31)	11.14	0.644(2)	2.02(23)	10.54(77)
$\mu^{*2}=20$	8.254	0.8632	0.183(1)	7.99(29)	22.43(36)	9.630	0.220(1)	7.56(10)	18.29(50)
	9.628	0.7445	0.333(1)	3.90(50)	14.42(82)	11.00	0.385(1)	3.73(10)	13.3(11)
	11.004	0.5972	0.598(1)	2.08(34)	9.35(75)	12.38	0.677(1)	1.98(15)	8.6(11)

Table B.2.3: Transport coefficients of 2CLJD fluids, for $L^* = 0.2$ and different dipole momentum μ^{*2}. The numbers in parentheses denote the uncertainty in the last digits.

$L^* = 0.2$	T^*	ρ^*	D^*	η^*	λ^*	T^*	D^*	η^*	λ^*
$\mu^{*2} = 0$	2.589	0.7114	0.088(1)	3.94(5)	11.18(62)	3.237	0.118(1)	3.87(10)	11.50(10)
	3.236	0.6275	0.190(1)	2.19(7)	8.6(12)	3.884	0.229(1)	2.03(10)	8.77(47)
	3.884	0.5144	0.377(1)	1.20(6)	5.66(35)	4.531	0.433(1)	1.14(6)	6.13(57)
$\mu^{*2} = 3$	2.715	0.7220	0.086(1)	4.21(42)	12.09(22)	3.393	0.115(1)	3.96(20)	16.96(52)
	3.393	0.6367	0.189(1)	2.19(10)	10.42(47)	4.072	0.227(1)	2.19(10)	11.58(50)
	4.072	0.5244	0.372(2)	1.34(10)	8.30(77)	4.751	0.429(1)	1.38(8)	8.79(95)
$\mu^{*2} = 6$	2.952	0.7307	0.091(1)	4.27(50)	17.6(10)	3.691	0.121(1)	3.77(22)	21.4(33)
	3.691	0.6439	0.197(1)	2.27(18)	15.73(86)	4.429	0.238(1)	2.41(15)	15.36(18)
	4.428	0.5306	0.389(1)	1.34(10)	11.2(19)	5.167	0.445(1)	1.33(7)	9.02(13)
$\mu^{*2} = 9$	3.233	0.7370	0.098(1)	4.22(10)	26.67(98)	4.040	0.130(1)	3.97(45)	25.5(40)
	4.040	0.6481	0.211(1)	2.42(10)	22.0(11)	4.848	0.253(1)	2.42(14)	15.9(24)
	4.848	0.5315	0.415(2)	1.20(10)	11.9(19)	5.656	0.472(2)	1.51(12)	10.1(19)
$\mu^{*2} = 12$	3.572	0.7388	0.110(1)	4.32(43)	29.4(21)	4.464	0.144(1)	4.10(17)	30.0(41)
	4.463	0.6463	0.235(1)	2.55(34)	24.7(31)	5.356	0.282(1)	2.29(17)	19.4(30)
	5.355	0.5226	0.466(1)	1.38(10)	11.5(15)	6.247	0.533(1)	1.56(10)	12.9(19)
$\mu^{*2} = 16$	3.998	0.7438	0.123(1)	4.75(18)	33.5(55)	4.997	0.162(1)	4.21(43)	27.7(10)
	4.996	0.6497	0.258(1)	2.58(23)	24.9(23)	5.995	0.308(2)	2.38(16)	23.1(14)
	5.994	0.5229	0.507(1)	1.18(15)	15.94(30)	6.991	0.465(1)	1.85(17)	9.2(15)

Table B.2.4: Transport coefficients of 2CLJD fluids, for $L^* = 0.2$ and different dipole momentum μ^{*2}. The numbers in parentheses denote the uncertainty in the last digits.

$L^* = 0.2$	T^*	ρ^*	D^*	η^*	λ^*	T^*	D^*	η^*	λ^*
$\mu^{*2} = 0$	3.884	0.7114	0.146(1)	3.53(51)	12.5(11)	4.532	0.174(1)	3.48(21)	12.5(14)
	4.532	0.6275	0.265(1)	2.14(12)	9.09(57)	5.179	0.303(2)	2.18(10)	9.11(10)
	5.178	0.5144	0.483(1)	1.27(10)	5.50(27)	5.825	0.533(1)	1.28(10)	6.75(10)
$\mu^{*2} = 3$	4.071	0.7220	0.144(1)	3.88(37)	15.44(80)	4.750	0.172(1)	3.46(10)	12.6(26)
	4.750	0.6367	0.265(1)	2.15(10)	11.92(62)	5.428	0.302(1)	2.22(10)	11.7(11)
	5.428	0.5244	0.479(2)	1.34(8)	7.61(55)	6.108	0.533(1)	1.36(14)	7.78(82)
$\mu^{*2} = 6$	5.166	0.7307	0.180(1)	3.77(16)	16.61(31)	5.167	0.180(1)	3.82(10)	14.4(32)
	5.167	0.6439	0.277(1)	2.41(12)	14.97(15)	5.905	0.315(1)	2.44(21)	13.84(10)
	5.904	0.5306	0.497(1)	1.41(8)	10.94(23)	6.642	0.552(1)	1.23(16)	9.03(37)
$\mu^{*2} = 9$	4.848	0.7370	0.162(1)	3.86(37)	24.7(25)	5.656	0.193(1)	3.39(19)	20.04(14)
	5.656	0.6481	0.297(1)	2.33(10)	14.9(25)	6.463	0.336(1)	2.33(10)	16.9(10)
	6.463	0.5319	0.534(2)	1.52(8)	12.71(94)	7.272	0.590(2)	1.46(8)	9.66(51)
$\mu^{*2} = 12$	5.356	0.7388	0.180(1)	3.85(20)	26.92(21)	6.248	0.215(1)	3.81(51)	24.7(71)
	6.248	0.6463	0.326(1)	2.29(10)	19.39(76)	7.140	0.370(1)	2.98(10)	20.0(24)
	7.140	0.5226	0.597(2)	1.39(7)	13.91(64)	8.032	0.662(2)	1.51(9)	15.99(83)
$\mu^{*2} = 16$	5.996	0.7438	0.200(1)	4.25(32)	35.9(49)	6.994	0.238(1)	3.70(13)	35.7(51)
	6.994	0.6497	0.359(1)	2.50(11)	20.2(10)	7.993	0.408(1)	2.26(11)	16.9(29)
	7.990	0.5229	0.518(2)	1.88(8)	7.64(93)	8.988	0.574(2)	1.91(8)	10.17(28)

Table B.2.5: Transport coefficients of 2CLJD fluids, for $L^* = 0.4$ and different dipole momentum μ^{*2}. The numbers in *parentheses denote the uncertainty in the last digits.*

$L^* = 0.4$	T^*	ρ^*	D^*	η^*	λ^*	T^*	D^*	η^*	λ^*
$\mu^{*2} = 0$	1.899	0.5810	0.093(1)	2.71(10)	10.0(22)	2.374	0.119(1)	2.50(10)	10.07(55)
	2.374	0.5123	0.187(1)	1.55(7)	7.8(10)	2.848	0.221(1)	1.63(8)	7.62(60)
	2.848	0.4185	0.360(1)	0.91(9)	4.84(10)	3.323	0.409(1)	0.83(7)	5.04(32)
$\mu^{*2} = 3$	1.988	0.5881	0.088(1)	2.97(15)	11.18(22)	2.485	0.115(1)	2.85(12)	11.3(17)
	2.485	0.5179	0.182(1)	1.80(18)	9.88(83)	2.982	0.218(1)	1.73(10)	7.54(35)
	2.982	0.4262	0.351(2)	0.94(8)	5.90(16)	3.479	0.401(1)	0.93(8)	4.84(50)
$\mu^{*2} = 6$	2.156	0.5932	0.086(1)	2.86(17)	11.36(42)	2.695	0.115(1)	2.95(13)	12.94(54)
	2.695	0.5225	0.182(1)	1.84(10)	9.95(38)	3.234	0.220(1)	1.67(12)	9.1(12)
	3.234	0.4275	0.360(1)	0.95(8)	6.22(30)	3.773	0.414(2)	0.95(8)	5.11(63)
$\mu^{*2} = 9$	2.347	0.5973	0.086(1)	3.52(18)	14.70(57)	2.934	0.116(1)	2.97(13)	14.9(31)
	2.934	0.5254	0.186(1)	1.86(10)	10.88(64)	3.520	0.224(1)	1.78(12)	10.2(12)
	3.521	0.4296	0.368(1)	0.98(8)	8.02(50)	4.107	0.427(1)	1.09(10)	7.6(13)
$\mu^{*2} = 12$	2.571	0.5988	0.090(1)	3.49(11)	13.4(15)	3.214	0.133(21)	2.97(14)	13.4(24)
	3.214	0.5243	0.194(1)	1.92(19)	12.61(98)	3.856	0.239(1)	1.92(10)	12.2(19)
	3.856	0.4257	0.390(1)	1.16(8)	6.88(40)	4.499	0.455(2)	1.13(10)	6.6(12)

Table B.2.6: Transport coefficients of 2CLJD fluids, for $L^* = 0.4$ and different dipole momentum μ^{*2}. The numbers in parentheses denote the uncertainty in the last digits.

$L^* = 0.4$	T^*	ρ^*	D^*	η^*	λ^*	T^*	D^*	η^*	λ^*
$\mu^{*2} = 0$	2.848	0.5810	0.144(1)	2.53(15)	11.52(59)	3.323	0.170(1)	2.33(10)	9.82(64)
	3.323	0.5123	0.254(1)	1.59(10)	7.44(85)	3.798	0.288(1)	1.52(8)	7.44(29)
	3.798	0.4185	0.456(1)	0.95(8)	5.04(23)	4.272	0.504(1)	0.96(10)	4.65(10)
$\mu^{*2} = 3$	2.982	0.5881	0.141(1)	2.73(10)	11.09(65)	3.479	0.167(1)	2.82(25)	11.7(14)
	3.479	0.5179	0.252(1)	1.78(10)	8.07(71)	3.976	0.286(1)	1.62(10)	8.52(81)
	3.976	0.4262	0.450(1)	0.95(8)	5.92(20)	4.473	0.496(1)	1.04(12)	6.4(14)
$\mu^{*2} = 6$	3.234	0.5932	0.142(1)	2.91(10)	11.90(89)	3.773	0.169(1)	2.52(21)	12.1(15)
	3.773	0.5225	0.257(1)	1.69(12)	9.8(10)	4.312	0.292(1)	1.83(8)	9.80(40)
	4.312	0.4275	0.463(1)	1.10(10)	7.28(20)	4.851	0.518(1)	1.00(6)	7.22(73)
$\mu^{*2} = 9$	3.521	0.5973	0.145(1)	2.85(24)	13.98(11)	4.107	0.175(1)	3.14(15)	12.74(50)
	4.107	0.5254	0.263(1)	1.82(16)	9.56(24)	4.694	0.304(1)	1.67(10)	9.88(30)
	4.694	0.4296	0.478(2)	1.09(8)	8.37(42)	5.281	0.534(1)	1.29(9)	7.05(50)
$\mu^{*2} = 12$	3.856	0.5988	0.153(1)	3.00(10)	15.3(13)	4.499	0.185(1)	2.63(10)	13.7(33)
	4.499	0.5243	0.280(1)	1.93(19)	12.3(18)	5.142	0.321(1)	1.96(7)	10.28(80)
	5.142	0.4257	0.511(2)	1.15(10)	7.76(33)	5.785	0.575(1)	1.10(6)	8.16(94)

Table B.2.7: Transport coefficients of 2CLJD fluids, for $L^* = 0.505$ and different dipole momentum μ^{*2}. The numbers in parentheses denote the uncertainty in the last digits.

$L^* = 0.505$	T^*	ρ^*	D^*	η^*	λ^*	T^*	D^*	η^*	λ^*
$\mu^{*2} = 0$	1.642	0.5293	0.092(1)	2.24(20)	9.99(85)	2.053	0.117(1)	2.38(13)	9.6(13)
	2.052	0.4637	0.184(7)	1.35(10)	6.01(10)	2.463	0.212(1)	1.45(10)	7.49(50)
	2.463	0.3834	0.339(1)	0.84(7)	4.16(28)	2.874	0.385(1)	0.81(10)	4.90(24)
$\mu^{*2} = 3$	1.724	0.5346	0.087(1)	2.66(20)	9.60(79)	2.155	0.112(1)	2.12(30)	10.53(94)
	2.155	0.4711	0.175(1)	1.42(13)	8.10(94)	2.585	0.209(1)	1.46(14)	6.64(84)
	2.586	0.3854	0.339(1)	0.85(8)	5.33(36)	3.016	0.388(1)	0.70(6)	5.55(40)
$\mu^{*2} = 6$	1.861	0.5392	0.082(1)	2.92(20)	10.78(16)	2.326	0.108(1)	2.70(17)	10.0(27)
	2.327	0.4748	0.171(1)	1.44(10)	7.57(78)	2.792	0.207(1)	1.52(13)	7.5(11)
	2.792	0.3902	0.334(2)	0.84(8)	5.09(20)	3.257	0.386(1)	0.91(17)	5.37(21)
$\mu^{*2} = 9$	2.027	0.5424	0.080(1)	3.11(14)	10.81(69)	2.534	0.108(1)	2.70(16)	13.62(84)
	2.535	0.4765	0.171(1)	1.67(11)	9.7(13)	3.041	0.210(1)	1.64(13)	8.84(21)
	3.041	0.3898	0.342(1)	0.88(8)	6.47(99)	3.548	0.396(2)	0.86(8)	4.61(37)
$\mu^{*2} = 12$	2.207	0.5457	0.079(1)	3.38(20)	12.58(20)	2.759	0.109(1)	2.91(14)	12.0(10)
	2.759	0.4778	0.175(1)	1.83(10)	10.2(16)	3.311	0.215(1)	1.74(11)	10.3(13)
	3.311	0.3886	0.351(2)	0.83(20)	6.92(40)	3.862	0.410(1)	1.01(8)	5.72(12)

Table B.2.8: Transport coefficients of 2CLJD fluids, for $L^* = 0.505$ and different dipole momentum μ^{*2}. The numbers in parentheses denote the uncertainty in the last digits.

$L^* = 0.505$	T^*	ρ^*	D^*	η^*	λ^*	T^*	D^*	η^*	λ^*
$\mu^{*2} = 0$	2.463	0.5293	0.141(1)	2.08(10)	10.67(29)	2.874	0.165(1)	2.20(19)	9.45(80)
	2.874	0.4670	0.243(1)	1.39(12)	7.06(71)	3.284	0.275(1)	1.47(10)	7.55(85)
	3.284	0.3834	0.428(1)	0.73(8)	4.60(35)	3.694	0.473(1)	0.78(5)	5.29(60)
$\mu^{*2} = 3$	2.585	0.5346	0.138(1)	2.51(18)	9.58(56)	3.016	0.162(1)	2.14(12)	9.66(96)
	3.016	0.4711	0.241(1)	1.36(12)	7.22(81)	3.447	0.274(1)	1.22(10)	7.60(80)
	3.447	0.3854	0.431(1)	0.79(40)	4.31(47)	3.878	0.481(2)	0.91(6)	4.94(55)
$\mu^{*2} = 6$	2.792	0.5392	0.135(1)	2.41(17)	12.98(24)	3.257	0.162(1)	2.21(11)	12.8(11)
	3.257	0.4748	0.242(1)	1.48(10)	8.3(14)	3.722	0.277(1)	1.37(10)	7.38(86)
	3.722	0.3902	0.432(1)	0.86(7)	5.0(18)	4.188	0.482(1)	0.87(9)	5.66(75)
$\mu^{*2} = 9$	3.041	0.5424	0.136(1)	2.81(30)	11.3(11)	3.548	0.164(1)	2.45(23)	13.0(12)
	3.548	0.4765	0.248(1)	1.67(12)	8.26(34)	4.055	0.284(1)	1.55(10)	9.09(95)
	4.055	0.3898	0.448(1)	0.89(4)	6.49(61)	4.562	0.500(1)	0.93(8)	5.07(70)
$\mu^{*2} = 12$	3.311	0.5457	0.139(1)	2.89(17)	12.14(10)	3.863	0.169(1)	2.89(12)	14.1(13)
	3.862	0.4778	0.255(1)	1.71(12)	10.4(12)	4.414	0.294(1)	1.73(9)	8.70(90)
	4.414	0.3886	0.465(1)	1.02(5)	6.28(25)	4.966	0.522(1)	0.91(6)	5.57(45)

Table B.2.9: Transport coefficients of 2CLJD fluids, for $L^* = 0.6$ and different dipole momentum μ^{*2}. The numbers in parentheses denote the uncertainty in the last digits.

$L^* = 0.6$	T^*	ρ^*	D^*	η^*	λ^*	T^*	D^*	η^*	λ^*
$\mu^{*2} = 0$	1.473	0.4900	0.091(1)	2.16(15)	9.25(47)	1.842	0.114(1)	2.07(30)	8.97(79)
	1.842	0.4321	0.174(1)	1.14(10)	6.85(10)	2.210	0.205(1)	1.26(13)	6.92(64)
	2.210	0.3515	0.332(1)	0.71(5)	4.15(41)	2.578	0.377(1)	0.77(4)	4.36(12)
$\mu^{*2} = 3$	1.536	0.4960	0.082(1)	2.19(15)	7.95(31)	1.920	0.107(1)	2.25(10)	8.9(13)
	1.920	0.4372	0.166(1)	1.27(10)	5.41(43)	2.304	0.197(1)	1.38(10)	7.66(88)
	2.303	0.3597	0.317(1)	0.83(12)	4.78(20)	2.687	0.360(1)	0.77(11)	4.41(39)
$\mu^{*2} = 6$	1.665	0.4995	0.077(1)	2.08(39)	9.8(17)	2.082	0.102(1)	2.43(23)	9.82(86)
	2.082	0.4398	0.160(1)	1.34(10)	7.73(40)	2.498	0.195(1)	1.41(12)	7.25(69)
	2.498	0.3583	0.319(1)	0.79(10)	5.12(35)	2.914	0.368(1)	0.91(4)	4.95(32)
$\mu^{*2} = 9$	1.825	0.5006	0.076(1)	2.91(12)	11.45(41)	2.281	0.103(1)	2.42(24)	10.9(28)
	2.281	0.4378	0.165(1)	1.75(15)	7.00(95)	2.738	0.202(1)	1.43(10)	7.69(15)
	2.738	0.3545	0.332(1)	0.84(7)	6.22(59)	3.194	0.387(2)	0.86(6)	5.87(10)
$\mu^{*2} = 12$	1.965	0.5062	0.071(1)	3.28(12)	9.71(44)	2.456	0.099(1)	2.78(21)	12.23(14)
	2.456	0.4429	0.159(1)	1.62(10)	7.80(16)	2.947	0.197(1)	1.60(50)	8.86(55)
	2.948	0.3603	0.322(1)	0.89(7)	5.94(20)	3.439	0.381(2)	0.92(11)	6.27(22)

Table B.2.10: Transport coefficients of 2CLJD fluids, for $L^* = 0.6$ and different dipole momentum μ^{*2}. The numbers in parentheses denote the uncertainty in the last digits.

$L^* = 0.6$	T^*	ρ^*	D^*	η^*	λ^*	T^*	D^*	η^*	λ^*
$\mu^{*2} = 0$	2.210	0.4900	0.137(1)	1.81(16)	8.39(35)	2.578	0.160(1)	2.01(10)	7.12(13)
	2.578	0.4321	0.236(1)	1.27(10)	6.72(23)	2.947	0.267(1)	1.18(10)	7.34(30)
	2.946	0.3515	0.418(1)	0.74(7)	4.76(44)	3.315	0.464(2)	0.76(4)	4.57(35)
$\mu^{*2} = 3$	2.304	0.4960	0.131(1)	2.04(12)	9.39(62)	2.688	0.154(1)	1.80(10)	12.1(10)
	2.688	0.4372	0.228(1)	1.44(10)	6.86(22)	3.072	0.259(1)	1.29(7)	7.24(21)
	3.071	0.3597	0.403(1)	0.77(8)	4.64(22)	3.456	0.448(2)	0.78(6)	5.10(90)
$\mu^{*2} = 6$	2.498	0.4995	0.128(1)	2.26(10)	10.04(22)	2.914	0.153(1)	2.58(15)	9.01(96)
	2.914	0.4398	0.227(1)	1.25(20)	8.11(27)	3.331	0.262(1)	1.40(10)	7.92(10)
	3.331	0.3583	0.415(2)	0.84(8)	4.69(18)	3.747	0.465(2)	0.66(6)	4.85(19)
$\mu^{*2} = 9$	2.738	0.5006	0.130(1)	2.62(20)	10.7(11)	3.194	0.157(1)	2.48(16)	10.2(18)
	3.194	0.4378	0.238(1)	1.43(10)	6.34(71)	3.650	0.273(1)	1.40(10)	8.12(43)
	3.651	0.3545	0.436(2)	0.88(7)	5.73(51)	4.107	0.489(1)	0.91(8)	5.46(36)
$\mu^{*2} = 12$	2.948	0.5062	0.126(1)	2.71(20)	11.71(67)	3.439	0.154(1)	2.34(23)	12.7(11)
	3.439	0.4429	0.235(1)	1.57(11)	9.88(98)	3.930	0.272(1)	1.49(10)	8.6(14)
	3.930	0.3603	0.433(2)	0.98(6)	5.73(64)	4.421	0.488(2)	0.90(7)	5.3(10)

Table B.2.11: Transport coefficients of 2CLJD fluids, for $L^* = 0.8$ and different dipole momentum μ^{*2}. The numbers in *parentheses denote the uncertainty in the last digits.*

$L^* = 0.8$	T^*	ρ^*	D^*	η^*	λ^*	T^*	D^*	η^*	λ^*
$\mu^{*2} = 0$	1.230	0.4302	0.081(1)	1.79(10)	8.29(33)	1.538	0.102(1)	1.88(21)	7.53(12)
	1.538	0.3777	0.157(1)	1.11(14)	4.98(18)	1.845	0.186(1)	1.13(13)	5.01(70)
	1.845	0.3039	0.306(1)	0.60(5)	3.86(14)	2.153	0.345(1)	0.55(4)	3.54(36)
$\mu^{*2} = 3$	1.277	0.4364	0.071(1)	2.18(19)	8.52(31)	1.596	0.092(1)	1.84(10)	8.19(10)
	1.596	0.3833	0.145(1)	1.27(14)	6.56(10)	1.916	0.174(1)	1.20(12)	6.13(79)
	1.915	0.3101	0.287(1)	0.62(7)	3.67(10)	2.235	0.330(1)	0.68(7)	3.66(45)
$\mu^{*2} = 6$	1.390	0.4383	0.065(1)	2.25(45)	8.85(15)	1.738	0.088(1)	2.10(16)	8.22(13)
	1.738	0.3835	0.141(1)	1.27(8)	5.7(10)	2.086	0.172(1)	1.31(17)	7.02(82)
	2.086	0.3085	0.288(1)	0.64(4)	3.39(60)	2.433	0.336(1)	0.72(5)	3.34(37)
$\mu^{*2} = 9$	1.513	0.4410	0.060(1)	2.44(10)	9.1(10)	1.891	0.084(1)	2.38(25)	9.96(94)
	1.891	0.3855	0.137(1)	1.39(10)	7.25(10)	2.269	0.169(1)	1.36(10)	6.11(66)
	2.270	0.3093	0.286(2)	0.70(5)	4.32(34)	2.648	0.335(1)	0.72(11)	4.08(65)
$\mu^{*2} = 12$	1.629	0.4466	0.054(1)	3.02(80)	9.84(80)	2.036	0.078(1)	2.67(20)	10.9(21)
	2.036	0.3899	0.130(1)	1.47(10)	7.52(26)	2.443	0.163(1)	1.41(21)	7.3(10)
	2.443	0.3155	0.274(2)	0.74(5)	4.92(57)	2.851	0.324(1)	0.75(5)	4.4(12)

Table B.2.12: Transport coefficients of 2CLJD fluids, for $L^* = 0.8$ and different dipole momentum μ^{*2}. The numbers in parentheses denote the uncertainty in the last digits.

$L^* = 0.8$	T^*	ρ^*	D^*	η^*	λ^*	T^*	D^*	η^*	λ^*
$\mu^{*2} = 0$	1.845	0.4302	0.123(1)	1.62(10)	8.21(51)	2.153	0.143(1)	1.64(10)	7.80(40)
	2.153	0.3777	0.212(1)	1.11(9)	6.42(10)	2.460	0.240(1)	1.12(10)	5.62(50)
	2.460	0.3039	0.383(1)	0.60(3)	4.07(17)	2.768	0.427(1)	0.72(6)	4.31(40)
$\mu^{*2} = 3$	1.915	0.4364	0.114(1)	1.87(10)	9.12(74)	2.235	0.133(1)	1.85(10)	8.47(30)
	2.235	0.3833	0.202(1)	1.23(8)	5.91(52)	2.554	0.228(1)	1.33(10)	5.19(74)
	2.554	0.3101	0.369(1)	0.68(5)	4.28(10)	2.873	0.411(2)	0.69(5)	4.05(58)
$\mu^{*2} = 6$	2.086	0.4383	0.111(1)	2.08(10)	8.42(11)	2.433	0.132(1)	2.13(11)	7.8(16)
	2.433	0.3835	0.203(1)	1.26(10)	6.83(34)	2.781	0.231(1)	1.10(10)	6.88(44)
	2.781	0.3085	0.378(1)	0.72(3)	4.19(74)	3.129	0.426(2)	0.66(6)	4.16(33)
$\mu^{*2} = 9$	2.269	0.4410	0.108(1)	2.30(12)	9.15(59)	2.648	0.131(1)	1.99(22)	9.21(80)
	2.647	0.3855	0.201(1)	1.32(8)	7.66(59)	3.026	0.233(1)	1.39(17)	6.5(13)
	3.026	0.3093	0.381(1)	0.71(3)	4.29(35)	3.404	0.430(2)	0.72(8)	3.32(10)
$\mu^{*2} = 12$	2.443	0.4466	0.102(1)	2.50(16)	8.7(17)	2.850	0.126(1)	2.35(12)	8.16(17)
	2.851	0.3899	0.195(1)	1.50(6)	8.03(47)	3.258	0.229(1)	1.46(19)	6.66(95)
	3.258	0.3155	0.373(2)	0.67(3)	4.95(72)	3.665	0.420(2)	0.85(4)	4.16(10)

Table B.2.13: Transport coefficients of 2CLJD fluids, for $L^* = 1.0$ and different dipole momentum μ^{*2}. The numbers in parentheses denote the uncertainty in the last digits.

$L^* = 1.0$	T^*	ρ^*	D^*	η^*	λ^*	T^*	D^*	η^*	λ^*
$\mu^{*2} = 0$	1.058	0.3970	0.064(1)	1.71(15)	7.12(41)	1.322	0.082(1)	1.88(16)	7.30(60)
	1.322	0.3487	0.128(1)	0.98(9)	4.75(35)	1.587	0.152(1)	1.03(8)	5.29(37)
	1.587	0.2860	0.245(1)	0.62(6)	3.50(10)	1.851	0.280(1)	0.67(5)	3.82(30)
$\mu^{*2} = 3$	1.126	0.3976	0.059(1)	1.96(17)	7.33(39)	1.408	0.078(1)	1.78(10)	7.34(63)
	1.408	0.3463	0.127(1)	1.18(10)	4.73(30)	1.689	0.153(1)	1.05(8)	5.14(40)
	1.689	0.2793	0.257(1)	0.56(4)	4.09(40)	1.971	0.294(1)	0.61(6)	3.76(31)
$\mu^{*2} = 6$	1.207	0.4041	0.048(1)	2.50(15)	7.45(78)	1.508	0.067(1)	2.08(34)	7.71(65)
	1.508	0.3524	0.113(1)	1.24(20)	6.04(30)	1.810	0.140(1)	1.29(2)	6.49(69)
	1.810	0.2887	0.232(4)	0.67(4)	3.62(17)	2.112	0.276(1)	0.73(6)	3.76(36)
$\mu^{*2} = 9$	1.308	0.4101	0.039(1)	3.31(30)	8.54(80)	1.635	0.059(1)	2.67(20)	8.3(15)
	1.635	0.3576	0.104(1)	1.56(15)	5.22(20)	1.961	0.131(1)	1.40(10)	6.10(77)
	1.961	0.2900	0.228(1)	0.72(5)	4.30(25)	2.288	0.268(1)	0.71(10)	4.26(29)
$\mu^{*2} = 12$	1.423	0.4163	0.033(1)	4.09(30)	8.98(30)	1.779	0.052(1)	3.57(30)	9.14(26)
	1.779	0.3625	0.097(1)	1.75(10)	6.64(98)	2.134	0.125(1)	1.72(15)	6.65(78)
	2.134	0.2923	0.223(1)	0.75(7)	3.92(34)	2.490	0.264(1)	0.75(11)	4.37(24)

Table B.2.14: Transport coefficients of 2CLJD fluids, for $L^* = 1.0$ and different dipole momentum μ^{*2}. The numbers in parentheses denote the uncertainty in the last digits.

$L^* = 1.0$	T^*	ρ^*	D^*	η^*	λ^*	T^*	D^*	η^*	λ^*
$\mu^{*2} = 0$	1.587	0.3970	0.098(1)	1.75(10)	7.92(74)	1.851	0.115(1)	1.86(12)	6.92(64)
	1.851	0.3487	0.174(1)	1.14(10)	5.73(57)	2.116	0.197(1)	1.06(17)	6.07(71)
	2.116	0.2860	0.309(1)	0.65(4)	3.86(25)	2.380	0.345(1)	0.62(4)	3.88(68)
$\mu^{*2} = 3$	1.689	0.3976	0.096(1)	1.77(10)	8.9(12)	1.971	0.115(1)	1.76(10)	8.3(10)
	1.971	0.3463	0.177(1)	1.15(8)	5.27(53)	2.253	0.204(1)	1.04(8)	4.96(75)
	2.252	0.2793	0.330(2)	0.61(4)	3.89(24)	2.534	0.369(2)	0.56(5)	3.44(17)
$\mu^{*2} = 6$	1.810	0.4041	0.087(1)	1.88(12)	8.64(54)	2.112	0.105(1)	2.16(20)	6.7(15)
	2.112	0.3524	0.164(1)	1.34(10)	6.56(32)	2.413	0.192(1)	1.15(10)	5.48(49)
	2.414	0.2860	0.312(2)	0.56(4)	4.09(40)	2.715	0.354(2)	0.69(9)	4.33(28)
$\mu^{*2} = 9$	1.962	0.4101	0.0780(5)	2.53(16)	7.29(14)	2.288	0.097(1)	2.40(15)	9.3(10)
	2.288	0.3576	0.157(1)	1.44(10)	7.26(32)	2.615	0.184(1)	1.24(5)	6.38(78)
	2.615	0.2900	0.305(1)	0.75(8)	4.66(14)	2.942	0.346(2)	0.87(5)	4.90(63)
$\mu^{*2} = 12$	2.134	0.4163	0.0730(5)	2.64(20)	9.7(12)	2.490	0.092(1)	2.63(26)	7.0(15)
	2.490	0.3625	0.152(1)	1.46(10)	7.59(72)	2.846	0.179(1)	1.40(9)	5.49(83)
	2.846	0.2923	0.306(1)	0.78(6)	4.13(40)	3.202	0.347(2)	0.86(6)	4.47(25)

Literature

[1] Alder B.J., Wainwright T.E., Velocity autocorrelations for hard spheres, Phys. Rev. Lett. **18** (1967) 988-990.

[2] Alder B.J., Wainwright T.E., Decay of velocity autocorrelation function, Phys. Rev. A. **1** (1970) 18-21.

[3] Alder B.J., Gass D.M., and Wainwright T.E., Studies in molecular dynamics VIII. The transport coefficients of hard-sphere fluid, J. Chem. Phys. **53** (1970) 3813-3825.

[4] Alder B.J., in Ciccotti G., and Hoover W.G. (Ed.), Molecular dynamic simulation of statistical mechanical systems, North-Holland, Amsterdam, 1986.

[5] Allen M.P., Tildesley D.J., Computer simulation of liquids, Clarendon Press, Oxford, 1987.

[6] Andersen H.C., Molecular dynamics simulations at constant pressure and or temperature, J. Chem. Phys. **72** (1980) 2384-2393.

[7] Arends B., Prins K.O., and Trappeniers N.J., Self-diffusion in gaseous and liquid ethylene, Physica A **107** (1981) 307-318.

[8] Arya G., Chang H.C., and Maginn E.J., A critical comparison of equilibrium, nonequilibrium and boundary driven molecular dynamics techniques for studying transport in microporous materials, J. Chem. Phys. **115** (2001) 8112-8124.

[9] Ashurst W.T., Hoover W.G., Dense fluid shear viscosity via nonequilibrium molecular dynamics, Phys. Rev. A **11** (1975) 658-678.

[10] Baranyai A., Cummings P.T., Nonequilibrium molecular dynamics study of shear and shear-free flows in simple fluids, J. Chem. Phys. **103** (1995) 10217-10225.

[11] Barker J.A., Watts R.O., Monte Carlo studies of dielectric properties of water-like model, Mol. Phys. **26** (1973) 789-792.

[12] Baron A.F.M., The dynamic liquid state, Longman, London, 1974.

[13] Bewilogua L., Gladun C., and Kubsch B., The coefficient of diffusion of liquid neon, J. Low Temp. Phys. **4** (1971) 299-303.

[14] Bi K.D., Chen Y.F., Yang J.K., Wang Y.J., and Chen M.H., Molecular dynamics simulation of thermal conductivity of single wall carbon nanotubes, Phys. Lett. A **350** (2006) 150-153.

[15] Brennan J.K., Turner C.H., Rice B.M., and Gubbins K.E., Chemical reactions in highly nonideal enviroments: reactive Monte Carlo simulations, AIP Conf. Proc. **690** (2003) 374-375.

[16] Borgelt P., Hoheisel C., and Stell G., Exact molecular dynamics and kinetic theory results for thermal transport coefficients of the Lennard-Jones argon fluid in a wide region of states, Phys. Rev. A **42** (1990) 789-794.

[17] Borzsak I., Cummings P.T., and Evans D.J., Shear viscosity of a simple fluid over a wide range of strain rates, Mol. Phys. **100** (2002) 2735-2738.

[18] Caldwell C.S., Babb A.L., Diffusion in ideal binary liquid mixtures, J. Phys. Chem. **60** (1956) 51-56.

[19] Canales M., Padro J.A., Dynamic properties of Lennard-Jones fluids and liquid metals, Phys. Rev. E **60** (1999) 551-558.

[20] Carnahan B., Luther H.A., and Wilkes J.O., Applied numerical methods, John Wiley & Sons, New York, 1969.

[21] Chacin A., Vazquez J.M., and Müller E.A., Molecular simulation of the Joule-Thomson inversion curve of carbon dioxide, Fluid Phase Equilib. **165** (1999) 147-155.

[22] Chen S.H., Rahman A., Molecular dynamics simulation of dense gases .1. Test particle motion, Mol. Phys. **34** (1977) 1247-1262.

[23] Cheung P.S.Y., Powles J.G., Properties of liquid nitrogen 4. Computer simulation, Mol. Phys. **30** (1975) 921-949.

[24] Chialvo A.A., Cummings H.D., Cochran, H.D., Simonson J.M., and Mesmer R.E., Na^+-Cl^- ion pair association in supercritical water, J. Chem. Phys. **103** (1995) 9379-9387.

[25] Ciccotti G., Jacucci G., and McDonald I.R., Transport properties of molten alkali halides, Phys. Rev. A **13** (1976) 426-436.

[26] Ciccotti G., Jacucci G., and McDonald I.R., "Thought experiments" by molecular dynamics, J. Stat. Phys. **21** (1979) 1-22.

[27] Codastefano P., Ricci M.A., and Zanza V., Behavior of self-diffusion coefficient of Kr at low densities, Physica A **92** (1978) 315-322.

[28] Coelho L.A.F., de Oliveira J.V., Tavares F.W., and Matthews M.A., Role of attractive forces in self-diffusion and mutual diffusion in dense simple fluids and real substances, *Fluid Phase Equilib.* **194** (2002) 1131-1140.

[29] Colina C.M., Olivera-Fuentes C.G., Siperstein F.R., Lisal M., and Gubbins K.E., Thermal properties of supercritical carbon dioxide by Monte Carlo simulations, Mol. Simul. **29** (2003) 405-412.

[30] Colina C.M., Lisal M., Siperstein F.R., and Gubbins K.E., Thermal properties of supercritical carbon dioxide by Monte Carlo simulations, Fluid Phase Equilib. **202** (2002) 253-262.

[31] Cook G.A., Argon, helium and the rare gases, Vol. I, Interscience Publishers, New York, 1961.

[32] Cowan J.A., Ball R.N., Temperature dependence of bulk viscosity in liquid argon, Can. J. Phys. **50** (1972) 1881-1886.

[33] Cowan J.A., Leech J.W., Ultrasonic attenuation and bulk viscosity of liquid xenon, Can. J. Phys. **59** (1981) 1280-1288.

[34] Cui S., Harris J.G., Ion association and liquid structure in supercritical water solution of sodium chloride: A microscopic view from molecular dynamic simulation, Chem. Eng. Sci. **49** (1994) 2749-2763.

[35] Cui S.T., Cummings P.T., and Cochran H.D., Multiple time step nonequilibrium molecular dynamics simulation of the rheological properties of liquid n-decane, J. Chem. Phys. **104** (1996) 255-262.

[36] Cui S.T., Cummings P.T., and Cochran H.D., *The calculation of viscosity of* liquid n-decane and n-hexadecane by the Green-Kubo method, Mol. Phys. **93** (1998) 117-121.

[37] Cummings P.T., Wang B.Y., Evans D.J., and Fraser K.J., Nonequilibrium molecular dynamics calculation of self-diffusion in a non-Newtonian fluid subject to a couette strain field, J. Chem. Phys. **94** (1991) 2149-2158.

[38] Cummings P.T., Evans D.J., Nonequilibrium molecular dynamics approaches to transport properties and non-newtonian fluid rheology, Ind. Eng. Chem. Res. **31** (1992) 1237-1252.

[39] Cussler E.L., Diffusion mass transfer in fluid systems, Cambridge University Press, Cambridge, 1997.

[40] Daivis P.J., and Evans D.J., Nonequilibrium molecular dynamics calculation of thermal conductivity of flexible molecules butane, Mol. Phys. **81** (1994) 1289-1295.

[41] Daivis P.J., and Evans D.J., Transport coefficients of liquid butane near the boiling point by equilibrium molecular dynamics, J. Chem. Phys. **103** (1995) 4261-4265.

[42] Darken L.S., Diffusion, mobility and their interrelation through free energy in binary metallic systems, Trans. Am. inst. Mining. Met. Eng. **175** (1948) 184-201.

[43] Daubert T.E., Daner R.P., Data compilation tables of properties of pure subtances AIChE, American Chemical Society, New York, 1985.

[44] De Groot S.R., Mazur P., Nonequilibrium thermodynamics, Dover, New York, 1984.

[45] Dubey G.S., Oshea S.F., and Monson P.A., Vapor-liquid equilibria for two center Lennard-Jones diatomics and dipolar diatomics, Mol. Phys. **80** (1993) 997-1007.

[46] Dullien F.A.L., Statistical test of vignes correlation of liquid phase diffusion coefficients, Ind. Eng. Chem. Fundam. **10** (1971) 41-49.

[47] Dymond J.H., Corrected Enskog theory and transport coefficients of liquids, J. Chem. Phys. **60** (1974) 969-979.

[48] Dymond J.H., Hard sphere theories of transport properties, Chem. Soc. Rev. **14** (1985) 317-356.

[49] Enders S., Kahl H., Mecke M., and Winkelmann J., Molecular dynamics simulation of the liquid-vapor interface: I. The orientational profile of two-center Lennard-Jones and of Stockmayer fluid molecules, J. Mol. Liq. **115** (2004) 29-39.

[50] Chapman S., Cowling T.G., The mathematical theory of nonuniform gases, Cambridge University Press, Cambridge, 1970.

[51] Erpenbeck J.J, Wood W.W., Molecular dynamics calculations of shear viscosity time correlation functions for hard spheres, J. Stat. Phys. **24** (1981) 455-468.

[52] Erpenbeck J.J., Comparison of Green-Kubo and nonequilibrium calculations of the self-diffusion constant of a Lennard-Jones fluid, Phys. Rev. A. **35** (1987) 218-232.

[53] Erpenbeck J.J., Shear viscosity of the Lennard-Jones fluid near the triple point Green-Kubo results, Phys. Rev. A. **38** (1988) 6255-6266.

[54] Etesse P.E., Zega J.A., and Kobayashi R., High-pressure nuclear magnetic resonance measurement of spin lattice relaxation and self-diffusion in carbon dioxide, J. Chem. Phys. **97** (1992) 2022-2029.

[55] Evans D.J., Streett W.B., Transport properties of homonuclear diatomic II. Dense fluids, Mol. Phys. **36** (1978) 161-176.

[56] Evans D.J., Rheological properties of simple fluids by computer simulation, Phys. Rev. A **23** (1981) 1988-1997.

[57] Evans D.J., Homogeneus NEMD algorithm for thermal conductivity. Aplication of noncanonical response theory, Phys. Lett. A **91** (1982) 457-460.

[58] Evans D.J., Morriss G.P., Nonequilibrium molecular dynamics, Comp. Phys. Rep. **1** (1984) 297-343.

[59] Evans D.J., Thermal conductivity of the Lennard-Jones fluid, Phys. Rev. A **34** (1986) 1449-1453.

[60] Evans D.J., Murad S., Thermal conductivity in molecular fluids, Mol. Phys. **68** (1989) 1219-1223.

[61] Evans D.J., Morriss G.P., and Hood L.M., On the number dependence of viscosity in 3 dimensional fluids, Mol. Phys. **68** (1989) 637-646.

[62] Evans D.J, Morriss G.P., Statistical mechanics of nonequilibrium liquids. Theoretical chemistry monograph series, Academic Press, London, 1990.

[63] Evers C., Lösch H.W., and Wagner W., An absolute viscometer densimeter and measurements of the viscosity of nitrogen, methane, helium, neon, argon, and krypton over a wide range of density and temperature, Int. J. Thermophys. **23** (2002) 1411-1439.

[64] Ferguson N., Day R., Johnson C.M., Allen M.D., Daggett V., and Fersht A.L., Simulation and experiment at high temperatures: Ultrafast folding of a thermophilic protein by nucleation-condensation, J. Mol. Biol. **347** (2005) 855-870.

[65] Fernández G.A., Vrabec J., and Hasse H., Self-diffusion and binary Maxwell-Stefan diffusion in simple fluids with the Green-Kubo method, Int. J. Thermophys. **25** (2004) 175-186.

[66] Fernández G.A., Vrabec J., and Hasse H., A molecular simulation study of shear and bulk viscosity and thermal conductivity of simple real fluids, Fluid Phase Equilib. **221** (2004) 157-163.

[67] Fernández, G.A., Vrabec, J., and Hasse H., Self-diffusion and binary Maxwell-Stefan diffusion coefficients of quadrupolar real fluids from molecular simulation, Int. J. Thermophys. **26** (2005) 1389-1407.

[68] Fernández G.A., Vrabec J., and Hasse H., Shear viscosity and thermal conductivity of quadrupolar real fluids from molecular simulation, Mol. Simul. **31** (2005) 787-793.

[69] Fernández G.A., Vrabec J., and Hasse H., Shear viscosity and thermal conductivity of dipolar real fluids from molecular dynamics simulation, Cryogenics in press.

[70] Fincham D., Quirke N., and Tildesley D.J., Computer simulation of molecular liquid mixtures 1. A diatomic Lennard-Jones model mixture for CO_2/C_2H_6, J. Chem. Phys. **84** (1986) 4535-4546.

[71] Ferrario M., Ciccotti G., Holian B.L., and Ryckaert J.P., Shear rate dependence of the viscosity of the Lennard-Jones liquid at the triple point, Phys. Rev. A **44** (1991) 6936-6939.

[72] Firouzi M., Tsotsis T.T., and Sahimi M., Nonequilibrium molecular dynamics simulations of transport and separation of supercritical fluid mixtures in

nanoporous membranes I. Results for a single carbon nanopore, J. Chem. Phys. **119** (2003) 6810-6822.

[73] Firouzi M., Nezhad K.M., Tsotsis T.T., and Sahimi M., Molecular dynamics simulations of transport and separation of carbon dioxide-alkane mixtures in carbon nanopores, J. Chem. Phys. **120** (2004) 8172-8185.

[74] Case F., Chaka A., Friend D.G., Frurip D., Golab J., Russel J., Moore J., Mountain R.D., Olson J., Schiller M., and Store J., The first industrial fluid properties simulation challenge, Fluid Phase Equilib. **217** (2004) 1-10.

[75] Ford D.M., Heffelfinger G.S., Massively parallel dual control volume grand canonical molecular dynamics with LADERA II. Gradient driven diffusion through polymers, Mol. Phys. **94** (1998) 673-683.

[76] Fotouh K., Shukla K., Effect of quadrupole moment on excess properties of binary 2CLJQ mixtures from molecular dynamics simulation: Model and real mixtures, Fluid Phase Equilib. **135** (1997) 35-50.

[77] Frenkel D., Smit R., Understanding molecular simulation, Academic Press, San Diego, 1996.

[78] Furtado P.M., Mazenko G.F., and Yip S., Kinetic model description of dense hard sphere fluids, Phys. Rev. A **13** (1976) 1641-1644.

[79] Furukawa S., Nitta T., Nonequilibrium molecular dynamics simulation studies on gas permeation across carbon membranes with different pore shape composed of micrographite crystallites, J. Membr. Sci. **178** (2000) 107-119.

[80] Furukawa S., Nitta T., A new algorithm of boundary-driven type nonequilibrium molecular dynamics for simulating membrane permeation of gas mixtures, J. Chem. Eng. Jpn. **38** (2005) 278-282.

[81] Galamba N., Nieto de Castro C.A., and Ely J.F., Shear viscosity of molten alkali halides from equilibrium and nonequilibrium molecular dynamics simulations, J. Chem. Phys. **122** (2005) 224501.

[82] Gao J.L., Simulation of the Na^+Cl^- ion pair in supercritical wather, J. Phys. Chem. **98** (1994) 6049-6053.

[83] Gardner P.J., Heyes D.M., and Preston S.R., Molecular dynamics computer simulations of binary Lennard-Jones fluid mixtures. Thermodynamics of mixing and transport coefficients, Mol. Phys. **73** (1991) 141-173.

[84] Gillan M.J., Dixon M., The calculation of thermal conductivities by perturbed molecular dynamics simulation, J. Phys. C. Solid State Phys. **16** (1983) 869-878.

[85] Gosling E.M., McDonald I.R., and Singer K., On the calculation by molecular dynamics of sher viscosity of a simple fluids, Mol. Phys. **26** (1983) 1475-1484.

[86] Graves R.E., Bulk viscosity: Past to present, J. Thermophysics Heat Transf. **13** (1999) 337-342.

[87] Gray C.G., Gubbins K.E., Theory of molecular fluids Vol. 1. fundamentals, Clarendon Press, Oxford, 1984.

[88] Green M.S., Markoff random processes and the statistical mechanics of time-dependent phenomena 1, J. Chem. Phys. **20** (1952) 1281-1295.

[89] Green M.S., Markoff random processes and the statistical mechanics of time dependent phenomena 2. Irreversible processes in fluids, J. Chem. Phys. **22** (1954) 398-413.

[90] Greiner-Schmid A., Wappmann S., Has M., and Lüdemann H.D., Self-diffusion in the compressed fluid lower alkanes methane, ethane, and propane, J. Chem. Phys. **94** (1991) 5643-5649.

[91] Gubbins K.E., in Singer K. (Ed.), Statistical mechanics vol. 1, The Chemical Society, Burlington House, London, 1972.

[92] Haile J.M., Molecular dynamics simulation, John Wiley & Sons Inc., Ne York, 1997.

[93] Hammonds K.D., Heyes D.M., Transport coefficients of model simple liquids a molecular dynamics study and effective hard-sphere analysis, J. Chem. Soc. Faraday Trans. 2, **84** (1988) 705-725.

[94] Hanley H.J.M., Transport phenomena in fluids, Marcel Dekker, New York and London, 1969.

[95] Hansen J.P., MacDonald I.R., Theory of simple liquids, Elsevier, 2rd Ed. London, 1990.

[96] Harris K.R., Density dependence of self-diffusion coefficient of methane at 50 degrees C, 25 degrees C and 50 degrees C, Physica A **94** (1978) 448-464.

[97] Haynes W.M., Mesurement of the viscosity of compressed and gaseous and liquid fluorine, Physica **76** (1974) 1-20.

[98] Heyes D.M., Kim J.J., Montrose C.J., and Litovitz T.A., Time dependent nonlinear shear stress effects in simple liquids. A molecular dynamics study, J. Chem. Phys. **73** (1980) 3987-3996.

[99] Heyes D.M., Self-diffusion and shear viscosity of simple fluids. A molecular dynamics study, J. Chem. Soc. Faraday Trans. II **79** (1983) 1741-1758.

[100] Heyes D.M., Thermal conductivity and bulk viscosity of simple fluids a molecular dynamics study, J. Chem. Soc. Faraday Trans. II **80** (1984) 1363-1394.

[101] Heyes D.M., Transport coefficients of the Lennard-Jones fluid by molecular dynamics, Can. J. Phys. **64** (1986) 773-781.

[102] Heyes D.M., Viscosity and self-diffusion of simple liquids. Hard-sphere treatment of molecular dynamics data, J. Chem. Soc. Faraday Trans. II **83** (1987) 1985-2009.

[103] Heyes D.M., Transport coefficients of Lennard-Jones fluids. A molecular dynamics and effective hard sphere treatment, Phys. Rev. B **37** (1988) 5677-5696.

[104] Heyes D.M., Powles J.G., Information theory applied to the transport coefficients of Lennard-Jones fluids, Mol. Phys. **71** (1990) 781-800.

[105] Heyes D.M., Preston S.R., Transport coefficients of Ar+Kr mixtures by molecular dynamics computer simulation, Phys. Chem. Liq. **23** (1991) 123-149.

[106] Heyes D.M., Molecular dynamics simulations of liquid binary mixtures partial properties of mixing and transport coefficients, J. Chem. Phys. **96** (1992) 2217-2227.

[107] Heyes D.M., Powles J.G., and Montero J.C.G., Information theory applied to the transport coefficients of Lennard-Jones fluids 2, Mol. Phys. **78** (1993) 229-234.

[108] Heyes D.M., Transport coefficients of simple fluids with steeply repulsive potentials, J. Phys. Condes. Matter. **6** (1994) 6409-6421.

[109] Heyes D.M., The Liquid State. Applications of molecular simulation, John Wiley & Sons, New York, 1998.

[110] Hill J.R., Minihan A.R., Wimmer E., and Adams C.J., Framework dynamics including computer simulations of the water adsorption isotherm of zeolite Na-MAP, Phys. Chem. Chem. Phys. **2** (2000) 4255-4264.

[111] Hirschfelder J.O., Curtiss C.F., and Bird R.B., Molecular theory of gases and liquids, John Wiley & Sons, New York, 1954.

[112] Hoheisel C., Ne/Xe at very high pressures a molecular dynamics study using Lennard-Jones (12-6) potentials, Mol. Phys. **62** (1987) 239-249.

[113] Hoheisel C., Transport coefficients of dense fluids composed of globular molecules equilibrium molecular dynamics investigations using more center Lennard-Jones potentials, J. Chem. Phys. **89** (1988) 3195-3202.

[114] Hoheisel C., Luo H., Transport coefficients of liquid N_2 computed by molecular dynamics, Nuovo Cimento Soc. Ital. Fis. D-Condens. Matter At. Mol. Chem. Phys. Fluids Plasmas Biophys. **12** (1990) 499-509.

[115] Hoheisel C., Transport properties of molecular liquids, Phys. Rep. **245** (1994) 111-157.

[116] Holian B.L., Evans D.J., Shear viscosities away from the melting line a comparison of equilibrium and nonequilibrium molecular dynamics, J. Chem. Phys. **78** (1983) 5147-5150.

[117] Hoover W.G., Evans D.J., Hickman R.B., Ashurst W.T., and Moran B., Lennard-Jones triple point bulk and shear viscosities Green-Kubo theory, hamiltonian mechanics, and nonequilibrium molecular dynamics, Phys. Rev. A **22** (1980) 1690-1697.

[118] Jaccuci G., Mcdonald I.R., Structure and diffusion in mixtures of rare-gas liquids, Physica A **80** (1975) 607-625.

[119] Jiang S.Y., Molecular simulation studies of self-assembled monolayers of alkanethiols on Au(111), Mol. Phys. **100** (2002) 2261-2275.

[120] Jolly D., Bearman R., Molecular dynamics simulation of the mutual and self-diffusion coefficients in Lennard-Jones liquid-mixtures, Mol. Phys. **41** (1980) 137-147.

[121] Karim S.M., The 2nd coefficient of viscosity of liquids and gases, Rev. Mod. Phys. **24** (1952) 108-116.

[122] Keffer D.J., Adhangale P., The composition dependence of self and transport diffusivities from molecular dynamics simulations, Chem. Eng. J. **100** (2004) 51-69.

[123] Keffer D.J., Edwards B.J., and Adhangale P., Determination of statistically reliable transport diffusivities from molecular dynamics simulation, J. Non-Newton. Fluid Mech. **120** (2004) 41-53.

[124] Kesting J., Wakeham W.A., Transport properties of fluids: Thermal conductivity, viscosity and diffusion coefficient, CINDAS data series in material properties, Hemisphere Publishing, New York, 1988.

[125] Keyes T., Masters A.J., Tagged particle motion in dense media dynamics beyond the Boltzmann equation, Adv. Chem. Phys. **58** (1985) 1-53.

[126] Kinjo T., Ohguchi K., Yasuoka K., and Matsumoto M., Computer simulation of phase change: Vapor nucleation and bubble formation dynamics, Comput. Mater. Sci. **14** (1999) 138-141.

[127] Kincaid J.M., Tuo R.F., and Deharo M.L., A test of the modified Enskog theory for self-diffusion, Mol. Phys. **81** (1994) 837-850.

[128] Kohler F., Van Nhu N., The 2nd virial coefficients of some halogenated ethanes, Mol. Phys. **80** (1993) 795-800.

[129] Kriebel C., Müller A., Winkelmann J., and Fischer J., Excess properties of dipolar and nonpolar fluid mixtures from NpT molecular dynamics simulations, Mol. Phys. **87** (1996) 151-157.

[130] Kriebel C., Mecke M., Winkelmann J., Vrabec J., and Fischer J., An equation of state for dipolar two-center Lennard-Jones molecules and its application to refrigerants, Fluid Phase Equilib. **142** (1998) 15-32.

[131] Taylor R., Krishna R., Multicomponent mass transfer, John Wiley & Sons, New York, 1993.

[132] Krynicki K., Rahkamaa E.J., and Powles J.P., Properties of liquid nitrogen 1. Self-diffusion coefficient, Mol. Phys. **28** (1974) 853-855.

[133] Kubo R., Yokota M., and Nakajima S., Statistical mechanical theory of irreversible processes 1. General theory and simple applications to magnetic and conduction problems, J. Phys. Soc. Jap. **12** (1957) 570-586.

[134] Kubo R., Some aspects of the statistical mechanical theory of irreversible processes, Lectures in theoretical physics **1** (1958) 120-188.

[135] Kubo R., Fluctuation dissipation theorem, Rpts. Progr. Phys. **29** (1966) 255-284.

[136] Ladd A.J.C., Equation of motion for nonequilibrium molecular dynamics simulation of viscous flow in molecular fluids, Mol. Phys. **53** (1984) 459-463.

[137] Lagache M.H., Ungerer Ph., and Boutin A., Prediction of thermodynamic derivative properties of natural condensate gases at high pressure by Monte Carlo simulation, Fluid Phase Equilib. **220** (2004) 211-223.

[138] Lees A.W., Edwards S.F., The computer study of transport processes under extreme conditions, J. Phys. C. Solid State **5** (1972) 1921-1929.

[139] Lee S.H., Cummings P.T., Shear viscosity of model mixtures by nonequilibrium molecular dynamics 1. Argon+krypton mixtures, J. Chem. Phys. **99** (1993) 3919-3925.

[140] Lee S.H., Cummings P.T., Shear viscosity of model mixtures by nonequilibrium molecular dynamics 2. Effect of dipolar interactions, J. Chem. Phys. **105** (1996) 2044-2055.

[141] Lee S.H., Cummings P.T., Shear viscosity of model mixtures by nonequilibrium molecular dynamics III. Effect of quadrupolar interactions, Mol. Simul. **27** (2001) 115-137.

[142] Lee S.H., Cummings P.T., Shear viscosity of model mixtures by nonequilibrium molecular dynamics IV. Effect of molecular shape, Mol. Simul. **27** (2001) 139-155.

[143] Lee J.C., Mutual diffusion in a liquid mixture of argon and krypton, Physica A **247** (1997) 140-152.

[144] Lee S.H., Moon G.K., and Choi S.G., Nonequilibrium molecular dynamics simulations of thermal transport coefficients of liquid water, Bull. Korean Chem. Soc. **12** (1991) 315-322.

[145] Lee S.H., Park D.K., and Kang D.B., Molecular dynamics simulations for transport coefficients of liquid argon: New approaches, Bull. Korean Chem. Soc. **24** (2003) 178-182.

[146] Lemmon E.W., McLinden M.O., and Huber M.L., REFPROP, NIST Standard reference database 23, Version 7.0, 2002.

[147] Levesque D., Verlet L., Computer "experiments" on classical fluids III. Time dependent self correlation functions, Phys. Rev. A **2** (1970) 2514-2528.

[148] Levesque D., Verlet L., and Kürkijarvi J., Computer experiment on classical fluids. IV. Transport properties and time-correlation fucntions of the Lennard-Jones liquid near its triple point, Physical Review A **7** (1973) 1690-1700.

[149] Levesque D., Verlet L., Molecular dynamics calculations of transport coefficients, Mol. Phys. **61** (1987) 143-159.

[150] Liem S.Y., Brown D., and Clarke J.H.R., Investigation of the homogeneous shear nonequilibrium molecular dynamics method, Phys. Rev. A **45** (1992) 3706-3713.

[151] Lin W., Yang Q.Y., and Zhong C.L., Molecular simulation of vapor-liquid equilibria of toxic gases, Fluid Phase Equilib. **220** (2004) 1-6.

[152] Lísal M., Budinský R., Vacek V., and Aim K., Vapor-liquid equilibria of alternative refrigerants by molecular dynamics simulations, Int. J. Thermophys. **20** (1999) 163-174.

[153] Liu H., Silva C.M., and Macedo E.A., Unified approach to the self-diffusion coefficients of dense fluids over wide ranges of temperature and pressure. Hard-sphere, square-well, Lennard-Jones and real substances, Chem. Eng. Sci. **53** (1998) 2403-2422.

[154] Lombardero M., Martin C., Lomba E., and Fernandez A., On the thermodynamics of quadrupolar two-center Lennard-Jones fluids, Fluid Phase Equilib. **74** (1992) 95-108.

[155] Luo H., Hoheisel C., Collective transport in a molecular liquid with quadrupole interaction, Phys. Rev. A. **43** (1991) 1819-1825.

[156] Lustig R., Angle average for the powers of the distance between 2 separated vectors, Mol. Phys. **65** (1988) 175-179.

[157] MacDowell L.G., Garzon B., Calero S., and Lago S., Dynamical properties and transport coefficients of Kihara linear fluids, J. Chem. Phys. **106** (1997) 4753-4767.

[158] MacDowell L.G., Menduina C., Vega C., and de Miguel E., Third virial coefficients and critical properties of quadrupolar two center Lennard-Jones models, Phys. Chem. Chem. Phys. **5** (2003) 2851-2857.

[159] Macedo P.B., Litovitz T.A., On relative roles of free volume and activation energy in viscosity of liquids, J. Chem. Phys. **42** (1965) 245-256.

[160] Macelroy J.M.D., Nonequilibrium molecular dynamics simulation of diffusion and flow in thin microporous membranes, J. Chem. Phys. **101** (1994) 5274-5280.

[161] MacElroy J.M.D., Boyle M.J., Nonequilibrium molecular dynamics simulation of a model carbon membrane separation of CH_4-H_2 mixtures, Chem. Eng. J. **74** (1999) 85-97.

[162] MacElroy J.M.D., Computer simulation of diffusion within and through membranes using nonequilibrium molecular dynamics, Korean J. Chem. Eng. **17** (2000) 129-142.

[163] MacGowan D., Evans D.J., Heat and matter trannsport in binary liquid mixtures, Phys. Rev. A **34** (1986) 2133-2142.

[164] Maddox M.W., Gubbins K.E., A molecular simulation study of freezing/melting phenomena in Lennard-Jones methane in cylindrical nano scale pores, J. Chem. Phys. **107** (1999) 9659-9667.

[165] Malbrunot P., Boyer A., and Charles E., Experimental bulk viscosities of argon, krypton, and xenon near their triple point, Phys. Rev. A **27** (1983) 1523-1534.

[166] Marcelli G., Todd B.D., and Sadus R.J., The strain rate dependence of shear viscosity, pressure and energy from two body and three body interactions, Fluid Phase Equilib. **183** (2001) 371-379.

[167] Maruyama S., A molecular dynamics simulation of heat conduction of a finite length single walled carbon nanotube, Microscale Thermophys. Eng. **7** (2003) 41-50.

[168] Matsumoto M., Molecular dynamics of fluid phase change, Fluid Phase Equilib. **144** (1998) 307-314.

[169] McDonald I.R., Singer K., Equation of state for simple liquids, Mol. Phys. **23** (1972) 29-40.

[170] McQuarri D.A., Statistical mechanics, Harper and Row, New York, (1976).

[171] Mecke M., Fischer J., and Winkelmann J., Molecular dynamics simulation of the liquid-vapor interface of dipolar fluids under different electrostatic boundary conditions, J. Chem. Phys. **114** (2001) 5842-5852.

[172] Meier K., Laesecke A., and Kabelac S., A molecular dynamics simulation study of the self-diffusion coefficient and viscosity of the Lennard-Jones fluid, Int. J. Thermophys. **22** (2001) 161-173.

[173] Meier K., PhD Thesis, Computer simulation and interpretation of the transport coefficients of the Lennard-Jones model fluid, Shaker Publishers, Aachen, 2002.

[174] Meier K., Laesecke A., and Kabelac S., Transport coefficients of the Lennard-Jones model fluid. II Self-diffusion, J. Chem. Phys. **121** (2004) 9526-9535.

[175] Meier K., Laesecke A., and Kabelac S., Transport coefficients of the Lennard-Jones model fluid I. Viscosity, J. Chem. Phys. **121** (2004) 3671-3687.

[176] Michels J.P.J., Trappeniers N.J., Molecular dynamical calculations of self-diffusion coefficient below critical density, Chem. Phys. Lett. **33** (1975) 195-200.

[177] Michels J.P.J., Trappeniers N.J., Self-diffusion coefficient in gas phase at moderate densities, obtained by computer simulations, Physica A **90** (1978) 179-195.

[178] Michels J.P.J, Trappeniers N.J., Molecular dynamical calculations on the viscosity of a square well fluid, Chem. Phys. Lett. **66** (1979) 20-23.

[179] Michels J.P.J., Trappeniers N.J., Molecular dynamical calculations of the transport properties of a square well fluid 1. The viscosity below critical density, Physica A **101** (1980) 156-166.

[180] Michels J.P.J., Trappeniers N.J., Molecular dynamical calculations on the transport properties of a square well fluid 2. The viscosity above the critical density, Physica A **104** (1980) 243-254.

[181] Michels J.P.J., Trappeniers N.J., Molecular dynamical calculations on the transport properties of a square well fluid 3. The thermal conductivity, Physica A **107** (1981) 158-165.

[182] Michels J.P.J., Trappeniers N.J., Molecular dynamical calculations on the transport properties of a square well fluid 4. The influence of the well width on the viscosity and the thermal conductivity, Physica A **107** (1981) 299-306.

[183] Michels J.P.J., Trappeniers N.J., Molecular dynamical calculations of the transport properties of a square well fluid 5. The coefficient of self-diffusion, Physica A **116** (1982) 516-525.

[184] Michels J.P.J., Trappeniers N.J., Molecular dynamical calculations of the viscosity of Lennard-Jones systems, Physica A **133** (1985) 281-290.

[185] Mifflin T.R., Bennett C.O., Self-diffusion in argon to 300 atmospheres, J. Chem. Phys. **29** (1958) 975-978.

[186] Mikhailenko S.A., Dudar V.G., Derkach V.N., and Zozulya V.N., Volume and shear viscosity of liquid argon+krypton mixtures, Sov. J. Low. Temp. Phys. **3** (1977) 331-336.

[187] Mikhailenko S.A., Dudar V.G., and Derkach V.N., Viscoelastic properties and acoustic relaxation in liquids, Sov. J. Low. Temp. Phys. **4** (1978) 205-212.

[188] Mills R., Malhotra R., Woolf L.A., and Miller D.G., Distinct diffusion coefficients in binary nonelectrolyte mixtures frames of reference, J. Phys. Chem. **98** (1994) 5565-5575.

[189] McCabe C., Cui S.T., Cummings P.T., Gordon P.A., and Saeger R.B., Examining the rheology of 9-octylheptadecane to giga-pascal pressures, J. Chem. Phys. **114** (2001) 1887-1891.

[190] McCabe C., Manke C.W., and Cummings P.T., Predicting the Newtonian viscosity of complex fluids from high strain rate molecular simulations, J. Chem. Phys. **116** (2002) 3339-3342.

[191] Möller D., Fischer J., Determination of an effective intermolecular potential for carbon dioxide using vapor liquid phase equilibria from NpT plus test particle simulations, Fluid Phase Equilib. **100** (1994) 35-61.

[192] Moon C.B., Moon G.K., and Lee S.H., Equilibrium and nonequilibrium molecular dynamics simulations of thermal transport coefficients of liquid argon, Bull. Korean Chem. Soc. **12** (1991) 309-315.

[193] Moreland J.F., Freund J.B., and Chen G., The disparate thermal conductivity of carbon nanotubes and diamond nanowires studied by atomistic simulation, Microscale Thermophys. Eng. **8** (2004) 61-69.

[194] Müller-Plathe F., A simple nonequilibrium molecular dynamics method for calculating the thermal conductivity, J. Chem. Phys. **106** (1997) 6082-6085.

[195] Müller A., Winkelmann J., and Fischer J., Effect of molecular elongation on the dipolar Free-energy, J. Chem. Phys. **99** (1993) 3946-3949.

[196] Murad S., Singh D.P., Hanley H.J.M., and Evans D.J., Thermal conductivity of a model diatomic fluid, Mol. Phys. **72** (1991) 487-490.

[197] Murad S., Lin J., Molecular modeling of fluid separations using membranes: Effect of molecular forces on mass transfer rates, Chem. Eng. J. **74** (1999) 99-108.

[198] Nasrabad A.E., Laghaei R., and Eu B.C. Modified free volume theory of self-diffusion and molecular theory of shear viscosity of liquid carbon dioxide, J. Chem. Phys. B **109** (2005) 8171-8179.

[199] Neumann M., Steinhauser O., Influence of boundary-conditions used in machine simulations on the structure of polar systems, Mol. Phys. **39** (1980) 437-454.

[200] Newsome D.A., Sholl D.S., Predictive assessment of surface resistances in zeolite membranes using atomically detailed models, J. Phys. Chem. B **109** (2005) 7237-7244.

[201] Nieto-Draghi C., Avalos J.B., and Rousseau B., Computing the Soret coefficient in aqueous mixtures using boundary driven nonequilibrium molecular dynamics, J. Chem. Phys. **122** (2005) 114503.

[202] NIST Chemistry WebBook, http://webbook.nist.gov/chemistry.

[203] Nosé S., A molecular dynamics method for simulations in the canonical ensemble, Mol. Phys. **100** (2002) 191-198.

[204] O'Reilly D.E., Peterson E.M., Hogenboom D.I., and Scheie C.E., F-19 Nuclear magnetic resonance of liquid and solid phases of fluorine, J. Chem. Phys. **54** (1971) 4194-4199.

[205] Osman M.A., Srivastava D., Temperature dependence of the thermal conductivity of single wall carbon nanotubes, Nanotechnology **12** (2001) 21-24.

[206] Palmer B.J., Calculation of thermal diffusion coefficients from plane wave fluctuations in the heat energy density, Phys. Rev. E **49** (1994) 2049-2057.

[207] Pas M.F., Zwolinski B., Computation of the transport coefficients of binary mixtures of argon+krypton, krypton+xenon, and argon+xenon by molecular dynamics, Mol. Phys. **73** (1991) 483-494.

[208] Peereboom P.W.E., Luigjes H., and Prins K.O., An NMR spin-echo study of self-diffusion in xenon, Physica A **156** (1989) 260-276.

[209] Perronace A., Ciccotti G., Leroy F., Fuchs A.H., and Rousseau B., Soret coefficient for liquid argon krypton mixtures via equilibrium and nonequilibrium molecular dynamics: A comparison with experiments, Phys. Rev. E **66** (2002) 031201.

[210] Perronace A., Leppla C., Leroy F., Rousseau B., and Wiegand S., Soret and mass diffusion measurements and molecular dynamics simulations of n-pentane+n-decane mixtures, J. Chem. Phys. **116** (2002) 3718-3729.

[211] Petravic J., Evans D.J., Approach to the nonequilibrium timeperiodic state in a steady shear flow model, Mol. Phys. **95** (1998) 219-231.

[212] Petravic J., Time dependence of phase variables in a steady shear flow algorithm, Phys. Rev. E **71** (2005) 011202.

[213] Poling B.E., Prausnitz J.M., and O'connell J.P., The properties of gases and liquids, McGaw-Hill, New York, 2000.

[214] Pohl P.I., Heffelfinger G.S., Massively parallel molecular dynamics simulation of gas permeation across porous silica membranes, J. Membr. Sci. **155** (1999) 1-7.

[215] Puibasset J., Phase coexistence in heteregeneous porous media: A new extension to Gibbs ensemble Monte Carlo simulation methods, J. Chem. Phys. **122** (2005) 134710.

[216] Raabe G., Todd B.D., and Sadus R.J., Molecular simulation of the shear viscosity and the self-diffusion coefficient of mercury along vapor-liquid coexistence curve, J. Chem. Phys. **123** (2005) 034511.

[217] Rah K., Eu B.C., Generic van der Waals equation of state and theory of diffusion coefficients: Binary mixtures of simple liquids, J. Chem. Phys. **116** (2002) 7967-7976.

[218] Reed T.M., Gubbins K.E., Applied statistical mechanics; Thermodynamic and transport properties of fluids, McGraw-Hill, New York, 1973.

[219] Rowley R.L., Stoker J.M., Molecular dynamics simulation of mutual diffusion in nonideal liquid mixtures, Int. J. Thermopys. **12** (1991) 501-513.

[220] Rowley R.L., Paiter M.M., Diffusion and viscosity equations of state for a Lennard-Jones fluid obtained from molecular dynamics simulations, Int. J. Thermophys. **18** (1997) 1109-1121.

[221] Rowley R.L., personal comunication. There exist two erros in the cited reference of Rowley et al., it should read: b_{32}=1067.97, w_2=-2.2065, also the subscript in equation (10) should read j instead i.

[222] Ryckaert J.P., Bellemans A., Ciccotti G., and Paolini G.V., Evaluation of transport coefficients of simple fluids by molecular dynamics comparison of *Green-Kubo and nonequilibrium approaches for shear viscosity*, Phys. Rev. A **39** (1989) 259-267.

[223] Saager B., Hennenberg R., and Fischer J., Construction and application of physically based equations of state 1. Modification of the back equation, Fluid Phase Equilib. **72** (1992) 41-66.

[224] Saager B., Fischer J., Construction and application af physically based equations of state 2. The dipolar and quadrupolar contributions to the Helmholtz energy, Fluid Phase Equilib. **72** (1992) 67-88.

[225] Sarman S.S, Evans D.J., and Cummings P.T., Recent developments in non-Newtonian molecular dynamics, Phys. Rep. **305** (1998) 1-92.

[226] Scheie C.E., Peterson E.M., and O'Reilly D.E., Self-diffusion and rotational correlation times in liquid acetylene, J. Chem. Phys. **59** (1973) 2303-2304.

[227] Schelling P.K., Phillpot S.R., and Keblinski P., Comparison of atomic-level simulation methods for computing thermal conductivity, Phys. Rev. B **65** (2002) 144306.

[228] Schoen M., Hoheisel C., The mutual diffusion coefficient-D_{12} in binary-liquid model mixtures. Molecular dynamics calculations based on Lennard-Jones (12-6) potentials 1. The method of determination, Mol. Phys. **52** (1984) 33-56.

[229] Schoen M., Hoheisel C., The shear viscosity of a Lennard-Jones fluid calculated by equilibrium molecular dynamics, Mol. Phys. **56** (1985) 653-672.

[230] Schoen M., Hoheisel C., Liquid CH_4, liquid CF_4 and the partially miscible liquid mixture CH_4/CF_4. A molecular dynamics study based on both a spherically symmetrical and a 4-Center Lennard-Jones potential model, J. Chem. Phys. **58** (1986) 699-709.

[231] Schofiel P., Computer simulation studies of liquid state, Comput. Phys. Commun. **5** (1973) 17-23.

[232] Shankland I.R., Dunlop P.J., Pressure dependence of the mutual diffusion coefficients of the binary systems N_2+Ar, N_2+O_2, O_2+Ar and Ar+Kr at 300 K and 323 K, Physica A **100** (1980) 64-84.

[233] Sharma S., Woodcock L.V., Interfacial viscosities via stress autocorrelation functions, J. Chem. Soc. Faraday Trans. **87** (1991) 2023-2030.

[234] Shing K.S., Gubbins K.E., Free energy and vapor liquid equilibria for a quadrupolar Lennard-Jones fluid, Mol. Phys. **45** (1982) 129-139.

[235] Shukla K., Thermodynamic properties of binary mixtures of atoms and quadrupolar diatomic molecules from computer simulation, Fluid Phase Equilib. **128** (1997) 29-46.

[236] Simon J.M., Dysthe D.K., Fuchs A.H., and Rousseau B., Thermal diffusion in alkane binary mixtures. A molecular dynamics approach, Fluid Phase Equilib. **151** (1998) 151-159.

[237] Simon J.M., Rousseau B., Dysthe D.K., and Hasfkjold B., Thermal diffusion in methane+n-decane mixtures by molecular dynamics using spherical and flexible multicenter models, Entropy **217** (1999) 29-32.

[238] Sindzingre P., Ciccotti G., Massobrio C., and Frenkel D., Partial enthalpies and related quantities in mixtures from computer simulation, Chem. Phys. Lett. **136** (1987) 35-41.

[239] Singer J.R., Excess ultrasonic attenuation and volume viscosity in liquid methane, J. Chem. Phys. **51** (1969) 4729-4733.

[240] Singer K., Singer J.V.L., and Taylor A.J., Molecular dynamics of liquids modeled by 2-Lennard-Jones centers pair potentials 2. Translational and rotational autocorrelation functions, Mol. Phys. **37** (1979) 1239-1262.

[241] Singer K., Singer J.V.L., and Fincham D., Deterination of the shear viscosity of atomics liquids by non equilibrium molecular dynamics, Mol. Phys. **40** (1980) 515-519.

[242] Slyusar V.P., Tretyakov V.M., and Rudenko N.S., The constant volume thermal conductivity of liquid and gaseous nitrogen over the 64.2-300 K temperature range. Thermal conductivity of nitrogen in the critical region, Sov. J. Low. Tem. Phys. **1** (1975) 556-561.

[243] Slyusar V.P., Tretyakov V.M., and Rudenko N.S., Thermal conductivity of krypton and xenon at constant density and pressures up to 2700 atm. Law of corresponding states, Sov. J. Low. Tem. Phys. **4** (1978) 363-368.

[244] Stassen H., Steele W.A., Simulation studies of shear viscosity time correlation functions, J. Chem. Phys. **102** (1995) 932-938.

[245] Steele W.A., in Hanley H.J.M. (Ed.), Transport phenomena in fluids, Marcel Dekker, New York and London, 1969.

[246] Stockmayer W.H., Second virial coefficients of polar gases, J. Chem. Phys. **9** (1941) 398-402.

[247] Stoker J.M., Rowley R.L., Molecular dynamics simulation of real fluid mutual diffusion coefficients with the Lennard-Jones potential model, J. Chem. Phys. **91** (1989) 3670-3676.

[248] Stoll J., Vrabec J., Hasse H., and Fischer J., Comprehensive study of the vapour-liquid equilibria of the pure two-centre Lennard-Jones plus point quadrupole fluid, Fluid Phase Equilib. **179** (2001) 339-362.

[249] Stoll J., Vrabec J., and Hasse H., Vapor-liquid equilibria of mixtures containing nitrogen, oxygen, carbon dioxide, and ethane, AIChE J. **49** (2003) 2187-2198.

[250] Stoll J., Vrabec J., and Hasse H., A set of molecular models for carbon monoxide and halogenated hydrocarbons, J. Chem. Phys. **119** (2003) 11396.

[251] Stoll J., Vrabec J., and Hasse H., Comprehensive study of the vapour-liquid equilibria of the pure two-centre Lennard-Jones plus pointdipole fluid, Fluid Phase Equilib. **209** (2003) 29-53.

[252] Stoll J., PhD. Thesis, Molecular models for the prediction of thermophysical properties of pure fluid and mixtures, Reihe 3, Band 836, VDI, Düsseldorf, 2005.

[253] Straub J.E., Analysis of the role of attractive forces in self-diffusion of a simple fluid, Mol. Phys. **76** (1992) 373-385.

[254] Streett W.B., Tildesley D.J., Computer simulations of polyatomic molecules 2. Molecular dynamics studies of diatomic liquids with atom-atom and quadrupole-quadrupole potentials, Proc. R. Soc. A **355** (1977) 239-266.

[255] Tham M.J., Gubbins K.E., Correspondence principle for transport properties of dense fluids, Ing. Eng. Chem. Fundam. **8** (1969) 791-795.

[256] Tham M.J., Gubbins K.E., Correspondence principle for transport properties of dense fluids. Nonpolar polyatomic fluids, Ing. Eng. Chem. Fundam. **9** (1970) 63-70.

[257] Thompson A.P., Ford D.M., and Heffelfinger G.S., Direct molecular simulation of gradient-driven diffusion, J. Chem. Phys. **109** (1998) 6406-6414.

[258] Thompson A.P., Heffelfinger G.S., Direct molecular simulation of gradient-driven diffusion of large molecules using constant pressure, J. Chem. Phys. **110** (1999) 10693-10705.

[259] Tison J.K., Hunt E.R., Self-diffusion, spin lattice relaxation, and density of SF_6 near critical point, J. Chem. Phys. **54** (1971) 1526-1531.

[260] Todd B.D., Computer simulation of simple and complex atomistic fluids by nonequilibrium molecular dynamics techniques, Comput. Phys. Commun. **142** (2001) 14-21.

[261] Todd B.D., Power law exponents for the shear viscosity of non-Newtonian simple fluids, Phys. Rev. E **72** (2005) 041204.

[262] Todd B.D., Cats, maps and nanoflows: Some recent developments in nonequilibrium nanofluidics, Mol. Simul. **31** (2005) 411-428.

[263] Tokumasu T., Ohara T., and Kamijo K., Effect of molecular elongation on the thermal conductivity of diatomic liquids, J. Chem. Phys. **118** (2003) 3677-3685.

[264] Travis K.P., Searles D.J., and Evans D.J., Strain rate dependent properties of a simple fluid, Mol. Phys. **95** (1998) 195-202.

[265] Trozzi C., Ciccotti G., Stationary nonequilibrium states by molecular dynamics 2. Newtons law, Phys. Rev. A **29** (1984) 916-925.

[266] Van de Ven-Lucassen I.M.J.J., Vlugt T.J.H., van der Zenden A.J.J., and Kerkhof P.J.A.M., Using molecular dynamics to obtain Maxwell-Stefan diffusion coefficients in liquid systems, Mol. Phys. **94** (1998) 495-503.

[267] Van de Ven-Lucassen I.M.J.J., Otten A.M.V.J., Vlugt T.J.H., and Kerkhof P.J.A.M., Molecular dynamics simulation of the Maxwell-Stefan diffusion coefficients in Lennard-Jones liquid mixtures, Mol. Simul. **23** (1999) 43-54.

[268] Van de Ven-Lucassen I.M.J.J., Vlugt T.J.H., van der Zanden A.J.J., and Kerkhof P.J.A.M., Molecular dynamics simulation of self-diffusion and Maxwell-Stefan diffusion coefficients in liquid mixtures of methanol and water, Mol. Simul. **23** (1999) 79-94.

[269] Van Heijningen R.J.J., Harpe J.P., and Beenakker J.J.M., Determination of diffusion coefficients of binary mixtures of noble gases as a function of temperature and concentration, Physica A **38** (1968) 1-34.

[270] Vargaftik N.B., Vinogradov Y.K., and Yargin V.S., Handbook of physical properties of liquids and gases, Begell house, New York, 1996.

[271] Vega C., Lago S., de Miguel E., and Rull L.F., Liquid vapor equilibria of linear Kihara molecules, J. Phys. Chem. **96** (1992) 7431-7437.

[272] Vega C., McBride C., and Menduina C., The second virial coefficient of the dipolar two center Lennard-Jones model, Phys. Chem. Chem. Phys. **4** (2002) 3000-3007.

[273] Vignes A., Diffusion in binary solutions variation of diffusion coefficient with composition, Ind. Eng. Chem. Fundam. **5** (1966) 189-199.

[274] Vogelsang R., Hoheisel C., and Ciccotti G., Thermal conductivity of the Lennard-Jones liquid by molecular dynamics calculations, J. Chem. Phys. **86** (1987) 6371-6375.

[275] Vogelsang R., Hoheisel C., Thermal conductivity of a binary liquid mixture studied by molecular dynamics with use of Lennard-Jones potentials, Phys. Rev. A **35** (1987) 3487-3491.

[276] Vogelsang R., Hoheisel C., Comparison of various potential models for the simulation of the pressure of liquid and fluid N_2, Phys. Chem. Liq. **16** (1987) 189-203.

[277] Vrabec J., Fischer J., Vapor-liquid equilibria of the ternary mixture CH_4+C_2H_6+CO_2 from molecular simulation, AIChE J. **43** (1997) 212-217.

[278] Vrabec J., Stoll J., and Hasse H., A set of molecular models for symmetric quadrupolar fluids, J. Phys. Chem. B. **105** (2001) 12126-12133.

[279] Vrabec J., Stoll J., and Hasse H., Molecular models of unlike interactions in fluid mixtures, Mol. Simul. **31** (2005) 215-221.

[280] Vrabec J., Kedia G.K., and Hasse H., Prediction of Joule-Thomson inversion curves for pure fluids and one mixture by molecular simulation", Cryogenics **45** (2005) 253-258.

[281] Wang B.Y., Cummings P.T, and Evans D.J., Nonequilibrium molecular dynamics study of molecular contributions to the thermal conductivity of carbon dioxide, Mol. Phys. **75** (1992) 1345-1356.

[282] Weingerl U., Fischer J., Consideration of dipole-quadrupole interactions in molecular based equations of state, Fluid Phase Equilib. **202** (2002) 49-66.

[283] Winkelmann J., Application of perturbation theory to vapor-liquid equilibri Calculation for dipolar quadrupolar fluids, Fluid Phase Equilib. **48** (1989) 67-81.

[284] Woolf L.A., Self-diffusion in carbon disulfide under pressure, J. Chem. Soc. Faraday. Trans. 1 **78** (1982) 583-590.

[285] Yeh I., Hummer G., System-size dependence of diffusion coefficients and viscosities from molecular dynamics simulations with periodic boundary conditions, J. Phys. Chem. B **108** (2004) 15873-15879.

[286] Zhang L.Z., Balasundaram R., Gehrke S.H., and Jiang S.Y., Nonequilibrium molecular dynamics simulations of confined fluids in contact with the bulk, J. Chem. Phys. **114** (2001) 6869-6877.

[287] Zhang L.Z., Jiang S.Y., Molecular simulation study of nanoscale friction for alkyl monolayers on Si(111), J. Chem. Phys. **117** (2002) 1804-1811.

[288] Zhang L.Z., Jiang S.Y., Molecular simulation study of nanoscale friction between alkyl monolayers on Si(111) immersed in solvents, J. Chem. Phys. **119** (2003) 765-770.

[289] Zhang M.M., Lussetti E., de Souza L.E.S., and Müller-Plathe F., Thermal conductivities of molecular liquids by reverse nonequilibrium molecular dynamics, J. Phys. Chem. B **109** (2005) 15060-15067.

[290] Zheng J., Lennon E.M., Tsao H.K., Sheng Y.J., and Jiang S.Y., Transport of a liquid water and methanol mixture through carbon nanotubes under a chemical potential gradient, J. Chem. Phys. **122** (2005) 214702.

[291] Zhou Y., Miller G.H., Mutual diffusion in binary Ar+Kr mixtures and empirical diffusion models, Phys. Rev. E. **53** (1996) 1587-1601.

[292] Zwanzig R., Time correlation functions and transport coefficients in statistical mechanics, Ann. Rev. Phys. Chem. **16** (1965) 67-102.

ISBN 978-3-8322-6462-8